INFORMATION TO USERS

This manuscript has been reproduced from the microfilm master. UMI films the text directly from the original or copy submitted. Thus, some thesis and dissertation copies are in typewriter face, while others may be from any type of computer printer.

The quality of this reproduction is dependent upon the quality of the copy submitted. Broken or indistinct print, colored or poor quality illustrations and photographs, print bleedthrough, substandard margins, and improper alignment can adversely affect reproduction.

In the unlikely event that the author did not send UMI a complete manuscript and there are missing pages, these will be noted. Also, if unauthorized copyright material had to be removed, a note will indicate the deletion.

Oversize materials (e.g., maps, drawings, charts) are reproduced by sectioning the original, beginning at the upper left-hand corner and continuing from left to right in equal sections with small overlaps.

Photographs included in the original manuscript have been reproduced xerographically in this copy. Higher quality 6" x 9" black and white photographic prints are available for any photographs or illustrations appearing in this copy for an additional charge. Contact UMI directly to order.

Bell & Howell Information and Learning
300 North Zeeb Road, Ann Arbor, MI 48106-1346 USA
800-521-0600

UMI®

VORTEX DISTRIBUTIONS AND DYNAMICS IN SUPERCONDUCTORS NEAR SURFACE STEPS AND SAMPLE EDGES STUDIED BY SCANNING SQUID MICROSCOPY AND CRITICAL CURRENT MEASUREMENTS

BY

BRITTON LOUIS PLOURDE

B.S., University of Michigan, 1993
B.Mus., University of Michigan, 1993
M.S., University of Illinois, 1995
M.Mus., University of Illinois, 1999

THESIS

Submitted in partial fulfillment of the requirements
for the degree of Doctor of Philosophy in Physics
in the Graduate College of the
University of Illinois at Urbana-Champaign, 2000

Urbana, Illinois

UNIVERSITY OF ILLINOIS AT URBANA-CHAMPAIGN

THE GRADUATE COLLEGE

JULY 2000
(date)

WE HEREBY RECOMMEND THAT THE THESIS BY

BRITTON LOUIS PLOURDE

ENTITLED VORTEX DISTRIBUTIONS AND DYNAMICS IN SUPERCONDUCTORS
NEAR SURFACE STEPS AND SAMPLE EDGES STUDIED BY
SCANNING SQUID MICROSCOPY AND CRITICAL CURRENT MEASUREMENTS

BE ACCEPTED IN PARTIAL FULFILLMENT OF THE REQUIREMENTS FOR

THE DEGREE OF DOCTOR OF PHILOSOPHY

Dale J Van Harlingen
Director of Thesis Research

Head of Department

Committee on Final Examination†

M. B. Weissman
Chairperson

Dale J Van Harlingen

Tony Leggett

† Required for doctor's degree but not for master's.

O-517

VORTEX DISTRIBUTIONS AND DYNAMICS IN SUPERCONDUCTORS NEAR SURFACE STEPS AND SAMPLE EDGES STUDIED BY SCANNING SQUID MICROSCOPY AND CRITICAL CURRENT MEASUREMENTS

Britton Louis Plourde. Ph.D.
Department of Physics
University of Illinois at Urbana-Champaign. 2000
Dale J. Van Harlingen. Advisor

We have studied the interactions of vortices in superconductors with surface features and sample edges. Surface steps can generate an asymmetric vortex pinning potential and can influence the distribution of vortices upon cooling into the superconducting state in an applied magnetic field. The edge of a sample acts as a barrier to vortex entry into the superconductor and can have a substantial effect on the transport properties of vortices. We have used a Scanning SQUID Microscope (SSM) to directly image the vortex distributions in various superconducting systems, including crystals with naturally cleaved surface steps as well as patterned superconducting thin films with etched surface trenches. The vortex distributions are significantly altered in the vicinity of the surface steps, and we have found evidence for a possibly paramagnetic compression of flux into surface trenches on thin film samples. We have studied vortex interactions with edge barriers primarily through transport measurements. By measuring the critical current at which the superconductor first develops a finite voltage, we are able to probe the entry of vortices at the edge of a superconducting strip in a perpendicular magnetic field. Our results display many of the characteristics expected for a thin superconducting strip with only weak bulk pinning based on recent theoretical treatments. We propose new experiments to investigate the possible paramagnetism around surface trenches and we discuss future work to study the edge barrier mechanism further.

ACKNOWLEDGMENTS

My completion of the research presented in this thesis was made possible by the assistance of many people. I would like to thank my thesis advisor. Dale Van Harlingen. for his guidance and patience as I explored several different experiments. I am grateful to the work of Mark Wistrom in building the Scanning SQUID Microscope and developing the software which I used for the vortex imaging measurements. The excellent data acquisition routines written by my fellow group member. Brian Yanoff. were invaluable for the transport experiments on superconducting strips. I also thank Kevin Osborn for performing measurements of the penetration depth in some of the superconducting thin films used in this thesis research. My other research group members over the years. Bill Neils. Joe Hilliard. Tony Bonetti. Trevis Crane. Jack Sadleir. Stuart Tessmer. and Dave Wollman have been helpful in ways too numerous to list.

Much of my research has relied on the resources of the Microfabrication Facility in the Materials Research Laboratory. I thank Tony Banks for his tireless efforts to maintain and improve this center over the past several years. I am also grateful to our collaborators on the experiments presented in this thesis. Rut Besseling. Marcel Hesselberth. and Peter Kes at Leiden University in the Netherlands have generously provided many of the superconducting films used in these measurements and have been excellent sources of information on vortex dynamics. I acknowledge many stimulating conversations (through email) on vortex entry barriers with Denis Vodolazov of Nizhny Novgorod University in Russia. I have also benefited from discussions with other scientists. including John Clem. Franco Nori. and Alexei Bezryadin.

This research has been supported by National Science Foundation Research Grants No. NSF-DMR91-20000 and No. NSF-DMR97-05695.

TABLE OF CONTENTS

CHAPTER

CHAPTER 1

INTRODUCTION

Over a large range of magnetic field and temperature, many superconductors contain regions which are threaded by localized magnetic flux lines. The quantum-mechanical wavefunction which characterizes the superconductivity winds its phase by 2π around one of these flux lines and vanishes at the center. These singularity points are appropriately called vortices, and the amount of flux carried by a vortex is quantized to be $hc/2e$. Vortices in superconductors exhibit a rich variety of phenomena, as the vortices can interact with transport currents, temperature gradients, sample surfaces and defects, and other vortices [1-3].

From a practical standpoint, the dynamics of vortices in superconductors is an important problem, as many applications of superconductors involve the transport of large currents through the material in the presence of substantial magnetic fields. A transport current exerts a tangential force on a vortex, and the motion of vortices generates a voltage which is transverse to the vortex flow direction. Thus in order to avoid dissipation as currents are passed through a superconductor containing vortices, one must be able to pin the vortex distribution in place and prevent the dissipative motion caused by the force from the transport current. The operation of many thin-film superconducting devices also relies on the prevention of vortex motion in the device electrodes. Such motion can result in excessive noise in Superconducting Quantum Interference Devices (SQUIDs). When vortex motion and other noise sources are minimized. SQUIDs can be used to measure extremely small quantities of magnetic flux and small voltages.

In addition to the practical aspects of vortex motion, there exist many fundamental issues in the complex behavior of vortices in superconductors. Vortices in defect-free superconductors will form a lattice due to the repulsive interaction between vortices. However, in certain situations, the vortex lattice can melt from a solid into a liquid, while the presence of disorder can produce a transition to a glassy state. These transitions have been studied in recent measurements of vortex dynamics [4]. Also, vortices in thin superconducting films provide excellent model two-dimensional systems for exploring the nature of the Kosterlitz-Thouless transition [1].

In order to address the above issues, one must have a model for the potential landscape experienced by a vortex in a superconductor. Four important terms comprising this landscape include bulk pinning on sample defects, intervortex interactions, pinning of vortices on surface features, and interactions between vortices and sample surfaces and edges. The first two terms have been studied extensively both through theoretical modeling and experimental work. The interactions of vortices with sample defects such as voids, grain boundaries, and inhomogeneities are reasonably well understood [5, 6]. The mutual repulsion between parallel vortices leads to collective effects at moderate to large magnetic fields, when the vortices are spaced by sufficiently small distances. An understanding of these intervortex interactions led to the successful theory of collective pinning, which describes the ability of a vortex lattice to deform elastically in order to accommodate available pinning sites [7].

The pinning of vortices on surface features is caused by the variation in vortex energy with the length of the vortex. Thus a vortex in a thinner region of a superconductor has a lower energy than a vortex in a thicker area. Surface steps corresponding to such a change in thickness are common in superconductor crystals and can be controllably fabricated in thin-film samples. Early experiments probed the vortex dynamics in the vicinity of surface steps through transport measurements [8, 9]. More recent imaging experiments have studied both static and dynamic vortex states near surface steps in superconductor crystals [10, 11]. However, several of these experiments were contradictory. Also, the possibility of controlling vortex distributions with patterned surface step structures has not yet been explored.

The interactions between vortices and screening currents flowing along sample surfaces and edges can strongly affect the entry and exit of vortices in superconductors as well as the vortex distribution inside the superconductor. This problem has been studied recently in the context of vortex entry into thin platelet crystals of the high-temperature cuprate superconductors, where vortices can tilt and cut across the sample corners before completely entering into the crystal [12]. The entry of vortices into a thin, effectively two-dimensional superconductor has been studied in several theoretical works and is an important fundamental problem in vortex physics and in the design of thin-film superconducting devices [13-15]. However, many of the theoretical predictions for this situation have not yet been tested experimentally.

An understanding of the vortex potential landscape may allow for the control of vortex dynamics at the mesoscopic scale. Thus by fabricating various sample edge shapes, surface step patterns, and bulk defects, it may be possible to influence the distribution and dynamics of vortices in superconductors. Microfabricated structures which only allow vortex motion in certain weak-pinning channels can be used to probe phase transitions in vortex matter in confined geometries [16-18]. The development of asymmetric pinning potentials may allow for the observation of ratchet effects and the rectification of vortex transport [19]. Also, the tailoring of this potential landscape may make possible electronic devices based on the control of vortex dynamics through fabricated pinning structures.

Our approach for investigating this potential landscape has been to study the nature of the vortex interactions with surface steps and sample edges while minimizing the effects of bulk pinning and collective vortex interactions. The interactions between vortices and surface features are best studied by directly imaging the vortex distributions. We have used a Scanning SQUID Microscope (SSM) to obtain magnetic flux images of vortices around steps and to measure dynamical changes in the local vortex density near surface features. Our SSM was first developed by previous UIUC graduate students, Mark Wistrom and Lan Vu for the study of Josephson junction arrays and superconducting wire networks [20-22]. In order to carry out the experiments presented in this thesis, I have fabricated new SQUIDs and pickup loops for the SSM and I have improved the system for the imaging of thin-film superconducting samples with surface steps.

We have studied the vortex interactions with edge barriers through transport measurements of the critical current in thin superconducting strips. The critical current, which corresponds to the first appearance of a finite voltage in the strip, is directly related to the dynamics of vortices in the strip and the entry of vortices at the strip edges. Measurements of the critical currents and current-voltage characteristics in these strips as well as their variation with magnetic field strength provide a direct probe of the edge barrier effects. By varying the strip geometry, we are able to compare our results with the various theoretical predictions.

This thesis describes our investigations of the vortex interactions with surface features and sample edges. Chapter 2 introduces the basic response of a superconductor to a magnetic field, including the Meissner effect and the generation of vortices. In Chapter 3 I discuss the relevant concepts which are necessary for describing vortex behavior in superconductors, such as the vortex response to a transport current, the pinning of vortices on defects, and the barriers to vortex entry at surfaces and edges.

Chapter 4 contains a review of the experimental techniques which are available for studying vortices including the transport measurements and SSM imaging used in this work. I compare the SSM with other magnetic imaging techniques and I explain why the SSM is most appropriate for studying vortex distributions around surface features. Chapter 5 is a detailed description of the SSM system used in these imaging experiments. I discuss the basic imaging principles and the SQUID operation, as well as the insert design and the pickup loop fabrication.

I present the results of our SSM imaging experiments in Chapters 6 and 7. Chapter 6 begins with a review of the previous experimental work on vortex behavior near surface features. I then discuss our SSM imaging of vortex dynamics around surface steps in superconducting $NbSe_2$ crystals. We have imaged field-cooled vortex distributions near steps, dynamical rearrangements of vortices around steps as the magnetic field is varied, and changes in the local flux density during vortex motion. These $NbSe_2$ crystals provide a rich system to study vortex behavior, but the complex surface structure makes it difficult to quantify the dynamics at the various surface features. Subsequently, we have studied vortex distributions in microfabricated thin-film structures with controlled arrangements of surface steps. In Chapter 7, I discuss our investigations of the dependence of the vortex behavior on the surface step height and magnetic field strength. I propose possible mechanisms to explain the observed behavior and I present future experiments which could confirm these scenarios.

Finally, in Chapter 8, I discuss our experiments on edge barrier effects in thin superconducting strips. I summarize the theoretical work on this system and highlight the various predictions for measurable quantities. In addition, I discuss previous transport measurements, some of which have demonstrated some of the expected edge barrier characteristics. I present our measurements of the critical current and current-voltage characteristics of thin weak-pinning superconducting strips. We have measured several of the predicted edge barrier phenomena for the first time, including the entry of vortices for current densities at the strip edge which approach the upper limit of the Ginzburg-Landau depairing current. We have also observed some unexpected features in the critical current and current-voltage dependence which are probably related to the presence of defects along the edges of the strip. I propose several new experiments to further probe the vortex dynamics near these edge defects.

Throughout this thesis, I have generally used Gaussian units. However, for comparison with experimentally measurable quantities, I have switched to SI units in certain places. Expressions in SI units are clearly indicated.

1.1 References

[1] M. Tinkham, *Introduction to Superconductivity* (McGraw-Hill, Inc., New York, 1996).

[2] V. V. Schmidt, *The Physics of Superconductors* (Springer-Verlag, Berlin, 1997).

[3] P. G. de Gennes, *Superconductivity of Metals and Alloys* (Addison-Wesley, Reading, 1989).

[4] G. W. Crabtree, W. K. Kwok, U. Welp, *et al.*, in *Physics and Materials Science of Vortex States, Flux Pinning and Dynamics*, edited by R. Kossowsky, S. Bose, V. Pan and Z. Durusoy (Kluwer Academic, Kusadasi, Turkey, 1998), Vol. 356, p. 357.

[5] R. P. Huebener, *Magnetic Flux Structures in Superconductors* (Springer-Verlag, Berlin, 1979).

[6] A. M. Campbell and J. E. Evetts, *Critical Currents in Superconductors* (Taylor and Francis Ltd., London, 1972).

[7] A. I. Larkin and Y. N. Ovchinnikov, *Pinning in Type II Superconductors*, J. Low Temp. Phys. **34**, 409 (1979).

[8] O. Daldini, P. Martinoli, J. L. Olsen, *et al.*, *Vortex-line Pinning by Thickness Modulation of Superconducting Films*, Phys. Rev. Lett. **32**, 218 (1974).

[9] D. D. Morrison and R. M. Rose, *Controlled Pinning in Superconducting Foils by Surface Microgrooves*, Phys. Rev. Lett. **25**, 356 (1970).

[10] H. Dai, J. Liu, and C. M. Lieber, *Surface Pinning and Grain Boundary Formation in Magnetic Flux-Line Lattices of* $Bi_2Sr_2CaCu_2O_{8+\delta}$ *High-*T_c *Superconductors*, Phys. Rev. Lett. **72**, 748 (1994).

[11] F. Pardo, F. de la Cruz, P. L. Gammel, *et al.*, *Real Space Images of the Vortex Lattice Structure in a Type II Superconductor during Creep over a Barrier*, Phys. Rev. Lett. **79**, 1369 (1997).

[12] E. Zeldov, A. I. Larkin, V. B. Geshkenbein, *et al.*, *Geometrical Barriers in High-Temperature Superconductors*, Phys. Rev. Lett. **73**, 1428 (1994).

[13] M. Y. Kupriyanov and K. K. Likharev, *Effect of an edge barrier on the critical current of superconducting films*, Sov. Phys. Solid State **16**, 1835 (1975).

[14] M. Benkraouda and J. R. Clem, *Critical current from surface barriers in type-II superconducting strips*, Phys. Rev. B **58**, 15103 (1998).

[15] D. Y. Vodolazov and I. L. Maksimov, *Distribution of the magnetic field and current density in superconducting films of finite thickness*, cond-mat/0001035 (2000).

[16] R. Besseling, R. Niggebrugge, and P. H. Kes, *Transport properties of vortices in easy flow channels: a Frenkel-Kontorova study*, Phys. Rev. Lett. **82**, 3144 (1999).

[17] A. Pruymboom, P. H. Kes, E. Van der Drift, *et al.*, *Flux-Line Shear through Narrow Constraints in Superconducting Films*, Phys. Rev. Lett. **60**, 1430 (1988).

[18] M. H. Theunissen, E. Van der Drift, and P. H. Kes, *Size Effects in Flow of Flux-Line Solids and Liquids*, Phys. Rev. Lett. **77**, 159 (1996).

[19] J. F. Wambaugh, C. Reichhardt, C. J. Olson, *et al.*, *Superconducting Fluxon Pumps and Lenses*, Phys. Rev. Lett. **83**, 5106 (1999).

[20] L. N. Vu, M. S. Wistrom, and D. J. Van Harlingen, *Imaging of magnetic vortices in superconducting networks and clusters by scanning SQUID microscopy*, Appl. Phys. Lett. **63**, 1693 (1993).

[21] L. N. Vu and D. J. Van Harlingen, *Design and Implementation of a Scanning SQUID Microscope*, IEEE Trans. Appl. Supercond. **3**, 1918 (1993).

[22] M. S. Wistrom and D. J. Van Harlingen, *To be published*, .

CHAPTER 2

SUPERCONDUCTORS IN MAGNETIC FIELDS

2.1 Basic properties

Superconductors exhibit the striking property of zero electrical resistance, such that currents can flow through the superconductor with no dissipation. This phenomenon was first discovered in 1911 by Kamerlingh Onnes as he investigated the low temperature electrical properties of metals. Kamerlingh Onnes found that as the temperature was lowered, the resistance of the metal decreased until a certain point at which the resistance dropped abruptly to zero, at least within the resolution of his measurement apparatus [1]. This effect was observed in several materials, and could not be explained with the existing theory of metallic conduction.

2.1.3 Perfect conductivity

Electrical conduction in typical metals occurs by the transport of charge through electronic states in the material. This transport process dissipates energy as the conduction electrons scatter off of defects or vibrations of the atomic lattice through which they travel. If one could produce a defect-free metal and cool it down to a low enough temperature such that the phonon vibrational modes were completely frozen out, it is reasonable to expect that the electrical resistance would vanish. Thus conduction electrons could propagate through the material with no dissipation.

If a magnetic field were then applied to this perfect conducting material, the field would be screened out from the interior of the material. A conventional metal with finite resistance will screen out an oscillatory field for length scales longer than the skin depth, which depends on the frequency of the applied field and the conductivity of the metal. Due to the infinite conductivity of this perfect conductor, even a dc magnetic field will be screened out beyond some characteristic penetration length. However, if the sample is cooled in a static magnetic field from some higher temperature, when the sample has some finite resistance, the magnetic field which penetrates the sample at the higher temperature will remain in the interior once the material becomes perfectly conducting [1].

2.1.2 Meissner effect

After the initial discovery of a zero electrical resistance state in certain metals, the response of these materials to an applied magnetic field was investigated. In 1933, Meissner and Ochsenfeld discovered that a superconductor cooled through its transition temperature in an applied magnetic field would actually expel all of the magnetic flux from its interior, in contrast to the expected response of a perfect conductor [2]. This perfect diamagnetic screening was termed the Meissner effect, and persists for applied magnetic fields up to a critical field, H_c. For fields larger than H_c, the superconductivity breaks down and the material has a finite resistance. These superconducting metals appear to enter a new thermodynamic phase, characterized by perfect conductivity, in which the material can lower its free energy by expelling a magnetic field [3].

2.1.3 London equations

The characteristic response of superconductors, perfect conductivity and perfect diamagnetism, can be described by two phenomenological equations in addition to the Maxwell equations. The perfect conductivity is accounted for by the first London equation:

$$\vec{E} = \frac{\partial}{\partial t}(\Lambda \vec{J_s}) \tag{2.1}$$

where $\Lambda = \frac{m}{n_s e^2}$, and n_s is the density of superconducting charge carriers. This equation describes an acceleration of the superelectrons under an applied electric field, in contrast to the response of a resistive metal, $\vec{J} = \sigma \vec{E}$, as described by the Drude model of conductivity [2].

The response of a superconductor to a magnetic field is described by the second London equation:

$$\vec{h} = -c\vec{\nabla} \times (\Lambda \vec{J_s}) \tag{2.2}$$

where $\vec{h}$ is the local magnetic flux density. When combined with the Maxwell equation,

$$\vec{\nabla} \times \vec{h} = \frac{4\pi}{c}\vec{J} \tag{2.3}$$

one obtains:

$$\nabla^2 \vec{h} = \frac{\vec{h}}{\lambda^2} \tag{2.4}$$

where the length scale, λ, is related to Λ by $\Lambda = \frac{m}{n_s e^2} = \frac{4\pi\lambda^2}{c^2}$. If equation (2.4) is applied to a superconducting half plane in a parallel magnetic field, the resulting solutions h(x) is:

$$h(x) = h(0)\exp(-x/\lambda) \tag{2.5}$$

where h(0) is the applied magnetic field at the surface, x = 0. Thus a magnetic field is exponentially screened out of a superconductor, such that B = 0 in the interior of the superconductor, as described by the Meissner effect. The characteristic screening length,

λ is called the penetration depth, and can range from about 40nm up to 1μm for different materials [2, 3].

2.1.4 Demagnetizing effects

When a long thin superconducting sample is placed in a magnetic field parallel to the long axis of the sample, the field is screened out of the interior, and the magnetic field at the surface of the sample is effectively equal to the applied field. However, when the sample has some finite width with respect to its length, the Meissner screening causes the net field to be distorted at the edges of the sample, such that the field at the surface can be larger than the applied magnetic field. In the limit of a semi-infinite thin superconducting slab placed in a perpendicular magnetic field, some of the field must penetrate the superconductor. This process occurs by some fraction of the slab being driven into the normal conducting state, allowing flux to penetrate, while the rest of the sample remains in the superconducting state with $B = 0$. The fraction of normal regions is given by H_a/H_c, where H_a is the applied magnetic field and H_c is the thermodynamic critical field of the superconductor [2, 3]. A description of the physical structure of the superconducting and normal regions in this situation requires a more detailed approach to the magnetic response of the superconductor.

2.2 Descriptions of the superconducting state

2.2.1 BCS pairing

Following the initial discovery of superconductivity in Hg, over forty years passed before a successful theory was developed to explain the occurrence of this state in metals and alloys. In 1957, Bardeen, Cooper, and Schrieffer (BCS) proposed a theory of a phonon-mediated attractive interaction between electrons with opposite momenta. This attraction produces pairs of electrons which condense into a macroscopic quantum state which can be described by a single complex wavefunction. The spatial extent of these Cooper pairs of electrons is characterized by the length scale. ξ_0. the BCS coherence length. The magnitude of ξ_0 can range from a few nm up to several microns for different superconductors. The BCS theory gained wide acceptance after several important predictions of the theory were confirmed experimentally [2].

2.2.2 Ginzburg-Landau phenomenology

In order to describe the magnetic response of superconductors. a detailed description of the mechanism of superconductivity is not necessary. Instead a phenomenological method will suffice. Ginzburg and Landau (GL) developed a theory describing the behavior of a system of superconducting charge carriers with long-range phase coherence. without referring directly to the mechanism which produces the superconductivity. The density and phase of the superelectrons are characterized by a complex order parameter. ψ. Near the critical temperature when superconductivity develops. ψ is small. and the free energy of the system can be expanded in powers of ψ:

$$f = f_n + \alpha|\psi|^2 + \frac{\beta}{2}|\psi|^4 + \frac{1}{2m^*}\left|\left(\frac{\hbar}{i}\vec{\nabla} - \frac{e^*}{c}\vec{A}\right)\psi\right|^2 + \frac{h^2}{8\pi} \tag{2.6}$$

where m^* and e^* are the mass and charge of the superelectrons. respectively. The free energy of the system in the normal state is given by $f_n + \frac{h^2}{8\pi}$. where the last term is the field energy. For certain combinations of the coupling constants, α and β. the system can lower its free energy with respect to the normal state by developing a finite order parameter, ψ, thus becoming superconducting [2, 3]. By minimizing this free energy with respect to ψ, one can generate a pair of differential equations describing the evolution of ψ.

Variations in the magnitude and phase of ψ occur on the scale of the GL coherence length, ξ_{GL}. For temperatures sufficiently below T_c and for clean materials, ξ_{GL} is approximately equal to the BCS coherence length discussed earlier [2]. When an external current is passed through a superconductor, the phase of ψ will wind and the magnitude will decrease according to the GL equations. At some critical value of the applied current, ψ will vanish, and the superconductivity will be destroyed. This current, called the depairing current is given by:

$$J_0 = \left(\frac{c}{4\pi}\right)\frac{\Phi_0}{3\sqrt{3}\pi\lambda^2\xi}. \tag{2.7}$$

J_0 can be quite large in practical superconductors, ranging between 10^6 and 10^8 A/cm^2.

2.2.3 Two types of superconductor

The length scales which characterize a superconductor are the coherence length and the magnetic penetration depth. The ratio of these two lengths, the Ginzburg-Landau parameter, $\kappa=\lambda/\xi$ separates two different types of magnetic response of a superconductor. In order for magnetic flux to penetrate a superconductor, some regions of the material must be driven normal, as discussed earlier for the example of a thin plate in a perpendicular field. Using the GL theory, it is possible to calculate the energy required to form a domain wall between a superconducting region and a normal region [2].

For superconductors with $\kappa < 1/\sqrt{2}$, the energy of forming this domain wall is positive. The magnetic field penetrates the superconductor over the short length scale, λ.

Because the coherence length is longer than the penetration length, the order parameter, ψ does not vary significantly over λ. This results in an energy cost for generating a domain wall [2]. Materials in this category, called *type-I* superconductors, tend to be pure metals, such as Al or Sn. Ideal type-I samples will perfectly screen out an applied magnetic field, maintaining $B = 0$ in the sample bulk until the applied field reaches the thermodynamic critical field, H_c, at which point the superconductivity is destroyed. This can be seen in the schematic magnetization curve shown in Figure 2.1 [3]. Typical values of H_c are in the range of 30 Oe - 800 Oe [3]. Type-I samples with significant demagnetizing factors can allow a certain fraction of magnetic flux to enter the sample interior. These normal regions develop so as to minimize the number of normal - superconductor interfaces which must be formed. Flux patterns in thin type-I superconductor samples in perpendicular magnetic fields have been studied with various magnetic imaging techniques [4, 5].

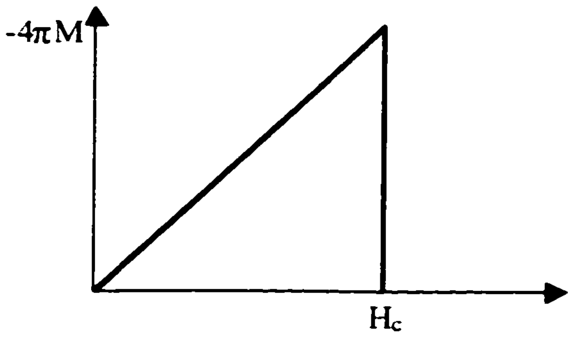

Figure 2.1: Magnetization, M(H) for a bulk type-I superconductor.

If $\kappa > 1/\sqrt{2}$, the shorter coherence length allows the order parameter to be easily reduced to zero within the magnetic penetration length. These materials, *type-II* superconductors, have a negative energy associated with the formation of a normal - superconductor domain wall. Most superconducting alloys as well as the high temperature cuprate superconductors fall in this category. In a certain range of applied magnetic field, when magnetic flux penetrates the interior, the superconductor will attempt to form as many domain walls as possible in order to maximize the energy gain [2, 5]. This results in the magnetic flux in the sample being broken into the smallest possible bundles. Each bundle carries a single quantum of flux:

$$\Phi_0 = \frac{hc}{2e} = 20.7\times10^{-8} G - cm^2 \tag{2.8}$$

and is called a vortex because of the circulation of supercurrent around the point where the order parameter vanishes. Vortices in a bulk sample experience a repulsive force from neighboring parallel vortices due to the interaction of the circulating currents around each vortex [5]. The currents, local magnetic fields, and interactions of vortices will be treated in more detail in subsequent chapters.

2.2.4 Type-II superconductors in a magnetic field

For small applied magnetic fields, an ideal type-II superconductor will perfectly screen out the field, maintaining B = 0 in the interior. However, once the applied field is sufficiently large, the lowest energy state of the system no longer occurs for B = 0 in the interior, and the sample allows vortices of magnetic flux to enter the sample. This crossover point is called the lower critical field, H_{c1}, and is given approximately by the expression [2]:

$$H_{c1} \approx \frac{\Phi_0}{4\pi\lambda^2}\ln\kappa . \tag{2.9}$$

Typical values of H_{c1} range between 50 Oe and several hundred Oe.

For applied fields larger than H_{c1}, vortices enter the superconductor, because the energy cost associated with maintaining perfect diamagnetism is greater than the energy required to nucleate vortices inside the superconductor. This nucleation energy is associated with introducing the circulating current loop of a vortex into the superconductor, and is given by the vortex line tension:

$$\varepsilon_L = \left(\frac{\Phi_0}{4\pi\lambda}\right)^2 \ln\kappa . \tag{2.10}$$

This line tension has units of energy/length, where the length is measured along the magnetic flux threading the vortex [2]. Thus a vortex penetrating a thicker region of a sample will have a larger line energy. Equation 2.10 is approximate because the energetic contribution from the vortex core has been neglected. Treating this term by solving the GL equations numerically, one obtains a correction factor, which is small for large κ materials [6].

Type-II superconductors in magnetic fields larger than H_{c1} are described as being in the mixed state, as the superconductivity coexists with the normal regions in the vortex cores. As the applied magnetic field is increased, more vortices enter the sample. Due to the repulsive interaction between vortices, a lattice of vortices forms which minimizes this interaction energy. For larger fields, the intervortex separation decreases until the normal vortex cores begin to overlap, thus leaving no superconducting regions in the sample. At this value of the applied field called the upper critical field, H_{c2},

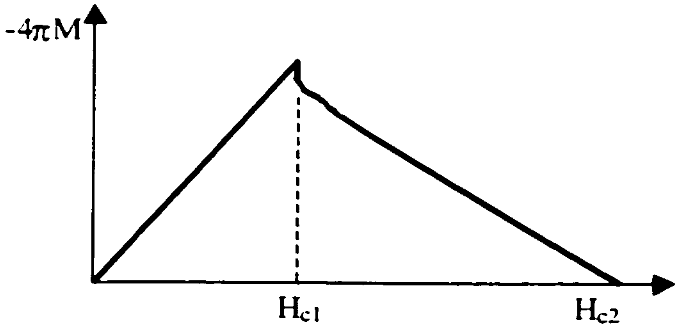

Figure 2.2: Magnetization, M(H) for a bulk type-II superconductor.

superconductivity in the bulk is destroyed [2]. Strongly type-II superconductors can have upper critical fields which are considerably larger than the thermodynamic critical fields of type-I materials. For some of the cuprate superconductors, $\mu_0 H_{c2}$ can be on the order of 100 T. The magnetization behavior of a type-II superconductor is shown schematically in Figure 2.2. For applied fields below H_{c1}, the sample remains perfectly diamagnetic, with the maximum magnetization when $H = H_{c1}$. As the field is increased further, the entry of vortices parallel to the applied field reduces the diamagnetic moment until superconductivity vanishes at H_{c2} [5]. The various states of a type-II superconductor are shown in the field-temperature diagram, shown in Figure 2.3. The magnetic response described to this point has referred to superconductors which were cooled through T_c in zero-field with a magnetic field applied after the development of superconductivity. Vortices can also be introduced into a type-II superconductor by cooling the sample from the normal state through T_c in an applied field.

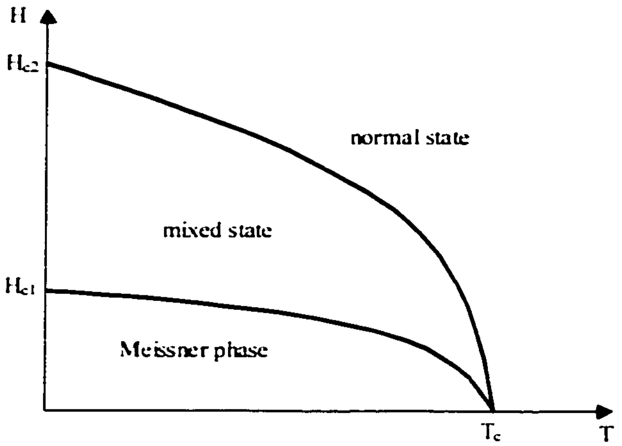

Figure 2.3: H-T phase diagram for a type-II superconductor. B=0 in the bulk for the Meissner phase, while vortices are present in the mixed state.

For a type-II superconductor, the thermodynamic critical field, H_c still relates to the condensation energy of the superconducting state. However, no bulk transition occurs at H_c. The lower critical field, H_{c1} is related to H_c through the expression [2]:

$$H_c \approx \frac{\sqrt{2}\kappa}{\ln \kappa} H_{c1} \tag{2.11}$$

2.2.5 Superconducting parameters for dirty metals

In order to determine the superconducting parameters, such as λ, ξ, and κ, for most materials, sophisticated experimental techniques are required. However, if the material is a particularly dirty metal, with an electronic mean free path shorter than the coherence length, then certain expressions can be used to relate these parameters to more experimentally accessible quantities. By measuring T_c, the zero-temperature normal state resistance, ρ_0, and the slope of the upper-critical field near T_c, $S \equiv -\mu_0 \left.\frac{dH_{c2}}{dT}\right|_{T_c}$, it is possible to obtain the effective zero-temperature penetration depth, λ(0) and coherence length, ξ(0) as well as the Ginzburg-Landau parameter, κ using the following expressions [2, 7]:

$$\lambda(0) = 1.05x10^{-3}(\rho_0/T_c)^{1/2} \tag{2.12}$$

$$\xi(0) = 1.81x10^{-8}(T_c S)^{-1/2} \tag{2.13}$$

$$\kappa = 3.54x10^{4}(\rho S)^{1/2}. \tag{2.14}$$

These dirty-limit equations are all given in practical SI units. Thus using T_c in Kelvin, ρ_0 in Ohm-meters, and S in Tesla/Kelvin, equations 2.12 and 2.13 will give lengths in meters.

2.2.6 Surface superconductivity

While superconductivity is destroyed in the bulk at H_{c2}, it is possible for superconductivity to exist up to substantially larger fields in a surface sheath for surfaces parallel to the applied field. By solving the Ginzburg-Landau equation for the nucleation of the superconducting order parameter, the presence of a surface boundary parallel to the magnetic field allows for a solution in a sheath within ξ of the surface for fields up to

$$H_{c3} = 1.7H_{c2}. \tag{2.15}$$

The existence of H_{c3} modifies the phase diagram for certain surfaces as shown in Figure 2.4 [2, 3].

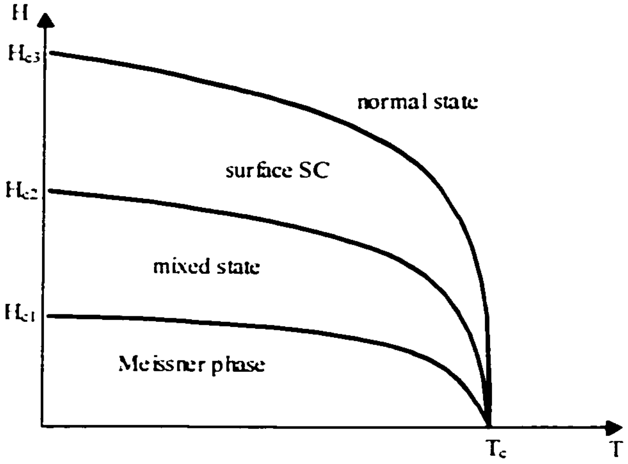

Figure 2.4: H-T phase diagram for a surface parallel to the applied magnetic field, showing the regime of surface superconductivity.

2.3 References

[1] T. P. Orlando and K. A. Delin, *Foundations of Applied Superconductivity* (Addison-Wesley, Reading, 1991).

[2] M. Tinkham, *Introduction to Superconductivity* (McGraw-Hill, Inc., New York, 1996).

[3] P. G. de Gennes. *Superconductivity of Metals and Alloys* (Addison-Wesley. Reading. 1989).

[4] R. P. Huebener. *Magnetic Flux Structures in Superconductors* (Springer-Verlag. Berlin. 1979).

[5] A. C. Rose-Innes and E. H. Rhoderick. *Introduction to Superconductivity* (Pergamon Press. Oxford. 1978).

[6] V. V. Schmidt. *The Physics of Superconductors* (Springer-Verlag. Berlin. 1997).

[7] P. H. Kes and C. C. Tsuei. *Two-dimensional collective flux pinning. defects. and structural relaxation in amorphous superconducting films*. Phys. Rev. B **28**. 5126 (1983).

CHAPTER 3

PHYSICS OF VORTICES IN TYPE-II SUPERCONDUCTORS

A complete discussion of vortex dynamics in superconductors requires a description of the characteristics of a vortex as well as a summary of the various interactions which make up the potential landscape experienced by a vortex. This chapter begins with a description of vortex profiles and the response of vortices to currents. We then discuss the influence of bulk pinning as well as intervortex interactions. Finally, we describe the effects of vortex interactions with sample edges and surface features, which are the main focus of the experimental work in this thesis.

3.1 Vortex characteristics

3.1.1 Vortex magnetic fields and interactions in bulk superconductors

As described previously, a vortex consists of a quantum of magnetic flux, Φ_0 penetrating a region where the superconducting order parameter is reduced to zero. This flux must necessarily be surrounded by a circulating screening current. By combining Maxwell's equation with the second London equation, one obtains an expression for the spatial dependence of the magnetic field in the vortex:

$$\nabla^2\vec{h}-\frac{\vec{h}}{\lambda^2}=-\frac{\Phi_0}{\lambda^2}\hat{z}\delta\left(\vec{r}-\vec{r}_0\right), \tag{3.1}$$

where the center of the vortex is located at r_0. The solution to this equation is given by:

$$h(r)=\frac{\Phi_0}{2\pi\lambda^2}K_0\left(\frac{r}{\lambda}\right). \tag{3.2}$$

where K_0 is a Hankel function and h is directed along the z-axis [1]. The divergence of this expression as r approaches zero is cut off at the coherence length, corresponding to the size of the normal core, as shown in the plot in Figure 3.1. At large distances, h(r) decays exponentially:

$$h(r) \approx \frac{\Phi_0}{2\pi\lambda^2}\left(\frac{\pi}{2}\frac{\lambda}{r}\right)^{1/2} \exp\left(-\frac{r}{\lambda}\right). \tag{3.3}$$

The local magnetic field at the center of the vortex, h(0), can be solved by cutting off the dependence of h(r) for r < ξ, which yields:

$$h(0) \approx \frac{\Phi_0}{2\pi\lambda^2}\ln\kappa. \tag{3.4}$$

or about twice H_{c1}. A more exact calculation involving a numerical integration of the Ginzburg-Landau equations, accounting for the spatial variation of the order parameter in the vortex core yields a small numerical correction to equation 3.4 [2].

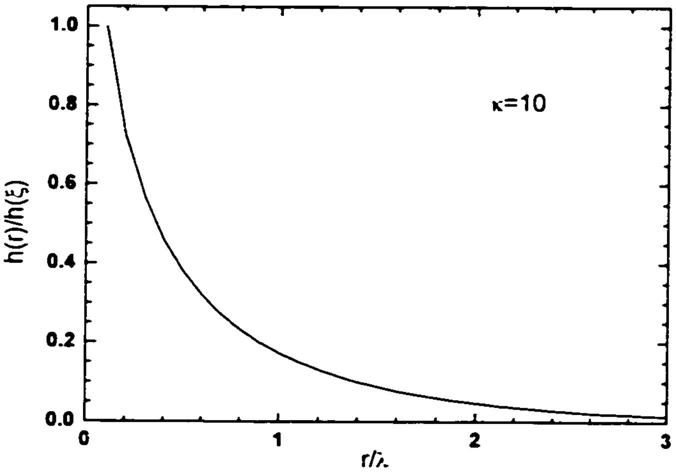

Figure 3.1: Radial dependence of the local magnetic field in a vortex from equation 3.2. The expression diverges in the vortex core, thus the plot is normalized to h(ξ), for κ=10.

Neighboring vortices in a bulk superconductor interact through the screening currents associated with the local magnetic field distribution around a vortex, given by equation 3.2. This interaction energy can be expressed as the product of the flux of vortex #1 with the strength of the magnetic field inside the superconductor due to vortex #2 at the center of vortex #1:

$$F_{12} = \frac{\Phi_0}{4\pi} h_2(r_1) = \frac{\Phi_0^2}{8\pi^2\lambda^2} K_0\left(\frac{r_{12}}{\lambda}\right). \qquad (3.5)$$

Vortices of the same polarity will repel one another in order to minimize this term. From the limit in equation 3.3, it can be seen that this interaction energy will be negligible at large distances. Thus at sufficiently low flux density, such that the intervortex spacing is greater than λ, vortices in a bulk superconductor will not interact significantly [1]. Alternatively, the intervortex interaction can be expressed by considering the net supercurrent flow pattern due to the circulating currents associated with two neighboring vortices as shown by Schmidt [2]. In between the vortices, the currents will cancel, while away from the two vortices, the circulating currents will add, resulting in a Bernoulli pressure pushing the vortices away from each other [2].

When the vortex spacing in a bulk superconductor becomes comparable to the penetration length, the vortices will arrange themselves in order to minimize the repulsive interaction energy. The lowest energy configuration with a stable equilibrium is a triangular lattice. The density of flux lines is proportional to B, $n = B/\Phi_0$, and the intervortex spacing for the triangular arrangement is given by:

$$a_0 = \left(\frac{2}{\sqrt{3}}\right)^{1/2} \sqrt{\left(\frac{\Phi_0}{B}\right)}, \qquad (3.6)$$

where the numerical constant is about 1.075 [1, 3]. The spacing, a_0 is about 0.1μm for B = 2.4 kG.

3.1.2 Vortices in thin-film superconductors

If the thickness of the superconductor, d, is less than the London penetration length, screening supercurrent flow patterns will be altered. Pearl showed that for a superconducting film with d < λ, screening currents flow over the longer thin-film screening length scale:

$$\lambda_\perp \approx \lambda^2/d. \tag{3.7}$$

Pearl also calculated the circulating current flow pattern for a vortex in a thin-film, with the vortex oriented along the thin direction of the superconductor. In contrast to the exponentially decaying expression for a vortex in a bulk superconductor, given by equation 3.3, the thin-film solution exhibits a power-law decay:

$$J_s(r) \approx \left(\frac{c\Phi_0}{4\pi^2 r^2 d}\right),\ r >> \lambda^2/d. \tag{3.8}$$

This slowly decaying screening current distribution results in a power-law decay of the intervortex interaction energy. Thus vortices in a thin-film will interact over much larger distances and form a lattice at much smaller fields than in a bulk superconductor [4].

The local magnetic field distribution above a vortex in a thin-film superconductor can be calculated from the complete expressions for the spatial dependence of the supercurrent in the paper of Pearl [4]. For distances greater than $\lambda_\perp$ away from the vortex core, the local magnetic field above the vortex is effectively that of a magnetic monopole located at the center of the vortex, one effective penetration length below the surface [5-7]. The z-component of this field above the surface, i.e. normal to the surface, for a vortex located at (x_0, y_0), can be expressed as:

$$B_z = \frac{\Phi_0}{2\pi}\frac{z+\lambda_\perp}{\left[(x-x_0)^2+(y-y_0)^2+(z+\lambda_\perp)^2\right]^{3/2}} \tag{3.9}$$

The vortex magnetic field above the surface of a bulk superconductor also exhibits this monopole behavior, as the supercurrent flow pattern is predicted to spread out substantially near the surface, where the vortex exits the superconductor. Thus in a thick superconductor at low flux density, the fields above the vortices can interact at large distances, although the screening current distributions of the vortices in the bulk, beneath the surface, do not overlap significantly [4, 8].

3.1.3 Lorentz Force

A current, with density J, passed through a superconductor in the mixed state will exert a Lorentz force on the vortices in the sample:

$$\vec{f}_L = \vec{J} \times \frac{\vec{\Phi}_0}{c}, \tag{3.10}$$

where f_L is a force per unit length of the vortex and the vector, $\vec{\Phi}_0$ points along the vortex core. At high vortex density, the Lorentz force is commonly expressed as a force density:

$$\vec{F} = \vec{J} \times \frac{\vec{B}}{c}, \tag{3.11}$$

where B is the macroscopic magnetic flux density. If B is perpendicular to J, then the Lorentz force on the vortices will be directed transverse to the direction of current flow. This force is essentially the same as the intervortex interaction force discussed in section 3.1.2, with the circulating supercurrent of one vortex at the location of the second vortex playing the role of J [1, 9, 10].

3.1.4 Flux flow

In an ideal bulk superconductor, with no pinning and no surfaces or edges, any finite Lorentz force will cause the vortices to move. This problem was first treated by Bardeen and Stephen in 1965 [11]. The motion of the magnetic flux of the vortex generates an electric field directed parallel to the applied current which produced the Lorentz force. Because the electric field and applied current point in the same direction, the vortex motion dissipates power, and the material is no longer in the zero resistance state. The electric field generated by the vortex moving with velocity, v_L produces a velocity-dependent damping force, f_{damp}, characterized by a viscosity, η which opposes the Lorentz force:

$$f_{damp} = -\eta v_L = -f_L, \tag{3.12}$$

assuming the mass of the vortex is negligible [2]. Thus if the applied current is maintained, the vortex will move with constant velocity:

$$v_L = \frac{cE}{B}. \tag{3.13}$$

One can then define a flux flow resistivity as the ratio of the electric field and the applied current density:

$$\rho_f = \frac{E}{J}. \tag{3.14}$$

At sufficiently high velocity, an electronic instability can occur when the distance the vortex core moves during the time-scale set by the charge carrier relaxation becomes greater than the size of the vortex core. For these high velocities, the current-voltage characteristic becomes nonlinear and switches out to the normal resistance state [12].

Using the expression for the flow velocity, the flux flow resistivity can be rewritten in terms of the flow viscosity, η, and B:

$$\rho_f = \frac{\Phi_0 B}{c^2 \eta}. \tag{3.15}$$

Thus a larger vortex viscosity results in a lower flux flow resistance, as the vortices move more slowly for a given Lorentz force. A detailed calculation of η is difficult, and must take into account several different damping mechanisms, as discussed by Tinkham [1]. However, by treating the dominant eddy current damping mechanism, one obtains the approximate expression:

$$\eta \approx \frac{\Phi_0 H_{c2}}{\rho_n c^2}, \tag{3.16}$$

where ρ_n is the resistivity of the material in the normal state. Applying this expression to equation 3.15, the flux flow resistivity is given by:

$$\rho_f = \frac{B}{H_{c2}} \rho_n. \tag{3.17}$$

Thus for magnetic fields much less than H_{c2}, the flux flow resistivity will be a small fraction of the normal state resistivity [1, 2, 10]. Equation 3.17 strictly holds only in the limit of isolated, independently moving vortex cores, thus requiring temperatures well below T_c and magnetic fields much less than H_{c2}. When these conditions are violated, $\rho_f(B)$ deviates from the linear dependence and exhibits an upward curvature over a wider range of B as the temperature approaches T_c [13, 14].

3.2 Pinning

3.2.1 Critical current density

As shown above, the application of a transport current to a superconductor in the mixed state will cause the vortices to move, thus dissipating power. Therefore a type-II superconductor should be useless for carrying a supercurrent in any magnetic field above H_{c1} which is typically quite small. However, real samples contain various defects which can exert a force on the vortices opposing the Lorentz force from the applied current. These defects are able to pin the vortices in place up to some critical threshold Lorentz force, thus preventing vortex motion and maintaining the zero resistance state of the material.

The strength of the pinning in a superconductor is characterized by a critical force density, F_c. When the Lorentz force exceeds F_c, the vortices will be pushed off of the pinning sites and dissipation will set in. One can then define a critical current density, J_c from:

$$\vec{F}_c = \vec{J}_c \times \frac{\vec{B}}{c}. \tag{3.18}$$

J_c is typically only a fraction of the depairing current, defined in section 2.2.2. Strong pinning superconductors can have J_c on the order of 10^6A/cm^2, while other materials can have critical current densities which are several orders of magnitude smaller [1, 9].

The current-voltage characteristic for a superconductor with pinning will exhibit a finite zero-voltage supercurrent in an applied magnetic field. Once the transport current density exceeds J_c, vortices will depin and flux flow will occur. Following a small non-Ohmic region related to flux creep effects of the vortices over a distribution of pinning energies, the voltage along the superconductor will increase linearly as the vortices flow with a uniform velocity. The slope of the voltage is given by the flux flow resistivity from equation 3.17 and does not extrapolate through the origin. For large voltages, an instability can occur which switches the superconductor out to the normal state resistance, as discussed above. This normal state resistance does, of course, extrapolate back through the origin [10, 15].

3.2.2 Critical state

The entry of flux into a superconductor with bulk pinning, characterized by J_c provides an illustration of the irreversibility associated with the pinning of vortices. Consider a thick superconducting slab, with thickness $w \gg \lambda$, with an applied magnetic field parallel to the face of the slab, oriented along the z-axis, as shown in Figure 3.2(a). As the applied field is increased from zero, vortices will enter at the faces of the slab. This model assumes no barriers to the entry of flux into the slab, and in the simplest case, H_{c1} is assumed to be zero. These vortices which enter the slab are pinned by defects in the superconductor, thus generating a vortex density gradient along the x direction. From the Maxwell equation, $\vec{J} = \frac{c}{4\pi}\vec{\nabla}\times\vec{B}$, this vortex density gradient must be accompanied by a current flowing parallel to the face and perpendicular to the field direction:

$$J_y = \frac{c}{4\pi}\frac{dB}{dx}. \tag{3.19}$$

When the current J_y exceeds J_c, the vortex density gradient can no longer be sustained. The vortex entry thus proceeds by vortices penetrating into the slab with the maximum possible gradient, corresponding to the critical current density flowing in the vortex-filled regions, with no current flowing in the vortex-free regions in the center of the slab. As the applied field is increased, the vortices penetrate further into the superconductor, maintaining the critical gradient, with current J_c flowing. Bean originally assumed the pinning force to be proportional to B, or equivalently J_c is independent of B [16]. In this case the vortex density profiles are straight lines with slope $^{4\pi J_c}/_{c}$, as shown in Figure 3.2(a) [16]. Later work of Kim assumed that the pinning force was independent of B, thus J_c is proportional to B^{-1}, leading to parabolic profiles for the vortices entering the slab [17]. A similar entry of vortices occurs if the magnetic field is due to the self-field of a transport current applied to the slab, instead of an externally applied magnetic field.

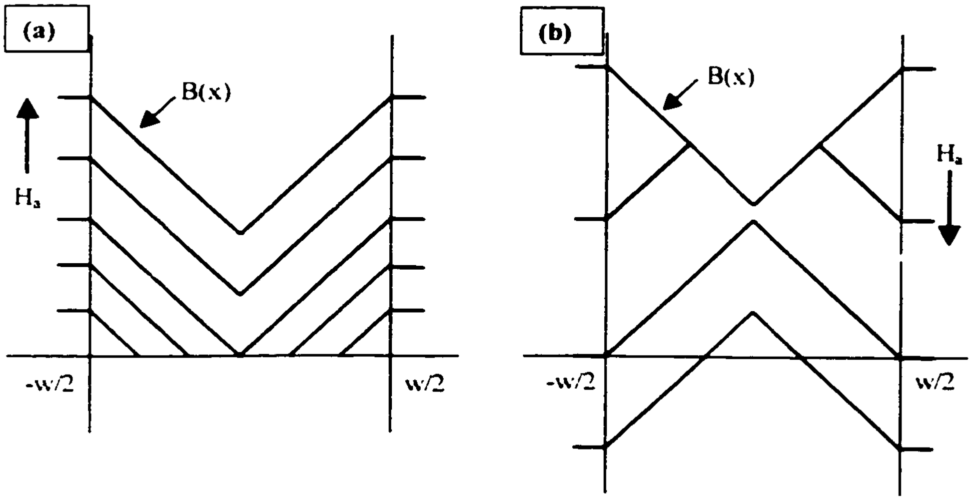

Figure 3.2: (a) Entry of vortices into a superconducting slab in the critical state model. Lines represent flux density, B(x), with slope $4\pi J_c/c$ in the Bean model. (b) Trapped flux upon decreasing applied magnetic field to zero from the fully penetrated flux state.

If the magnetic field is reduced after these vortex profiles are established, the profiles near the faces of the slab will reverse direction at some intermediate location across the width of the slab, as shown in Figure 3.2(b). Once the applied field is reduced to zero, the profile reversal points will not have propagated through all of the vortex-filled regions, thus producing a remanent magnetic moment in the slab. This is manifested in a hysteresis in the magnetization curve for the slab. Because of this irreversibility of the mixed state, materials with substantial pinning are often referred to as "hard" superconductors, in analogy with permanent magnets [1-3, 9]. Richardson, Pla, and Nori studied the dynamics of the vortex profiles in the critical state model of Bean through computer simulations [18].

3.2.3 Pinning mechanisms

At the macroscopic level, pinning produces a critical threshold transport current which a superconductor in the mixed state can sustain with zero resistance. On the microscopic scale, pinning occurs through various defects which provide a favorable place for a vortex to sit. For low flux density and a high pin density, it is possible that each vortex could be captured by a different pinning site, resulting in some amorphous vortex distribution, corresponding to the random distribution of pins. At higher vortex density, only a fraction of the vortices may reside at pinning sites, but these pinned vortices may be capable of restraining the rest of the vortices through the elastic properties of the vortex lattice. The detailed summation of individual pinning forces to obtain the macroscopic critical current density is a difficult problem, but approximations are possible along the way. Several research groups have attempted to measure the elementary pinning force for a single vortex in a superconducting thin film using a variety of techniques, with results covering a large range [19-23].

Because a vortex consists of a normal core surrounded by a circulating supercurrent, a defect in a superconductor can pin a vortex by providing an energetically favorable place for the vortex core or the circulating currents to pass. If the vortex core passes through a non-superconducting defect or a region with a reduced T_c, the system will recover the condensation energy which would have been required to nucleate the vortex in the bulk of the superconductor. For a normal (non-superconducting) inclusion, the core energy per unit vortex length which is saved is:

$$E_{core} = \frac{H_c^2}{8\pi}\left(\pi\xi^2\right). \tag{3.20}$$

where $\pi\xi^2$ is the cross-sectional area of the vortex core. Because this energy varies over a length scale of ξ, the maximum pinning force from such a defect is given by:

$$f_{core} \approx \frac{E_{core}}{\xi}. \tag{3.21}$$

Thus an effective core pinning site must be at least on the order of ξ in size [2, 9]. In addition to normal inclusions, effective core pinning can also be achieved at voids in the sample, where again the system can regain the condensation energy by allowing the normal core to pass through a region which is already normal (or empty, in the case of a void). These voids can either develop naturally during the growth of the sample, or they can be introduced by bombarding the sample with heavy ions [2].

A defect can also pin a vortex by producing a distortion of the circulating supercurrents which flow around the vortex core. Altered current flow patterns can have a lower energy than for a vortex located in the bulk with variations of the potential occuring on the length scale of the penetration depth. For high-κ type II superconductors, the core pinning interaction generally dominates the magnetic interaction of the screening current distortion, although there are situations where the latter mechanism plays an important role [9]. Mkrtchyan treated the problem of a vortex interacting with the interface between two superconducting regions with different values of λ. At the interface, the screening current flow lines of the vortex are diffracted, resulting in an attractive force drawing the vortex towards the interface [24, 25].

Other effective pinning sites include extended defects, such as grain boundaries between different crystal orientations in the superconductor. This mechanism has been studied extensively in the high-T_c cuprates [26]. Also in the cuprates, interfaces between growth islands generated during the film deposition can pin vortices [27].

3.2.4 Elasticity constants and collective pinning theory

An infinitely rigid vortex lattice cannot be effectively pinned by a random distribution of point defects, as different defects will tend to attract the vortex lattice in all different directions, with the net pinning force adding to zero [1, 9]. Thus in order to take advantage of the distribution of pinning sites, the vortex lattice must be able to deform such that vortices can pass through the optimal pinning locations in their vicinity. There is then a competition between the gain in energy from the pinning and the cost of deforming the vortex distribution from the low-energy triangular lattice. For small vortex displacements, this deformation can be best described through the elasticity constants for the vortex lattice. This procedure is described in detail in the book of Campbell and Evetts [15].

The elastic response of the vortex lattice to various orientations of strain is characterized by the group of elastic constants, C_{ij}. If the vortices are oriented along the z-axis, the constants C_{11} and C_{12} correspond to compression modes of the vortex lattice in the x-y plane. The constant, C_{66} relates shear displacements of vortices, also in the x-y plane. For high-κ superconductors, C_{66} is generally smaller than the other constants, thus shear displacements are often the soft mode for deformations of the vortex lattice [15, 28]. Tilt deformations of the vortices, relative to the z-axis are characterized by the elastic constant, C_{44}. For sufficiently thin superconductors placed in a perpendicular magnetic field, i.e. vortices oriented along the thickness direction, tilt deformations given by C_{44}, can be ignored. Approximations of this displacement roughly predict this crossover when the thickness of the superconductor becomes less than about twice the vortex lattice spacing. For thinner films, vortices behave essentially as 2D objects [29].

A model describing the pinning of vortices by a random collection of pinning sites was proposed in 1979 by Larkin and Ovchinnikov [30]. The authors used the elastic response of the vortex lattice to relate the deformations of the lattice to accommodate the available pin distribution. Vortices are assumed to be ordered over a correlation volume, V_c. The radius R_c and height, L_c of this volume are given by the elastic constants discussed above and the strength and density of available pinning sites. A stiffer vortex lattice results in larger correlation lengths, as the lattice is more difficult to deform, while stronger pinning shortens R_c and L_c, since vortices are pulled away from the ordered state more easily. For thin films, L_c can be replaced by the film thickness, d, because tilt deformations can be neglected [1].

When the vortex lattice spacing, a_0 is less than the correlation length, R_c, the system is in the collective pinning regime. The Larkin-Ovchinnikov collective pinning theory was able to explain the unusual peak effect phenomenon which had been observed in many type II superconductors. As the magnetic field is increased, the critical current density, J_c generally decreases monotonically until H_a approaches H_{c2}, where J_c increases suddenly, before dropping to zero at H_{c2} when superconductivity in the bulk is destroyed. The theory showed that a softening of the vortex lattice which allowed the vortices to better accommodate the pinning sites just below H_{c2} could explain the observed increase in J_c [1, 30, 31]. In the opposite limit of low magnetic fields and weak pinning, it is possible for the R_c to be less than a_0. In this case, the vortices are in the individual pinning regime, and the vortices are distributed in an amorphous structure corresponding to the locations of pinning sites [29]. An overview of collective pinning and other vortex-related phenomena in the context of the high-temperature superconductors is contained in the review of Blatter et al. [32].

3.2.5 Flux creep

In addition to depinning caused by transport currents, vortices can also be excited out of pinning sites by thermal activation over the pinning potential barrier. This can lead to a relaxation of flux density gradients, first described by Anderson and Kim as a theory of flux creep [33]. If one assumes an activated distribution of vortex depinning times, a crude derivation of the decay of the magnetization from flux creep processes due to Yeshurun et al. is possible [34]. Assume the time for a vortex to hop out of a pinning well is related to the barrier height, U by:

$$t = t_0 \exp\left(\frac{U}{k_B T}\right). \tag{3.22}$$

Because a current density, J will tend to push a vortex out of a pinning well due to the Lorentz force, the barrier height U should decrease for larger values of J. A simple approximation assumes:

$$U(J) = U_0\left(1 - \frac{J}{J_c}\right). \tag{3.23}$$

More thorough study reveals that U(J) is better described by a non-linear function [35], but for most conventional low-T_c superconductors with J near J_c, the linear approximation is generally sufficient. Combining equation 3.22 and 3.23 gives:

$$J(t) = J_c\left[1 - \frac{kT}{U_0}\ln\left(\frac{t}{t_0}\right)\right]. \tag{3.24}$$

The magnetization of a bulk superconductor is proportional to the screening current density, J, thus equation 3.24 predicts a magnetization decay which is logarithmic in time. Therefore after a sudden change in the applied magnetic field or an externally applied transport current, vortices will hop between pinning sites rapidly at first, but considerably more slowly at longer times. This can also be seen in the decay of the remanent magnetization by first establishing the mixed state then suddenly reducing the applied magnetic field, perhaps all the way to zero. The trapped vortices will try to leave the sample, resulting in a decrease in the sample magnetization, but the vortex flow rate will decrease logarithmically in time. A plot of M against log(t) follows a straight line whose slope depends on the temperature of the measurement, according to equation 3.24. These flux creep phenomena were observed as early as 1963 by Kim et al. [36]. Flux creep can also lead to a non-linear region in the current-voltage characteristic for a superconducting wire or strip above the zero-voltage supercurrent and below the linear flux flow regime [2].

For conventional strong pinning low-T_c superconductors, U_0/k_B can be quite large, on the order of 1000 K. Combined with the low temperatures required for superconductivity, the logarithmic term in equation 3.24 can be rather small. This leads to small flux creep rates, with the magnetization dropping by only a few percent over several hours. However in the high-temperature superconductors, the pinning barriers, U_0 can be much lower, due to the considerably shorter coherence lengths. The lower barriers and the higher operating temperatures lead to significant flux creep effects. Since the discovery of the cuprates, flux creep phenomena have been reinvestigated [34]. Also, recent investigations have addressed the possibility of local modifications of flux creep behavior around surface defects [37, 38].

3.2.6 Thermomagnetic Instability

Due to the power dissipation associated with flux motion, insufficient cooling power can lead to instability problems in current-carrying applications of superconductors. If a fluctuation causes a bundle of vortices to move, the power dissipated by this flux flow can cause a local increase in the temperature. Because J_c decreases at higher temperatures, it can be easier for vortices to depin in the region of the original fluctuation. This can then produce more flux motion and dissipate more power, potentially leading to an avalanche process which can destroy superconductivity completely. If the local heat buildup can be dissipated quickly enough, before more vortices depin due to the lowered J_c, then the system will be stable to these fluctuations. Thus the stability depends on the thermal conductivity of the superconductor and the thermal conductance to the environment, such as the bath or the substrate, as well as the heat capacity of the superconductor [39]. Considerations of flux jump effects are important in the design of high-field superconducting magnets, as these instabilities can cause catastrophic failures [1]. In addition to flux jumps in high-current superconducting wires, thermomagnetic instabilities have recently been observed in the entry of vortices in thin-film superconducting strips [40].

3.3 Vortex interactions with sample edges and surface features

In addition to bulk pinning and interactions between vortices, vortex behavior can be influenced by interactions with the sample edges and with surface features. Near a surface, the vortex screening currents become distorted, resulting in a surface barrier to vortex entry. Depending on the sample geometry, a thin superconductor in a perpendicular magnetic field can have large demagnetizing currents which affect the vortex energy with respect to its distance from the sample edge, leading to a geometrical barrier to flux entry. Both surface and geometrical barriers can produce irreversible magnetization curves even in the absence of bulk pinning, and they have important effects on the transport properties of superconductor samples. Once inside the superconductor, a vortex can interact with surface features, such as steps, through variations in the vortex line energy due to thickness changes. These three interactions, surface and geometrical barriers, as well as step barriers are the main focus of these thesis experiments.

3.3.1 Surface barriers

A surface barrier arises from the interaction of a vortex with the surface of a sample when both the vortex and the applied magnetic field are oriented parallel to the surface. The first treatment of this problem, due to Bean and Livingston, involves computing the composite energy landscape seen by a vortex in the vicinity of the sample surface [41]. The external magnetic field, H_a causes screening currents to flow along the surface of the sample. These currents decay over a penetration depth into the sample and produce a Lorentz force which pushes the vortex into the sample, away from the surface. The energy barrier per unit vortex length corresponding to this force is given by:

$$E_{M}(x_L) = \frac{\Phi_0}{4\pi} H_a \exp\left(\frac{-x_L}{\lambda}\right), \tag{3.25}$$

where x_L is the distance of the vortex into the sample relative to the surface. In order to satisfy the boundary condition of no current flow normal to the sample surface, the circulating current around the vortex must be distorted as the vortex approaches the surface. This is most easily solved with the method of images by placing an image antivortex at $-x_L$, resulting in a potential given by the vortex interaction described in section 3.1:

$$E_I(x_L) = \varepsilon_L - \left(\frac{\Phi_0}{4\pi\lambda}\right)^2 K_0\left(\frac{2x_L}{\lambda}\right). \tag{3.26}$$

where ε_L is the line tension of the vortex in the bulk of the superconductor. The sum of these two energies, E_M and E_I, yields the potential sketched in Figure 3.3. As H_a is increased from zero, there is a potential barrier to vortex entry into the sample. This barrier persists past H_{c1}, when entry of vortices into the bulk is thermodynamically favorable. Vortices do not enter until a larger field, H_p, at which point the surface barrier vanishes. Calculations predict a value for H_p which is on the order of the thermodynamic critical field, H_c. However, surface defects with a spatial extent on the order of λ will result in a value of H_p lower than that predicted by theory [3].

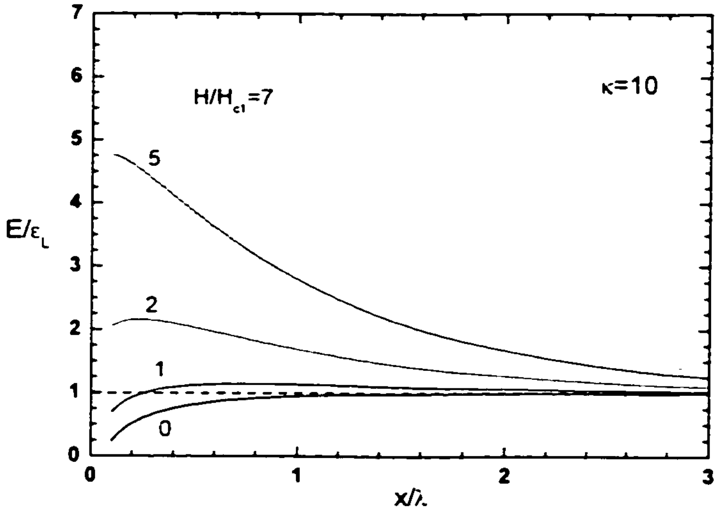

Figure 3.3: Vortex energy as a function of position near the surface of a superconductor, given by equations 3.25 and 3.26. The plots are for a superconductor with κ=10. The expressions break down for $x_L \sim \xi$, where numerical solutions of the GL equations are required.

Once flux has entered the superconductor, if the applied magnetic field is then reduced, vortices will be held inside the sample by the Meissner screening barrier given by equation 3.25. Thus the flux exit is delayed until $H_a = 0$, when the exit barrier vanishes. This leads to hysteresis in the magnetization curve, although with no bulk pinning, the surface barrier alone does not produce a remanent magnetic moment, i.e. on the descending branch, $M = 0$ when $H_a = 0$ [2, 15, 42]. Also, at finite temperatures, it is possible for vortices to be thermally excited over the surface barrier. Thus H_p exhibits a thermally activated decrease with increasing temperature.

3.3.2 Geometrical barriers

A superconducting sample with a large demagnetizing factor can also present a barrier to vortex entry and exit. The Meissner screening in a thin superconducting strip, with $W/d \gg 1$ and $d \gg \lambda$, in a perpendicular magnetic field will produce a substantial distortion of the magnetic field. Because the strip is thicker than the penetration depth, the screening currents corresponding to this distortion flow primarily on the top and bottom surfaces and the variation across the width of the strip can be found from conformal mapping:

$$J_y(x) = \frac{-cH_a}{2\pi d} \frac{x}{\sqrt{(w/2)^2 - x^2}}, \tag{3.27}$$

for x not too close to the strip edge [43]. Thus the screening current is largest at the edges of the strip, but flows across the entire strip width. A similar screening response occurs if a transport current instead of a magnetic field is applied to the strip.

As the applied magnetic field is increased from zero, the curvature and concentration of the field lines at the strip edges causes vortex segments to cut diagonally across the corners of the edge initially, as shown in Figure 3.4. These vortex segments experience a Lorentz force directed towards the center of the strip due to the screening current distribution given by equation 3.27. However, as the tops of the vortex segments are dragged further into the strip, the diagonal vortex segments lengthen, resulting in a larger vortex line energy. This produces an outwardly directed force opposing vortex entry. Vortices do not enter the bulk of the strip until the screening current near the strip edge has stretched the vortex segments to the point at which the line energy is of the order of $\varepsilon_L d$, the energy of a vortex which is entirely in the strip. At this point, the vortex segments snap into the strip and form a complete vortex which threads the entire thickness of the strip [29, 43].

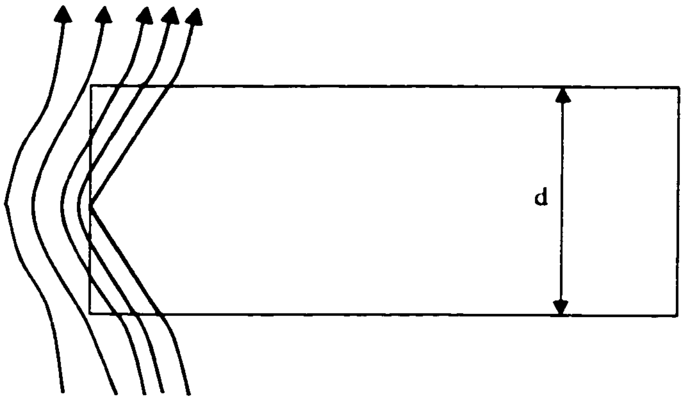

Figure 3.4: Vortices initially cut diagonally across the sample corners in the geometrical barrier model for flux entry, due to the strong curvature of the field lines at the edge of the strip. Thickness of strip, d is greater than the penetration depth, λ.

The traditional treatment of the magnetic response of a superconductor with a large demagnetizing factor involves approximating the sample cross section with an ellipse. Flux entry then occurs when the Gibbs free energy in the center of the strip reaches zero, giving a penetration field, $H_p = H_{c1}(d/W)$. However the geometrical barrier described above predicts a vortex entry field of $H_p \approx H_{c1}\sqrt{2d/W}$. Thus flux entry is delayed with respect to the elliptical cross section response [43].

If the strip contains no bulk pinning, then vortices which enter past the geometrical barrier are immediately swept to the center of the strip by the Lorentz force associated with the screening current distribution given by equation 3.27. This results in a dome-like distribution of vortices in the center of the strip with correspondingly no vortices in the region between the dome and the edge of the strip. This vortex dome has been predicted theoretically and observed experimentally by several groups [29, 43, 44]. As the applied magnetic field is reduced, the vortex dome expands out towards the edge of the strip, while the total amount of flux in the strip remains constant. This delayed flux exit produces hysteresis in the magnetization curve, similar to the Bean-Livingston surface barrier. If the applied field is larger than ~0.5 H_{c1}, then the vortex dome fills almost the entire width of the strip, and vortices exit almost immediately once the field is reduced. Thus in the absence of bulk pinning, the magnetic response will become reversible for larger fields. Unlike the surface barrier, the geometrical barrier is not as sensitive to defects along the sample edge, as the relevant screening currents are distributed over the entire top and bottom surfaces of the strip. Also, the geometrical barrier is not affected by thermal activation, as the energy scale, $\varepsilon_L d >> k_B T$ [42, 43, 45].

It is possible for both surface and geometrical barriers to exist in certain samples, thus moderately thick strips ($d >> \lambda$) can exhibit effects related to both types of barriers. For thin superconducting strips with the thickness less than the penetration depth, the vortices are unable to tilt and effectively behave as two-dimensional objects. Thus the geometrical barrier due to the cutting of vortices across the corners in thicker strips as described above will not be present. However, the surface barrier interaction between the vortices and the edges and the distortion of the screening current flow caused by the strip geometry combine to produce a hybrid effect called an edge barrier [46]. The theory of vortex entry into thin superconducting strips along with our experimental measurements will be discussed further in Chapter 8.

3.3.3 Vortex pinning by surface features

Steps on the surface of a superconductor can pin vortices due to the variation in vortex line energy (equation 2.10) caused by the modulation of the superconductor thickness. A vortex has a lower line energy in a thinner region of a superconductor, leading to an impedance to vortex motion from thin to thick regions, as shown in Figure 3.5.

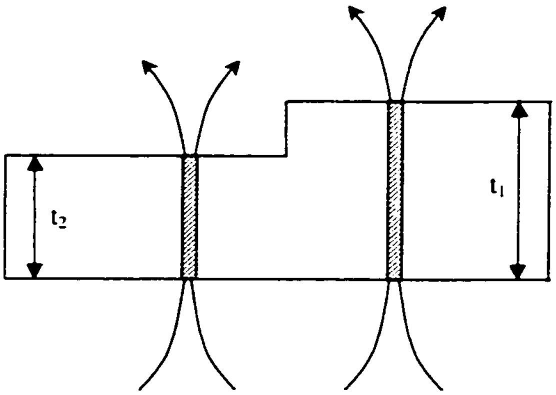

Figure 3.5: Schematic of vortex line energy variation due to thickness change at a surface step. This produces a barrier to vortex motion from thin to thick regions of the superconductor.

This interaction can lead to substantial pinning in thin films with large surface roughness [47, 48] as well as significant distortions of field-cooled vortex distributions [49]. An understanding of vortex surface pinning is necessary to improve the critical currents of superconducting thin films and to control the field-cooled locations of vortices, an important problem in thin film devices, such as SQUIDs. Our Scanning SQUID Microscope measurements of vortex dynamics and distributions near surface steps will be presented in Chapters 6 and 7.

3.4 References

[1] M. Tinkham, *Introduction to Superconductivity* (McGraw-Hill, Inc., New York, 1996).

[2] V. V. Schmidt, *The Physics of Superconductors* (Springer-Verlag, Berlin, 1997).

[3] P. G. de Gennes, *Superconductivity of Metals and Alloys* (Addison-Wesley, Reading, 1989).

[4] J. Pearl, *Current Distribution in Superconducting Films Carrying Quantized Fluxoids*, Appl. Phys. Lett. **5**, 65 (1964).

[5] G. Carneiro and E. H. Brandt, *Vortex lines in films: Fields and interactions*, Phys. Rev. B **61**, 6370 (2000).

[6] A. M. Chang, H. D. Hallen, L. Harriott, *et al.*, *Scanning Hall probe microscopy*, Appl. Phys. Lett. **61**, 1974 (1992).

[7] J. R. Clem, *Two-dimensional vortices in a stack of thin superconducting films: A model for high-temperature superconducting multilayers*, Phys. Rev. B **43**, 7837 (1991).

[8] D. A. Huse, *Magnetic-flux patterns on the surface of a type-II superconductor*, Phys. Rev. B **46**, 8621 (1992).

[9] R. P. Huebener, *Magnetic Flux Structures in Superconductors* (Springer-Verlag, Berlin, 1979).

[10] A. C. Rose-Innes and E. H. Rhoderick, *Introduction to Superconductivity* (Pergamon Press, Oxford, 1978).

[11] J. Bardeen and M. J. Stephen, *Theory of the Motion of Vortices in Superconductors*, Phys. Rev. **140**, A1197 (1965).

[12] A. V. Samoilov, M. Konczykowski, N.-C. Yeh, *et al., Electric-Field-Induced Electronic Instability in Amorphous Mo_3Si Superconducting Films*, Phys. Rev. Lett. **75**, 4118 (1995).

[13] Y. B. Kim, C. F. Hempstead, and A. R. Strnad, *Flux-Flow Resistance in Type-II Superconductors*, Phys. Rev. **139**, A1163 (1965).

[14] P. Berghuis and P. H. Kes, *Two-dimensional collective pinning and vortex-lattice melting in a-$Nb_{1-x}Ge_x$ films*, Phys. Rev. B **47**, 262 (1993).

[15] A. M. Campbell and J. E. Evetts, *Critical Currents in Superconductors* (Taylor and Francis Ltd., London, 1972).

[16] C. P. Bean, *Magnetization of High-Field Superconductors*, Rev. Mod. Phys. **36**, 31 (1964).

[17] Y. B. Kim, C. F. Hempstead, and A. R. Strnad, *Magnetization and Critical Supercurrents*, Phys. Rev. **129**, 528 (1963).

[18] R. A. Richardson, O. Pla, and F. Nori, *Confirmation of the Modified Bean Model from Simulations of Superconducting Vortices*, Phys. Rev. Lett. **72**, 1268 (1994).

[19] O. B. Hyun, D. K. Finnemore, L. Schwartzkopf, *et al., Elementary Pinning Force for a Superconducting Vortex*, Phys. Rev. Lett. **58**, 599 (1987).

[20] L. H. Allen and J. H. Claasen, *Technique for measuring the elementary pinning force in thin films*, Phys. Rev. B **39**, 2054 (1989).

[21] M. J. Goldstein and W. G. Moulton, *Thermally induced flux motion and the elementary pinning force in Nb thin films*, Phys. Rev. B **40**, 8714 (1989).

[22] G. S. Park, C. E. Cunningham, B. Cabrera, *et al., Vortex Pinning Force in a Superconducting Niobium Strip*, Phys. Rev. Lett. **68**, 1920 (1992).

[23] C.-H. Sow, K. Harada, A. Tonomura, *et al., Measurement of the Vortex Pair Interaction Potential in a Type-II Superconductor*, Phys. Rev. Lett. **80**, 2693 (1998).

[24] G. S. Mkrtchyan and V. V. Shmidt, *Interaction Between a Vortex and the Boundary Between Two Sperconductors*, JETP **36**, 352 (1973).

[25] G. S. Mkrtchyan and V. V. Shmidt, *Pinning of a vortex lattice on the interface of two superconductors and the critical current*, JETP **41**, 90 (1975).

[26] G. W. Crabtree, W. K. Kwok, U. Welp, *et al.*, in *Physics and Materials Science of Vortex States, Flux Pinning and Dynamics*, edited by R. Kossowsky, S. Bose, V. Pan and Z. Durusoy (Kluwer Academic, Kusadasi, Turkey, 1998), Vol. 356, p. 357.

[27] B. Dam, J. M. Huijbregste, F. C. Klaasen, *et al.*, *Origin of high critical currents in* $YBa_2Cu_3O_{7-\delta}$ *superconducting thin films*, Nature **399**, 439 (1999).

[28] H. Ullmaier, *Irreversible Properties of Type II Superconductors* (Springer-Verlag, Berlin, 1975).

[29] M. V. Marchevsky, Ph.D. Thesis (Leiden University, Leiden, 1997).

[30] A. I. Larkin and Y. N. Ovchinnikov, *Pinning in Type II Superconductors*, J. Low Temp. Phys. **34**, 409 (1979).

[31] P. H. Kes, in *Physics and Materials Science of Vortex States, Flux Pinning and Dynamics*, edited by R. Kossowsky, S. Bose, V. Pan and Z. Durusoy (Kluwer Academic, Kusadasi, Turkey, 1998), Vol. 356, p. 109.

[32] G. Blatter, M. V. Feigel'man, V. B. Geshkenbein, *et al.*, *Vortices in high-temperature superconductors*, Rev. Mod. Phys. **66**, 1125 (1994).

[33] P. W. Anderson and Y. B. Kim, *Hard Superconductivity: Theory of the Motion of Abrikosov Flux Lines*, Rev. Mod. Phys. **36**, 39 (1964).

[34] Y. Yeshurun, A. P. Malozemoff, and A. Shaulov, *Magnetic relaxation in high-temperature superconductors*, Rev. Mod. Phys. **68**, 911 (1996).

[35] M. R. Beasley, R. Labusch, and W. W. Webb, *Flux Creep in Type-II Superconductors*, Phys. Rev. **181**, 682 (1969).

[36] Y. B. Kim, C. F. Hempstead, and A. R. Strnad, *Flux Creep in Hard Superconductors*, Phys. Rev. **131**, 2486 (1963).

[37] F. Pardo, F. de la Cruz, P. L. Gammel, *et al.*, *Real Space Images of the Vortex Lattice Structure in a Type II Superconductor during Creep over a Barrier*, Phys. Rev. Lett. **79**, 1369 (1997).

[38] B. L. T. Plourde and D. J. Van Harlingen, in *Physics and Materials Science of Vortex States, Flux Pinning and Dynamics*, edited by R. Kossowsky, S. Bose, V. Pan and Z. Durusoy (Kluwer Academic, Dordrecht, 1998), Vol. 356, p. 281.

[39] R. G. Mints and E. H. Brandt, *Flux jumping in thin films*, Phys. Rev. B **54**, 12421 (1996).

[40] P. Esquinazi, A. Setzer, D. Fuchs, *et al.*, *Vortex avalanches in Nb thin films: Global and local magnetization measurements*, Phys. Rev. B **60**, 12454 (1999).

[41] C. P. Bean and J. D. Livingston, *Surface Barrier in Type-II Superconductors*, Phys. Rev. Lett. **12**, 14 (1964).

[42] R. A. Doyle, S. F. W. R. Rycroft, C. D. Dewhurst, *et al.*, in *Physics and Materials Science of Vortex States, Flux Pinning and Dynamics*, edited by R. Kossowsky, S. Bose, V. Pan and Z. Durusoy (Kluwer Academic, Kusadasi, Turkey, 1998), Vol. 356, p. 239.

[43] E. Zeldov, A. I. Larkin, V. B. Geshkenbein, *et al.*, *Geometrical Barriers in High-Temperature Superconductors*, Phys. Rev. Lett. **73**, 1428 (1994).

[44] M. Benkraouda and J. R. Clem, *Magnetic hysteresis from the geometrical barrier in type-II superconducting strips*, Phys. Rev. B **53**, 5716 (1996).

[45] N. Morozov, E. Zeldov, M. Konczykowski, *et al.*, *Geometrical and distributed surface barriers in* $Bi_2Sr_2CaCu_2O_8$, Physica C **291**, 113 (1997).

[46] D. Y. Vodolazov and I. L. Maksimov, *Distribution of the magnetic field and current density in superconducting films of finite thickness*, cond-mat/0001035 (2000).

[47] C. Jooss, A. Forkl, and H. Kronmuller, *Simple model of vortex pinning at rough superconductor surfaces in* $YBa_2Cu_3O_{7-\delta}$ *thin films*, Physica C **268**, 87 (1996).

[48] C. Jooss, A. Forkl, R. Warthmann, *et al.*, *Thickness and roughness dependence of magnetic flux penetration and critical current densities in* $YBa_2Cu_3O_{7-\delta}$ *thin films*, Physica C **266**, 235 (1996).

[49] H. Dai, J. Liu, and C. M. Lieber, *Surface Pinning and Grain Boundary Formation in Magnetic Flux-Line Lattices of* $Bi_2Sr_2CaCu_2O_{8+\delta}$ *High-*T_c *Superconductors*, Phys. Rev. Lett. **72**, 748 (1994).

CHAPTER 4

EXPERIMENTAL TECHNIQUES FOR STUDYING THE MAGNETIC RESPONSE OF SUPERCONDUCTORS

In order to study the vortex distributions and dynamics near surface features and sample edges, we have performed magnetic imaging as well as transport measurements on various superconducting samples. In this chapter, we discuss the various techniques which are available for studying the magnetic response of superconductors. Some of these techniques measure the global response of the superconductor and provide information about the superconducting critical fields, pinning strengths, and the influence of vortex entry barriers. In this context, we discuss the influence of vortex dynamics on the critical current of a superconducting wire or thin strip. Our measurements of the critical current in thin superconducting strips will be presented in Chapter 8. Other experimental approaches, such as magnetic imaging, detect the local flux behavior in the superconductor. We review most of the available magnetic imaging techniques, including the Scanning SQUID Microscope which is best suited for our vortex imaging experiments near surface steps and edges.

4.1 Magnetization

Early studies of the response of superconductors to magnetic fields involved measurements of the bulk magnetization, providing evidence for the Meissner effect. Bulk magnetization measurements still play an important role for investigations of vortex dynamics in superconducting samples. As discussed in Chapter 2, the magnetization of a type-II superconductor in an applied magnetic field decreases in magnitude as the applied field is increased beyond the diamagnetic magnetization peak, where vortices first enter the sample. Neglecting surface barriers and demagnetizing effects, this flux entry occurs when the applied field reaches the lower critical field, H_{c1}, as the formation of vortices in the superconductor becomes energetically favorable. This magnetization can be hysteretic with applied field due to the presence of bulk pinning, Bean-Livingston surface barriers, or geometrical barriers [1]. Careful measurements of the hysteresis in the $M(H_a)$ response and the magnitude of the remanent moment as the applied field is reduced to zero can be used to extract the strength of bulk pinning and the influence of surface barriers in a superconducting sample. Also, studies of the temporal relaxation of the superconductor magnetization can probe the dynamics of vortices and provide information about the distribution of pinning energies and the nature of intervortex interactions in the sample [2].

4.1.1 Inductive technique

The first measurements of the magnetization of superconductors were performed by monitoring the change in the response of a coil surrounding the sample as the superconductor developed a diamagnetic magnetization to screen an applied magnetic field. The most common approach involves two counter-wound coils, one of which encircles the sample, while the other coil is empty. The current to a solenoid surrounding the system is swept, applying a slowly varying external magnetic field to the superconductor and the coils. Because of the oppositely wound coil polarities, the response of the coils to the external field will cancel out, so that the output signal will be directly proportional to the time rate of change of the sample magnetization. By running this output into an electronic integrator, one obtains a voltage corresponding to the magnetization. The output can be calibrated by measuring a superconductor in a small applied field and assuming perfect diamagnetism, such that $M = -H/4\pi$ [3]. While straightforward to implement, this technique lacks sensitivity. Also, the requirement of a time-varying magnetic field can be a limitation to measurements of vortex dynamics and magnetic relaxation.

4.1.2 SQUID magnetometry

More recently, the development of Superconducting Quantum Interference Devices (SQUIDs) has greatly improved the resolution available for magnetization measurements. Conventional commercial SQUID magnetometer systems use a dc SQUID, unparalleled in flux sensitivity, to read-out the flux from a series of superconducting coils. The sample is mechanically translated along the axis of the coils, which are typically wound in a gradiometer configuration. Any magnetic moment of the sample generates a response in the coils which can be fit using a computer to the response of an ideal point dipole moving through the same region. This then provides a direct measurement of the sample magnetization. A superconducting field coil surrounds the system for applying magnetic fields, making possible the measurement of $M(H)$. Unlike the inductive technique described earlier, the SQUID magnetometer has the advantage of being able to measure the sample magnetization in static or even zero applied magnetic field.

SQUID magnetometers have been useful in studying the nature of vortex matter in the high-T_c superconductors. Recent SQUID measurements have revealed a magnetization jump in the field-temperature phase diagram of the cuprates, corresponding to a first-order melting of the vortex lattice into a liquid [4, 5]. The temporal decay of the remanent state in the cuprates has also been measured using SQUID magnetometers, yielding important information about flux creep and the distribution of pinning energy scales [2]. While the SQUID does have excellent flux sensitivity, one must be careful to account for any field inhomogeneities when interpreting measurements of superconducting samples. Because the sample is physically moved through the detector coils, any spatial field variations seen by the sample during its translation will produce spurious values for the measured moment, due to the magnetic hysteresis present in most superconducting samples. The effects of this problem can be reduced by attempting to eliminate trapped flux in the superconducting magnet and by minimizing the distance over which the sample is translated [2].

4.1.3 Torsion oscillators

The sample magnetization can also be studied by measuring the torque about some pivot axis between the sample magnetic moment and the applied magnetic field. This torque is most easily detected by mounting the sample on the end of a flexible cantilever such that the sample can oscillate through small angles about the equilibrium position. As the sample magnetization varies, the capacitively-detected response of the cantilever to an oscillatory drive will change. With knowledge of the sample geometry and the applied field orientation, it is possible to compute the sample magnetization from the torque measurement. For a superconducting sample, one can extract the bulk pinning strength, J_c, by measuring the change in torque for increasing and decreasing field sweeps [6].

Torsion oscillators can be operated over a wide temperature range and the sample magnetization can be measured quickly, typically in less than 1 second. This relatively short acquisition time is an advantage over SQUID magnetometers which require significantly more time to perform a measurement, as the sample must be translated through the pickup coils multiple times and the results averaged and fit. The torsion oscillator technique has been used to characterize the pinning strengths in YBCO thin films under a wide variety of growth conditions, leading to an understanding of the nature of pinning defects in cuprate films [7].

Torque magnetometry generally must be performed with large applied magnetic fields, as the interaction of the magnetic moment with the applied field must produce a large enough torque on the cantilever to be detected by the readout scheme. This requirement prevents the study of low-field magnetization, or the decay of the remanent state in zero-field. Also, conventional torque magnetometers have at least two orders of magnitude less sensitivity than a SQUID system [6]. However, much smaller oscillators, with dimensions in the range of 10μm - 100μm, have been made recently using silicon micromachining technology. The magnetization is detected by measuring the resonance frequency, in the range of 45 kHz, which shifts as the torque on the oscillator changes. The greater sensitivity of these micromechanical oscillators has permitted measurements of single vortex entry and dynamics in single crystals of $NbSe_2$ [8].

4.2 Transport

The behavior of vortices in superconductors can also be probed by measuring transport properties. As discussed in Chapter 3, a transport current exerts a Lorentz force per unit length on vortices:

$$\vec{f}_L = \vec{J} \times \frac{\vec{\Phi}_0}{c} \quad . \tag{4.1}$$

The motion of vortices generates a longitudinal voltage, transverse to the direction of vortex flow. The magnitude of this voltage is proportional to the flow velocity. Because the generated electric field is parallel to the current exerting the Lorentz force, the motion of vortices dissipates energy. Thus in the absence of any bulk pinning or entry barriers, any finite current will move vortices causing dissipation, so that there would be no true superconducting state when vortices are present [9]. In practical samples, the vortices are held in place, up to some threshold Lorentz force, with bulk pinning and forces related to geometrical and surface barriers. This threshold force then defines a finite critical current, below which the sample will exhibit zero resistance.

Transport measurements of a superconducting wire or strip can thus probe the vortex interaction with the bulk pinning and entry barriers. A typical current-voltage characteristic (IVC) for a type-II superconducting wire is shown in Figure 4.1.

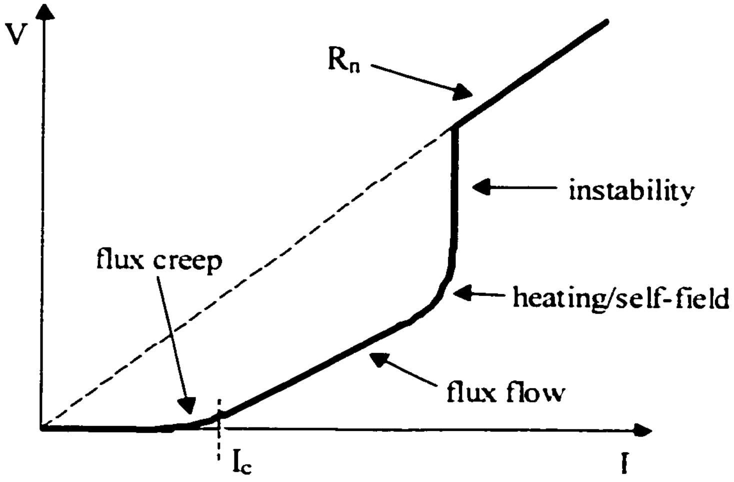

Figure 4.1: Representative current-voltage characteristic (IVC) for a type-II superconducting wire or thin strip in a transverse magnetic field. For small magnetic fields, the IVC for a thin strip can exhibit extra structure arising from demagnetizing effects and defects along the strip edges. The thin strip response will be discussed further in Chapter 8.

Just below the threshold critical current, flux creep processes can generate small voltages with a non-Ohmic response. This temperature dependent vortex motion is sometimes referred to as Thermally Activated Flux Flow (TAFF) [9]. For currents beyond the critical current, the vortices begin to flow uniformly, producing a voltage with a constant differential resistance. If the magnetic field is close to zero, the IVC for thin strips with vortex entry barriers in this low current regime can exhibit extra structure. At large currents, the voltage dependence can deviate from the linear flux flow slope and can increase more quickly, appearing as a curved region in the IVC. Often this curvature is due to Joule heating, however in thin superconducting strips, it is possible to have a curved region in the IVC caused by the self-field of the transport current at the strip edges. Calculations and measurements of the IVC for thin superconducting strips will be presented in Chapter 8. For still larger currents, the vortex flow velocity and the corresponding voltage increase further, and an instability can occur due to the increasing dissipation. This switches the sample out to the normal resistance state, thus the wire or strip is no longer superconducting [10].

4.2.1 Critical current

By measuring the critical current of a superconducting sample, one can probe the forces experienced by vortices in the sample. As described above, the superconductor can develop small voltages due to thermally activated motion of vortices, particularly at the high temperatures near T_c in the cuprates, making the determination of the critical current somewhat arbitrary. The critical current is typically defined as the current at which the longitudinal voltage reaches a predetermined threshold, usually in the range of a few μV [10]. This voltage is measured in a conventional 4-terminal configuration, as shown in Figure 4.2. By applying the current through remote leads, the current flow pattern is uniform along the long axis of the sample in the region in which the voltage is being measured. The voltage leads are typically spaced by 0.1mm - 10mm and are connected to a low-noise, high gain differential amplifier, permitting the detection of subμV levels. The measurement is performed by slowly increasing the applied current, usually over several seconds, until the threshold voltage is exceeded. This procedure is commonly run with a computer data acquisition system, which allows for repeated readings of the critical current which can then be averaged. The external conditions of the sample, such as the temperature or applied magnetic field, can be varied between critical current acquisitions, providing a measure of $I_c(T)$ or $I_c(H_a)$. The critical current measured with the above procedure is often called the static critical current.

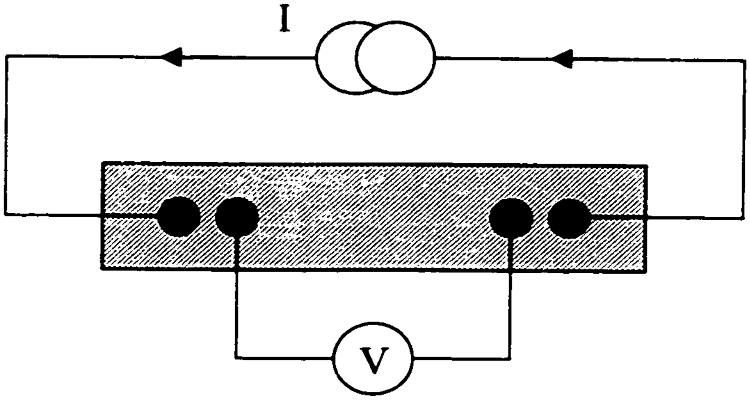

Figure 4.2: 4-terminal configuration for measuring longitudinal voltages in a superconducting sample. No current flows along the voltage leads, so the voltage measurement is independent of the lead and contact resistances. The magnetic field would be applied perpendicular to the page, so that vortex flow across the strip width would produce a longitudinal voltage.

Another technique measures the dynamic critical current by recording the entire IV characteristic, then fitting the linear flux flow region and extrapolating back though zero voltage [11]. For small magnetic fields and low temperature, these techniques will yield quite similar values for the critical current. However, in the other limits, the actual supercurrent region of the IV curve can be very small and flux creep processes can add substantial curvature below the flux flow region. This can lead to different values for the static and dynamic critical currents, thus one must be careful to specify which quantity is being measured.

In order to interpret the critical current measurements, one must account for the influence of surface and geometrical barriers on the vortex dynamics. At low fields, when the self-field due to the transport current is greater than or comparable to the applied magnetic field, the entry barriers, treated in Chapter 3, can dominate the vortex behavior. These barriers, which are most significant in samples with a large demagnetizing factor, such as thin strips with the field applied along the thickness direction, can cause the sample to have a finite critical current, even when the sample contains no bulk pinning. Clem and Benkraouda have computed the variation of the critical current with applied magnetic field for a thin superconducting strip with no bulk pinning [12]. In the limit of large magnetic fields, geometrical effects are less important, and vortices penetrate more uniformly across the width of the sample. In this regime, the measured critical current can be used to determine the pinning force experienced by vortices in the bulk of the sample [10].

4.2.2 Flux flow

Information about the superconductor can also be obtained from measurements in the flux flow regime, once the critical current has been exceeded. Measurements of the flux flow resistance by Kim et al. provided one of the early indications that flux was indeed carried by quantized vortices in type-II superconductors [13]. Kim observed that strips made from the same superconductor with the same geometry but different defect concentrations had different critical currents in the same magnetic field, as strips with more defects possessed stronger pinning and thus larger critical currents. However, although the strips had different critical currents, the flux flow resistance in a given field was the same for the different strips. For low temperatures and magnetic fields well below H_{c2}, the flux flow resistance in the strips was also measured as a function of the applied magnetic field, and was found to follow the form:

$$\frac{\rho_f}{\rho_n} = \frac{B}{H_{c2}}, \tag{4.2}$$

where ρ_n is the normal state resistivity and H_{c2} is the upper critical field [13]. This dependence was first predicted by Bardeen and Stephen and was discussed in Chapter 3 [14]. Thus the flux flow regime appears to depend primarily on the intrinsic properties of the superconductor, ρ_n and H_{c2}, and not on the strength of defect pinning in the material. At temperatures closer to T_c and for larger magnetic fields, intervortex interactions become significant and the $\rho_f(B)$ dependence deviates from the linear behavior and curves upwards [13, 15].

However, subsequent measurements as well as more detailed treatments showed that in certain materials, pinning can have some influence on the flux flow behavior, as the pinning can introduce a spread in the distribution of vortex flow velocity [10]. The true flux flow resistance can be studied by going out to larger currents, where residual pinning effects do not play a role. Kunchur et al. used a pulsed current technique to probe the free flux flow regime near T_c in YBCO thin films [16]. The pulsed currents were necessary in order to minimize Joule heating due to the high dissipation levels. While not as severe at lower currents, these heating effects can still play a role, thus most studies of flux flow are performed with the sample and leads immersed in liquid helium, for optimum cooling.

Investigations of the transport properties of flowing vortices are useful for studying many properties of the vortex dynamics. Measurements of the differential resistance, dV/dI, are often performed with a lock-in technique, where a small ac modulation is superimposed on the dc transport current. Studies of the flux flow have recently addressed nonlinearities in the flux flow properties [17] as well as steps in the current-voltage curves [18] arising from interactions between the vortex motion and the underlying electronic structure in the superconductor. Transport measurements have also been used to observe the melting of the vortex lattice in YBCO crystals [19].

4.3 Magnetic Imaging

While bulk measurements, such as magnetization and transport, can yield much information about vortex properties, it can often be quite useful to image the flux distributions directly. By imaging vortices, it is possible to study local flux behavior and interactions between vortices and isolated defect structures. Several imaging techniques are available, each one having capabilities which make it advantageous in different experimental situations.

4.3.1 Bitter Decoration

Some of the earliest images of the vortex lattice in a type-II superconductor were obtained by Träuble and Essmann in 1968 using Bitter decoration [20]. The Bitter decoration technique produces images of magnetic field distributions when small ferromagnetic particles are evaporated from a metal filament and are deposited on the sample. In the presence of a small pressure of inert gas, the magnetic particles form small clusters which follow the field gradients and deposit preferentially in regions of high magnetic field on the sample surface. The decoration process takes on the order of one second. The resulting distribution of particles can then be imaged in a Scanning

Electron Microscope (SEM), where the difference in conductivity between the magnetic particles and the sample surface produces contrast variations in the image [21].

Bitter decoration provides high spatial resolution, limited by the magnetic cluster size, typically around 10nm. Figure 4.3 contains a decoration image of the vortex lattice in a PbIn sample. Images can also cover a large area, set by the field of view of the SEM. One drawback to this technique is the destruction of the sample. Once the sample is decorated, it is coated with magnetic particles, generally preventing further study of the sample. Also, only one image can be obtained in an experimental run. Bitter decoration is primarily limited to images of static flux distributions, although several recent studies have imaged slowly moving vortex patterns. By applying field gradients to a superconductor, it is possible to drive vortices slowly so that the vortex motion during the decoration time is less than a few lattice spacings. Thus moving vortices appear as streaks in the decoration images. This technique has been used to image correlated channel flow of moving vortices in $NbSe_2$ [22] and to study the motion of vortices around surface steps, also in $NbSe_2$ [23].

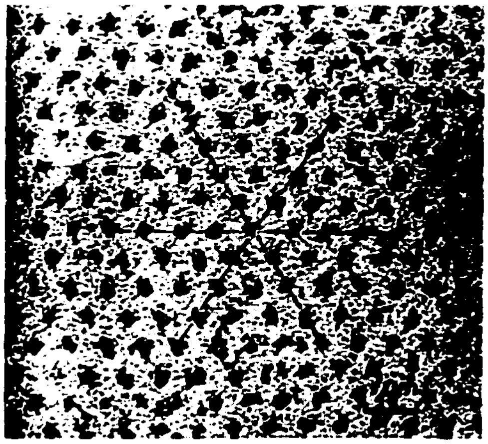

Figure 4.3: Bitter decoration image of vortex lattice in superconducting PbIn cylinder in the remanent state, with $B \approx 70$ G, at $T=1.2$ K (from Träuble and Essmann, 1968, p.4053).

4.3.2 Magneto-optical imaging

Magneto-optical techniques utilize the field-dependent Faraday effect to produce images of the magnetic field distribution at the sample surface. In magneto-optically (MO) active materials. the polarization of incident light is rotated through an angle determined by the local magnetic field strength and the Verdet constant of the material. To image flux distributions in a superconductor. a MO film with a metallic mirror layer is placed on the superconductor surface. The sample is then illuminated with optical wavelength polarized light. which reflects off the mirror and passes through a series of polarization filters. Any polarization rotation due to magnetic field variations at the sample surface produces contrast variations in the optical microscope image. as depicted in Figure 4.4 [24].

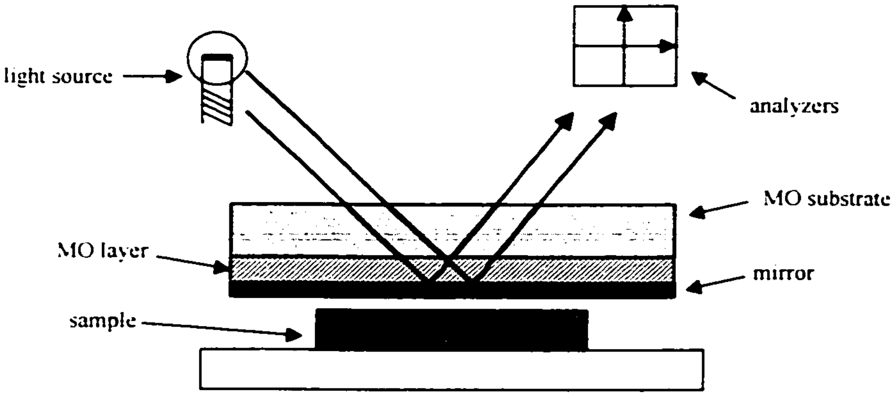

Figure 4.4: Schematic arrangement of sample. MO layer. and incident light in a magneto-optical imaging system. An optical microscope after the cross-polarizers provides the images (after Koblischka and Wijngaarden. 1995. p. 201).

MO imaging provides decent spatial resolution of about 0.5µm. as determined by the wavelength of light used. The images can be obtained quickly. making possible nearly real-time studies of flux dynamics. The MO technique also works over a wide temperature range. allowing for studies of flux distributions in the cuprates near the high superconducting transition temperatures. The most significant limitation of MO imaging is the low field sensitivity of 0.1G. which prevents the resolution of individual vortices [24. 25]. However. much useful information about flux distributions and dynamics can still be obtained [25. 26]. including images of the field distribution in current-carrying strips patterned from superconducting YBCO films [27].

4.3.3 Neutron Diffraction

It is also possible to study the vortex lattice with diffraction techniques. thus providing information about the vortex distribution in k-space. A superconductor in the mixed state will diffract an incident beam of neutrons due to the scattering of the neutron moment from the magnetic fields of the vortices [28]. The resulting diffraction peaks are related to the order and symmetry of the vortex lattice. in a similar manner to the correspondence between x-ray diffraction and crystal structure. Analysis of the diffraction peak shape leads to values for the vortex lattice correlation lengths related to shear and compressive displacements. Measurement of the rocking curves provides a measure of the longitudinal correlation length due to tilt displacements of the vortex lattice.

Neutron diffraction was recently used to study the structure of the vortex lattice in superconducting Nb crystals near the peak effect. For magnetic fields close to the upper critical field. H_{c2}. some superconducting samples exhibit a peak in the critical current as a function of magnetic field. Neutron diffraction measurements have confirmed theoretical models which predict that the vortex lattice should become disordered near the peak effect field. thus allowing the vortex distribution to deform to fit optimally into the available pinning sites in the sample. resulting in a larger critical current [29]. Because neutron diffraction is not a real-space imaging technique. it is not possible to study local interactions of vortices with isolated defects. Also, neutron diffraction is ineffective at low magnetic fields, where the vortex density available for scattering neutrons is small. Finally, these measurements can only be performed at a sophisticated neutron source facility, of which there are only a few in the world.

4.3.4 Lorentz Microscopy

Lorentz microscopy can produce high-resolution images of vortices in superconductors with high acquisition rates. A field-emission Transmission Electron Microscope (TEM) is used to generate a coherent beam of electrons. When a thin superconducting sample is placed in the electron beam, electrons passing through the sample are deflected different amounts depending on the local magnetic field. The transmitted electrons form an image of the flux distribution in a defocused plane below the sample, with sufficient contrast to resolve individual vortices for moderate fields (< 150 G) [30, 31].

Because of the fast raster scans of the TEM, images can be obtained at up to 30 frames per second, making possible real-time images of vortex motion [32]. This technique has been used to study the dynamics of vortices near thickness variations in thin Nb samples, where vortices order along the thin side of surface steps and are sometimes observed to move along the steps [30]. Lorentz microscopy studies of vortex lattice melting in BSCCO have also been performed [32]. This technique is limited by the requirement of extremely thin samples and the need for complex equipment to produce the coherent electron beam.

4.3.5 Scanning Tunneling Microscopy

The Scanning Tunneling Microscope (STM) can be used to image vortices in a superconductor by monitoring the change in conductance as the metal tip passes between superconducting regions and the non-superconducting vortex cores. In a STM, electrons can tunnel across a vacuum barrier between the metallic tip and a conducting sample when the tip is held at distances of less than one Ångstrom above the sample surface. This height regulation along with the scanning of the tip over the sample surface are achieved with sensitive piezoresistive actuators. Because the tunnel current depends exponentially on the tip-sample separation, it is possible to obtain images of the surface electronic structure with Ångstrom resolution [33]. By applying an ac modulation to the tunneling bias voltage, it is possible to scan the tip and measure the spatial variation of the differential conductance. This quantity is directly related to the local electronic density of states. Hess obtained the first STM images of vortices in superconducting $NbSe_2$ by measuring this local density of states as a function of position. The local variation in the superconducting energy gap provides high contrast images of the vortex cores [34].

Because the STM images are generated by the vortex electronic structure and not by the local vortex magnetic fields, the STM can probe the vortex structure on the electronic coherence length scale rather than the magnetic penetration length scale. In the cuprates, the penetration length can be over 100 times larger than the coherence length, thus the STM provides the highest spatial resolution possible for vortex imaging. This high resolution makes it possible to obtain images in large magnetic fields, up to several Tesla, where the intervortex spacing can be less than 50nm.

By using the STM to study the local density of states, the nature of the quasiparticle distribution in and around the vortex core can also be probed. In 1964, Caroli et al. predicted the existence of bound fermionic states in the vortex core at energies below the superconducting gap [35]. Measurements of the differential conductance on $NbSe_2$ in the mixed state revealed low energy conductance peaks near the center of the vortex core, confirming the existence of these bound states [34]. Conductance curves obtained with the STM tip positioned away from the vortex core show a conventional BCS gap structure, while when the tip is over the vortex core, bound state peaks are observed. The STM can also be used to obtain topographic information from a superconductor surface in addition to the differential conductance. This combination has been used to study the interaction of vortices with pinning sites, such as columnar defects resulting from ion bombardment in $NbSe_2$ crystals [36].

The STM is limited to a small scan range of typically a few microns or less at low temperatures. This makes the STM unsuitable for studying vortex dynamics in superconducting structures which have been patterned from thin films. The most significant drawback of the STM is the requirement of extremely clean sample surfaces, such that a stable vacuum tunneling current can be established. This restricts the variety of superconductors which can be studied with STM. After unsuccessful attempts by many groups to image the vortex lattice in the high-temperature superconductor, YBCO, using an STM, Maggio-Aprile et al. were able to obtain rough vortex images [37]. Many recent experiments have shown that the order parameter in the cuprates possesses d-wave symmetry [38]. The nature of the vortex core in a d-wave superconductor has been studied theoretically, with predictions of unusual vortex core structure due to the induction of subdominant order parameters near the superconductor-vortex core interface

[39-41]. Measurements of the differential conductance around YBCO vortex cores may reveal important information about this response of an unconventional superconducting order parameter near an interface.

4.3.6 Magnetic Force Microscopy

The Magnetic Force Microscope (MFM) scans a small mechanical cantilever with a magnetic tip across the sample surface. Interactions between the tip magnetic moment and the local magnetic field on the sample surface result in a deflection of the cantilever. By monitoring this deflection of the tip using either optical interferometry [42] or piezoresistive sensing [43], it is possible to map out the local magnetic field distribution. Spatial resolutions of 0.1μm are possible, depending on the radius of the magnetic tip on the cantilever. The field resolution is on the order of 0.1 G/Hz$^{1/2}$, limited by the detection resolution of cantilever deflections. This makes it possible to image vortices in superconductors, although the vortex contrast in most images is not particularly impressive. The vortex lattice in $NbSe_2$ has been imaged with MFM by Volodin et al. [43], although only over a few micron square area, limited by the scan range of the piezo-tube used to scan the magnetic tip. Moser et al. imaged vortices in a YBCO film at 77K and observed evidence for the existence of a disordered vortex glass [44].

The usefulness of the MFM for studying vortices is limited by the perturbative interaction between the tip moment and the vortex fields which can disturb vortex distributions in weak-pinning superconductors [43]. This interaction also makes a quantitative analysis of MFM images difficult, as one must deconvolve the magnetic field distribution of the tip from the images [45]. The spatial resolution and the perturbative nature of MFM can be improved by developing spatially sharper magnetized regions at the scanning tip [43]. Eventually, emerging fabrication techniques may make it possible to attach a single magnetic nanoparticle to the end of a cantilever, thus producing a highly localized magnetic moment for scanning.

4.3.7 Scanning Hall Probe Microscopy

Scanning Hall Probe Microscopy (SHM) produces magnetic field images by scanning a small Hall bar across the sample surface. Variations in the local magnetic field shift the Hall voltage across the sensor. The Hall bar is typically fabricated from a semiconductor heterostructure, with active regions as small as 0.25μm x 0.25μm. By keeping the Hall bar within a micron of the sample surface, submicron spatial resolution is possible. The sensor height regulation is often achieved by monitoring the tunnel current from a conducting tip near the region of the substrate containing the Hall sensor [46]. Detection of the tunnel current can be used to obtain the background plane of a sample. Once measured, this plane can then be used to regulate the sensor height with a piezoelectric actuator so that scanning can take place at a fixed height above the surface. Using this technique, 25μm x 25μm images can be obtained at up to 1 frame/second, making possible measurements of vortex dynamics [47]. For sensors with a large Hall resistance, it is possible to obtain field resolutions down to 1mG/Hz$^{1/2}$. The SHM can also operate at higher temperatures, making possible imaging of vortex lattice melting in high-T_c BSCCO crystals [48].

One drawback to some SHM designs is the relatively small scan range of a few microns, limited by the displacement of the traditional piezo-tube scanner. New innovations have extended the scan range up to 1mm through the use of long piezoelectric benders [49]. Hall probes have also been used to study vortices without scanning, where an array of Hall probes is fixed in place across the surface of a superconductor. The individual Hall probes can be between 10μm^2 and 2500μm^2 in active area and are typically spaced by 10μm-100μm. These Hall probe arrays thus provide a measurement of B(x) across the sample as parameters such as applied magnetic field or temperature are varied. This technique has been used to study the dynamics of vortices interacting with the geometrical barrier in thin platelet superconducting samples of BSCCO [50] and $NbSe_2$ [51].

4.3.8 Scanning SQUID Microscopy

For our vortex imaging experiments, we have used a Scanning SQUID Microscope (SSM) to map out the local flux distribution on the sample surface. The SSM uses a dc Superconducting Quantum Inteference Device (SQUID), the most sensitive detector of magnetic flux available. For typical SSM systems, the local flux is detected by a small superconducting pickup loop which couples the flux signal back to the SQUID through a superconducting flux transformer, as shown schematically in Figure 4.5 [52, 53]. With this arrangement, the SQUID dimensions can be optimized for the best flux sensitivity, while the spatial resolution of the SSM is set by making the pickup loop as small as possible and by maintaining a small separation above the sample surface. There are some SSM systems which do not operate in this manner, but rather generate images from the sample flux which is coupled directly into the SQUID washer. These directly-coupled scanners mostly use high-T_c superconductor SQUIDs, where the fabrication difficulties make it impractical to build a multi-layer device with a separate pickup loop and flux transformer [54, 55].

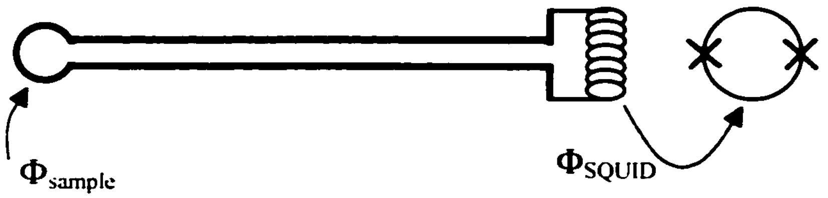

Figure 4.5: Schematic of superconducting pickup loop and flux transformer in a SSM.

The spatial resolution of the SSM is determined by the size of the flux coupling region, or the superconducting pickup loop in most designs. Typical low-T_c pickup loops are between 4μm and 10μm in diameter. In order for the pickup loop to image the flux distribution effectively, it must be kept within one loop diameter of the sample surface during the scan. Most existing designs are able to maintain a pickup loop-sample separation of 1μm-5μm [53]. The primary advantage of the SSM for magnetic imaging is the unparalleled flux sensitivity, which can be down to $10^{-6}\ \Phi_0/\mathrm{Hz}^{1/2}$, corresponding to a field resolution exceeding $10\mu\mathrm{G/Hz}^{1/2}$ for a 10μm pickup loop [52]. The SSM is restricted to operation in relatively low magnetic fields (< 10 G), as a large magnetic field can swamp the flux signal in the SQUID and may exceed the critical field of the superconducting electrodes which comprise the SQUID. Also, it is difficult to operate low-T_c SSM systems at elevated temperatures, as the SQUID and pickup loop must be held below the T_c of their constituent superconducting layers. For Nb devices, this critical temperature is 9 K. However, by carefully isolating the sample and SQUID, and thermally anchoring the SQUID and pickup loop to a 4.2 K bath, SSM systems can be made which allow for the sample temperature to be raised to 100 K, while maintaining the SQUID Nb layers below 9 K [56]. We discuss the design and operation of our SSM in Chapter 5.

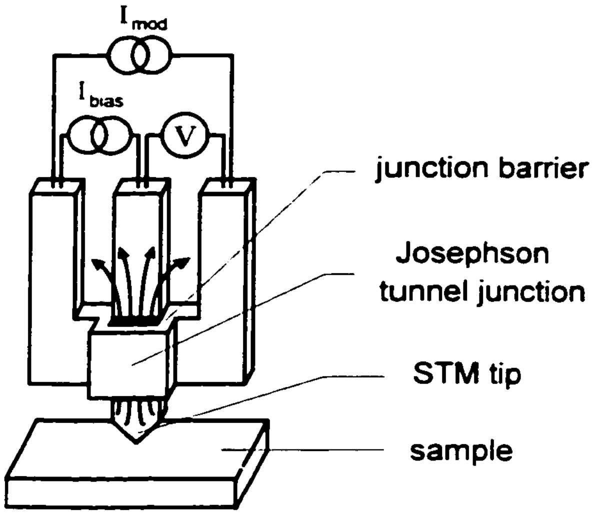

Figure 4.6: Schematic of SJJM, showing the orientation of the junction relative to the sample surface.

We are in the process of developing a new type of SSM, which scans a single Josephson junction fabricated near a Scanning Tunneling Microscope tip. This device, which we call the Scanning Josephson Junction Microscope (SJJM) should have a spatial resolution limited by the size of the junction. The junction can have an effective pickup area of less than $0.1\mu m^2$ and can be scanned within $0.1\mu m$ above the sample surface by the STM height regulation, as shown schematically in Figure 4.6. The single junction exhibits a Fraunhofer single-slit diffraction pattern with applied magnetic field, making possible a similar operation scheme to the conventional 2-junction dc SQUID. Simulations of the SJJM response for a $1\mu m$ x $0.1\mu m$ junction pickup area scanned over a distribution of 3 vortices are shown in Figure 4.7. This response is compared to the output of a SSM scan with a $5\mu m$ pickup loop over the same region, where the individual vortex images become blurred together, due to the larger pickup area of the SSM [57].

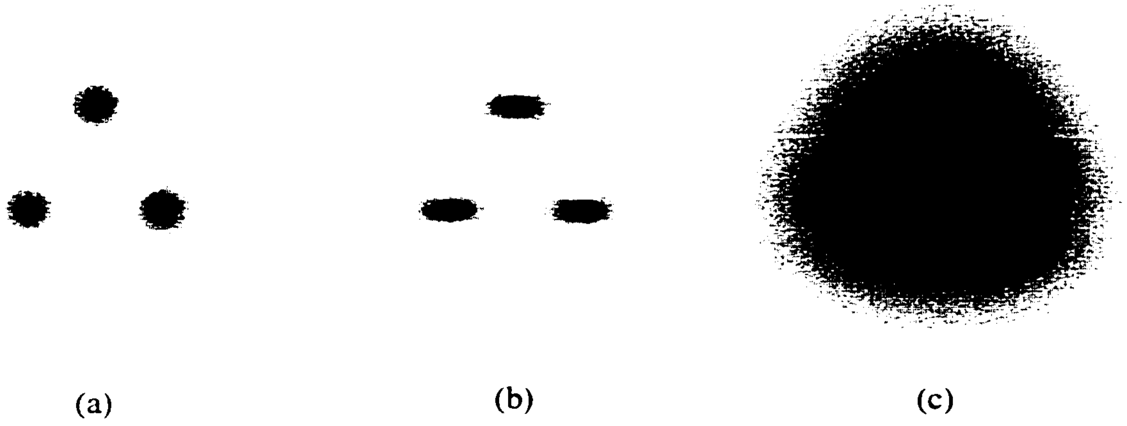

Figure 4.7: Simulated images of three vortices, separated by 3.46μm, corresponding to a magnetic flux density of 2 G. The scan area is 10μm x 10μm.

(a) Vertical component of the magnetic field, B_z.

(b) Calculated SJJM image for a 1μm x 1μm junction scanned at a height of 0.2μm.

(c) Calculated SSM image for a 5μm diameter SQUID loop scanned at a height of 2μm.

4.3.9 Summary of magnetic imaging techniques

From the above descriptions, one can see that each of the available magnetic imaging techniques has an application for which it is best suited. For rapid acquisition of large-scale flux distributions, Magneto-optical imaging is ideal, while for imaging individual vortices with the highest sensitivity, the SSM works best. Figure 4.8 shows a comparison of these imaging techniques by plotting the magnetic field sensitivity vs. the spatial resolution of each system. Diagonal lines indicate constant flux sensitivity so that techniques with the best flux resolution will fall in the lower left corner of the graph. Thus for imaging vortices where fast scan speed is not a requirement, the ultimate imaging technique would be the one located closest to the lower left corner of the graph.

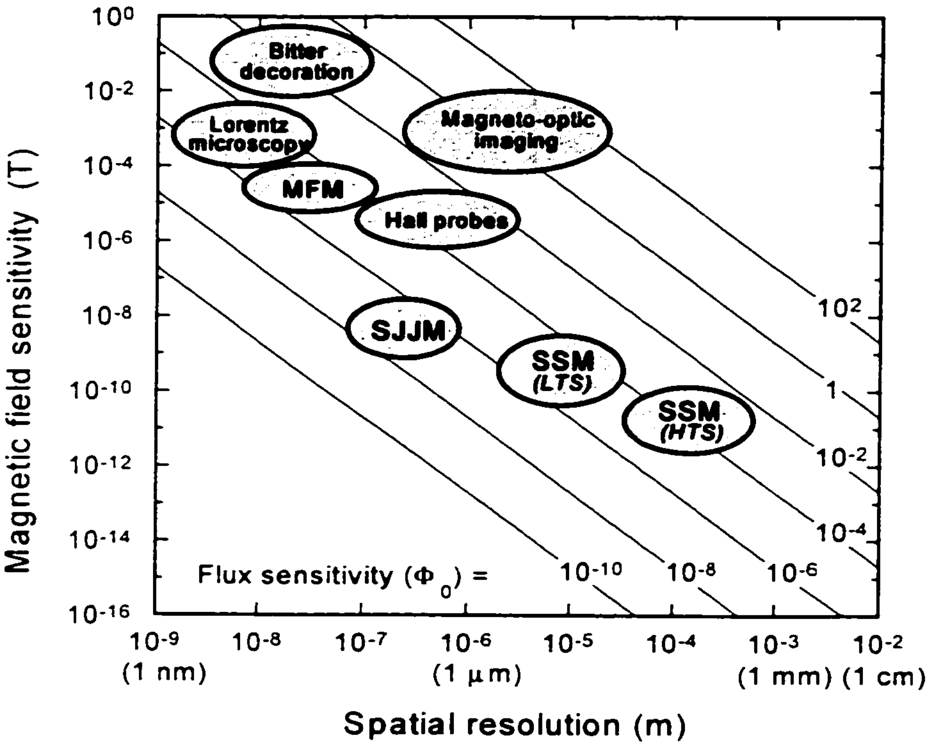

Figure 4.8: Comparison of magnetic imaging techniques.

4.4 References

[1] R. A. Doyle, S. F. W. R. Rycroft, C. D. Dewhurst, *et al.*, in *Physics and Materials Science of Vortex States, Flux Pinning and Dynamics*, edited by R. Kossowsky, S. Bose, V. Pan and Z. Durusoy (Kluwer Academic, Kusadasi, Turkey, 1998), Vol. 356, p. 239.

[2] Y. Yeshurun, A. P. Malozemoff, and A. Shaulov, *Magnetic relaxation in high-temperature superconductors*, Rev. Mod. Phys. **68**, 911 (1996).

[3] A. C. Rose-Innes and E. H. Rhoderick, *Introduction to Superconductivity* (Pergamon Press, Oxford, 1978).

[4] U. Welp, J. A. Fendrich, W. K. Kwok, *et al.*, *Thermodynamic evidence for a flux line lattice melting transition in YBCO*, Phys. Rev. Lett. **76**, 4809 (1996).

[5] G. W. Crabtree, W. K. Kwok, U. Welp, *et al.*, in *Physics and Materials Science of Vortex States, Flux Pinning and Dynamics*, edited by R. Kossowsky, S. Bose, V. Pan and Z. Durusoy (Kluwer Academic, Kusadasi, Turkey, 1998), Vol. 356, p. 357.

[6] M. Qvarford, K. Heeck, J. G. Lensink, *et al.*, *Microtorquemeter for magnetization measurements on small superconducting samples*, Rev. Sci. Inst. **63**, 5726 (1992).

[7] B. Dam, J. M. Huijbregste, F. C. Klaasen, *et al.*, *Origin of high critical currents in* $YBa_2Cu_3O_{7-\delta}$ *superconducting thin films*, Nature **399**, 439 (1999).

[8] C. A. Bolle, V. Aksyuk, F. Pardo, *et al.*, *Observation of mesoscopic vortex physics using micromechanical oscillators*, Nature **399**, 43 (1999).

[9] M. Tinkham, *Introduction to Superconductivity* (McGraw-Hill, Inc., New York, 1996).

[10] H. Ullmaier, *Irreversible Properties of Type II Superconductors* (Springer-Verlag, Berlin, 1975).

[11] V. V. Schmidt, *The Physics of Superconductors* (Springer-Verlag, Berlin, 1997).

[12] M. Benkraouda and J. R. Clem, *Critical current from surface barriers in type-II superconducting strips*, Phys. Rev. B **58**, 15103 (1998).

[13] Y. B. Kim, C. F. Hempstead, and A. R. Strnad, *Flux-Flow Resistance in Type-II Superconductors*, Phys. Rev. **139**, A1163 (1965).

[14] J. Bardeen and M. J. Stephen, *Theory of the Motion of Vortices in Superconductors*, Phys. Rev. **140**, A1197 (1965).

[15] P. Berghuis and P. H. Kes, *Two-dimensional collective pinning and vortex-lattice melting in a-*$Nb_{1-x}Ge_x$ *films*, Phys. Rev. B **47**, 262 (1993).

[16] M. N. Kunchur, D. K. Christensen, and J. M. Phillips, *Observation of Free Flux Flow at High Dissipation Levels in* $YBa_2Cu_3O_{7-\delta}$ *Epitaxial Films*, Phys. Rev. Lett. **70**, 998 (1993).

[17] F. Lefloch, C. Hoffman, and O. Demolliens, *Nonlinear flux flow in TiN superconducting thin film*, Physica C **319**, 258 (1999).

[18] O. M. Stoll, S. Kaiser, R. P. Huebener, *et al.*, *Intrinsic Flux-Flow Resistance Steps in the Cuprate Superconductor* $Nd_{2-x}Ce_xCuO_y$, Phys. Rev. Lett. **81**, 2994 (1998).

[19] W. K. Kwok, S. Fleshler, U. Welp, *et al.*, *Vortex lattice melting in untwinned and twinned single crystals of YBCO*, Phys. Rev. Lett. **69**, 3370 (1992).

[20] H. Träuble and U. Essmann, *Flux-Line Arrangement in Superconductors Revealed by Direct Observation*, J. Appl. Phys. **39**, 4052 (1968).

[21] M. V. Marchevsky, Ph.D. Thesis (Leiden University, Leiden, 1997).

[22] M. Marchevsky, J. Aarts, P. H. Kes, *et al.*, *Observation of the Correlated Vortex Flow in* $NbSe_2$ *with Magnetic Decoration*, Phys. Rev. Lett. **78**, 531 (1997).

[23] F. Pardo, F. de la Cruz, P. L. Gammel, *et al.*, *Real Space Images of the Vortex Lattice Structure in a Type II Superconductor during Creep over a Barrier*, Phys. Rev. Lett. **79**, 1369 (1997).

[24] M. R. Koblischka and R. J. Wijngaarden, *Magneto-optical investigations of superconductors*, Supercond. Sci. Technol. **8**, 199 (1995).

[25] V. K. Vlasko-Vlasov, G. W. Crabtree, U. Welp, *et al.*, in *Physics and Materials Science of Vortex States, Flux Pinning and Dynamics*, edited by R. Kossowsky, S. Bose, V. Pan and Z. Durusoy (Kluwer Academic, Kusadasi, Turkey, 1998), Vol. 356, p. 205.

[26] U. Welp, T. Gardiner, D. O. Gunter, *et al.*, *Reply to Comment of Duran et al.*, Phys. Rev. Lett. **74**, 3713 (1995).

[27] M. E. Gaevski, A. V. Bobyl, D. V. Shantsev, *et al.*, *Magneto-optical study of magnetic-flux penetration into a current-carrying high-temperature-superconductor strip*, Phys. Rev. B **59**, 9655 (1999).

[28] D. Cribier, B. Jacrot, L. M. Rao, *et al.*, *Mise en Evidence par Diffraction de Neutrons d'une Structure Periodique du Champ Magnetique dans le Niobium Supraconducteur*, Phys. Lett. **9**, 106 (1964).

[29] P. L. Gammel, U. Yaron, A. P. Ramirez, *et al.*, *Structure and Correlations of the Flux Line Lattice in Crystalline Nb through the Peak Effect*, Phys. Rev. Lett. **80**, 833 (1998).

[30] K. Harada, H. Kasai, T. Matsuda, *et al.*, *Real-Time Observation of the Interaction between Flux Lines and Defects in a Superconductor by Lorentz Microscopy*, Jpn. J. Appl. Phys. **33** (1994).

[31] K. Harada, T. Matsuda, J. Bonevich, *et al.*, *Real-time observation of vortex lattices in a superconductor by electron microscopy*, Nature **360**, 51 (1992).

[32] K. Harada, T. Matsuda, H. Kasai, *et al.*, *Vortex Configuration and Dynamics in $Bi_2Sr_{1.8}CaCu_2O_x$ Thin Films by Lorentz Microscopy*, Phys. Rev. Lett. **71**, 3371 (1993).

[33] G. Binnig, H. Rohrer, C. Gerber, *et al.*, *Surface Studies by Scanning Tunneling Microscopy*, Phys. Rev. Lett. **49**, 57 (1982).

[34] H. F. Hess, R. B. Robinson, R. C. Dynes, *et al.*, *Scanning-Tunneling Microscope Observation of the Abrikosov Flux Lattice and the Density of States near and inside a Fluxoid*, Phys. Rev. Lett. **62**, 214 (1989).

[35] C. Caroli, P. G. de Gennes, and J. Matricon, *Bound Fermion States of a Vortex Line in a Type II Superconductor*, Phys. Lett. **9**, 307 (1964).

[36] S. Behler, S. H. Pan, P. Jess, *et al.*, *Vortex Pinning in Ion-Irradiated $NbSe_2$ Studied by Scanning Tunneling Microscopy*, Phys. Rev. Lett. **72**, 1750 (1994).

[37] I. Maggio-Aprile, C. Renner, A. Erb, *et al.*, *Direct Vortex Lattice Imaging and Tunneling Spectroscopy on $YBa_2Cu_3O_{7-\delta}$*, Phys. Rev. Lett. **75**, 2754 (1995).

[38] D. J. Van Harlingen, *Phase-sensitive tests of the symmetry of the pairing state in the high-temperature superconductors - Evidence for $d_{x^2-y^2}$ symmetry*, Rev. Mod. Phys. **67**, 515 (1995).

[39] M. Ichioka, N. Hayashi, N. Enomoto, *et al.*, *Vortex structure in d-wave superconductors*, Phys. Rev. B **53**, 15316 (1996).

[40] A. J. Berlinsky, A. L. Fetter, M. Franz, *et al.*, *Ginzburg-Landau Theory of Vortices in d-Wave Superconductors*, Phys. Rev. Lett. **75**, 2200 (1995).

[41] G. E. Volovik, *Superconductivity with lines of gap nodes: density of states in the vortex*, JETP Lett. **58**, 469 (1993).

[42] Y. Martin, D. Rugar, and H. K. Wickramasinghe, *High-resolution magnetic imaging of domains in TbFe by force microscopy*, Appl. Phys. Lett. **52**, 244 (1988).

[43] A. Volodin, K. Ternst, C. V. Haesendonck, *et al.*, *Observation of the Abrikosov vortex lattice in NbSe2 with magnetic force microscopy*, Appl. Phys. Lett. **73**, 1134 (1998).

[44] A. Moser, H. J. Hug, I. Parashikov, *et al.*, *Observation of Single Vortices Condensed into a Vortex-Glass Phase by Magnetic Force Microscopy*, Phys. Rev. Lett. **74**, 1847 (1995).

[45] H. J. Hug, B. Stiefel, P. J. A. v. Schendel, *et al.*, *Quantitative magnetic force microscopy on perpendicularly magnetized samples*, J. Appl. Phys. **83**, 5609 (1998).

[46] A. M. Chang, H. D. Hallen, L. Harriott, *et al.*, *Scanning Hall probe microscopy*, Appl. Phys. Lett. **61**, 1974 (1992).

[47] A. Oral, S. J. Bending, and M. Henini, *Real-time Scanning Hall Probe Microscopy*, Appl. Phys. Lett. **69**, 1324 (1996).

[48] A. Oral, J. C. Bernard, S. J. Bending, *et al.*, *Direct Observation of Melting of the Vortex Solid in* $Bi_2Sr_2CaCu_2O_{8+\delta}$, Physical Review Letters **80**, 3610 (1998).

[49] J. Siegel, J. Witt, N. Venturi, *et al.*, *Compact large-range cryogenic scanner*, Rev. Sci. Instrum. **66**, 2520 (1995).

[50] E. Zeldov, A. I. Larkin, V. B. Geshkenbein, *et al.*, *Geometrical Barriers in High-Temperature Superconductors*, Phys. Rev. Lett. **73**, 1428 (1994).

[51] Y. Paltiel, D. T. Fuchs, E. Zeldov, *et al.*, *Surface barrier dominated transport in* $NbSe_2$, Phys. Rev. B **58**, R14763 (1998).

[52] L. N. Vu and D. J. Van Harlingen, *Design and Implementation of a Scanning SQUID Microscope*, IEEE Trans. Appl. Supercond. **3**, 1918 (1993).

[53] J. R. Kirtley and J. John P. Wikswo, *Scanning SQUID Microscopy*, Annu. Rev. Mater. Sci. **29**, 117 (1999).

[54] F. C. Wellstood, Y. Gim, A. Amar, *et al.*, *Magnetic Microscopy using SQUIDs*, IEEE Trans. Appl. Supercond. **7**, 3134 (1997).

[55] T. S. Lee, Y. R. Chemla, E. Dantsker, *et al.*, *High-T_C SQUID Microscope for Room Temperature Samples*, IEEE Trans. Appl. Supercond. **7**, 3147 (1997).

[56] J. R. Kirtley, C. C. Tsuei, K. A. Moler, *et al.*, *Variable sample temperature scanning superconducting quantum interference device microscope*, Appl. Phys. Lett. **74**, 4011 (1999).

[57] B. L. T. Plourde and D. J. Van Harlingen, *Design of a Scanning Josephson Junction Microscope for Submicron-Resolution Magnetic Imaging*, Rev. Sci. Inst. **70**, 4344 (1999).

CHAPTER 5

SCANNING SQUID MICROSCOPY

The Scanning SQUID Microscope (SSM) provides the best flux sensitivity of the available magnetic imaging techniques, making the SSM ideal for imaging vortices in low fields and studying the dynamics of individual vortices. At the core of the SSM is a dc SQUID coupled to a superconducting pickup loop. In order to obtain high-quality images, the pickup loop height above the sample surface must be carefully regulated. Other important considerations include a scan mechanism which can position the pickup loop with sub-μm resolution, as well as sample temperature control.

In this chapter, we discuss the design, construction, and operation of the SSM used in our study of vortex interactions with sample edges and surface features. The first SSM in our lab was built by a previous graduate student, Lan Vu, and was used to study vortices in superconducting wire networks [1, 2]. The SSM used in the imaging experiments in this thesis was designed and built by Mark Wistrom, a graduate student who investigated vortices in Josephson junction arrays [3]. Other SSM systems have been used to study order parameter symmetry effects in rings of the high-temperature superconductors containing Josephson junctions [4].

5.1 SQUIDs

5.1.1 Operation and design

The excellent flux sensitivity of the SSM is achieved by using a dc SQUID (Superconducting Quantum Interference Device) to detect the magnetic flux from the sample surface. The dc SQUID consists of 2 Josephson junctions in parallel forming a phase-coherent loop. Each Josephson junction has a thin insulating tunnel barrier, separating the neighboring superconducting electrodes. The superconducting state in the electrodes is characterized by a macroscopic quantum wavefunction with a well defined phase. If the phase difference across the junction is varied, the critical current of the junction exhibits oscillations which are 2π-periodic in this phase difference. In the dc SQUID, magnetic flux applied transverse to the SQUID loop winds the phase of the superconducting wavefunction, and causes the SQUID response to exhibit oscillations similar to double-slit diffraction patterns from optics experiments. These oscillations can be observed as a modulation in the critical current of the SQUID with a period of Φ_0, the superconducting flux quantum, as shown in Figure 5.1.

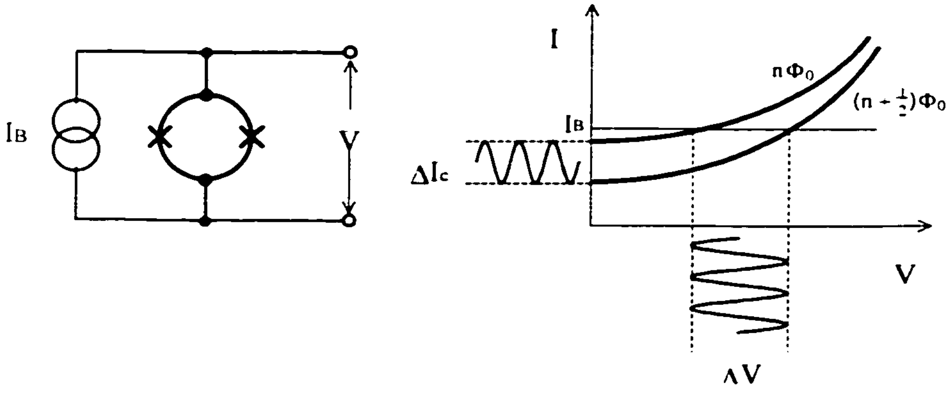

(a) (b)

Figure 5.1: (a) Schematic of dc SQUID - two Josephson junctions, in parallel in a superconducting loop. (b) Critical current of SQUID is periodic in Φ_0, thus flux modulation will produce modulated voltage output.

The SQUID is operated with a dc current bias just above the zero flux critical current, while an ac modulation flux is applied to the SQUID loop. The modulated output voltage is phase-sensitively detected and the dc level is fed back to the flux input, thus maintaining a constant amount of flux in the SQUID loop. This linearizes the output voltage and extends the dynamic range [5, 6]. The useful frequency range of dc SQUIDs which are operated in a flux-locked loop is limited to frequencies below the modulation frequency, typically in the range of several 100 kHz.

The flux-locked loop modulation scheme requires the SQUID current-voltage characteristic to be non-hysteretic. This is achieved by making the junctions in the SQUID loop over-damped, as determined by the damping parameter:

$$\beta_c = \frac{2\pi I_c R^2 C}{\Phi_0} < 1 . \tag{5.1}$$

The critical current and capacitance are set by the geometry and barrier of the junction, so the damping is typically implemented by adding a normal metal shunt resistor in parallel with each junction. This lowers R in equation 5.1, maintaining $\beta_c<1$ [5]. While providing the necessary damping, these resistors also generate noise in the device. The simplest model for the noise in a dc SQUID assumes that the dominant source is Nyquist noise fluctuations in the shunt resistors which couple flux noise into the SQUID loop. It is then possible to compute the noise energy in the SQUID, which determines the energy resolution of an optimized device:

$$\varepsilon(f) \approx 16 k_B T \sqrt{\frac{LC}{\beta_c}} . \tag{5.2}$$

This quantity exhibits a flat spectrum for frequencies well below the Josephson frequency, several GHz for typical operating voltages, and above the low frequency 1/f region. The 1/f noise can be caused by charges trapping at defect sites in the tunnel barrier and by thermally activated motion of flux trapped in the superconducting electrodes. For typical low-T_c dc SQUIDs, the 1/f cutoff extends out to a few Hz and is usually not an issue for SSM imaging, where the SQUID signal is sampled at much higher frequencies. The sampling rate in our SSM system is 20kHz. However 1/f noise can be a problem for measurements of low-frequency signals, especially in biomagnetic and geomagnetic systems.

From equation 5.2, it appears that the energy resolution of the SQUID can be improved by lowering the temperature and by minimizing L and C. The quantity β_c is constrained to be less than one, as shown in equation 5.1. The junction capacitance is minimized by making the junction area as small as possible with the available lithographic patterning techniques. Computer simulations of the SQUID response indicate that making L too small can actually cause the noise energy to increase [6]. The inductive properties of the dc SQUID are characterized by the screening parameter:

$$\beta = \frac{2LI_c}{\Phi_0}, \tag{5.3}$$

where I_c is the critical current of each junction. The energy resolution from these simulations exhibits a minimum for $\beta \approx 1$. In practical SQUID design, the SQUID loop size is chosen to provide sufficient inductance in order to effectively couple the input flux into the SQUID. The junction fabrication parameters are then adjusted to produce critical currents such that β is about one. A typical low-T_c dc SQUID has a loop inductance of a few 100 pH [7]. Besides the noise sources described above, SQUID performance can also be degraded by resonant modes in the SQUID loop and in the modulation and feedback coil. These resonances can be reduced by adding normal metal damping resistors.

5.1.2 SQUID fabrication

Our SSM uses a custom thin film Nb trilayer dc SQUID which we fabricate in our cleanroom facilities. With this style of device, the Josephson junctions have Nb for both superconducting electrodes with an Al_2O_3 tunnel barrier. Because Nb is a refractory metal, Nb trilayer SQUIDs are quite robust, and can withstand many thermal cycles without degradation. The Nb trilayer process, shown schematically in Figure 5.2 consists of four fabrication steps:

(1) A trilayer is deposited through a lithographically defined pattern onto a Si or sapphire substrate. The trilayer consists of a dc sputtered Nb layer, roughly 100nm thick, followed by an Al layer which wets the Nb surface, forming a uniform layer which is on the order of 10nm thick. The Al surface is then oxidized by introducing oxygen gas into the vacuum chamber, typically at a pressure of 0.1 - 1.0 Torr for 5 - 15 minutes. Longer oxidation times and higher oxygen pressures produce a deeper oxide in the Al, causing the junctions to have a lower critical current. After oxidation, a second layer of about 50nm of Nb is sputtered on top of the oxidized Al. This procedure is executed in one vacuum system, and the substrate is not removed until the trilayer deposition is complete.

(2) Junction regions are lithographically patterned on top of the trilayer. In the area surrounding the junction, the top Nb of the trilayer is selectively removed by Reactive Ion Etching in CF_4 and O_2. Thus the junctions consist of complete trilayer, while the adjacent regions only have the base Nb and oxidized Al layers. These regions are filled in with sputtered SiO_2 to isolate the junctions, using the same lithographic mask in a self-aligned process.

(3) The metal layer is deposited into the pattern for the shunting and damping resistors. Typically an alloy of Cu and Au is used and is deposited by thermal evaporation.

(4) A wiring layer of Nb is sputtered into a pattern defining the contact to the tops of the junctions as well as the feedback and modulation coil.

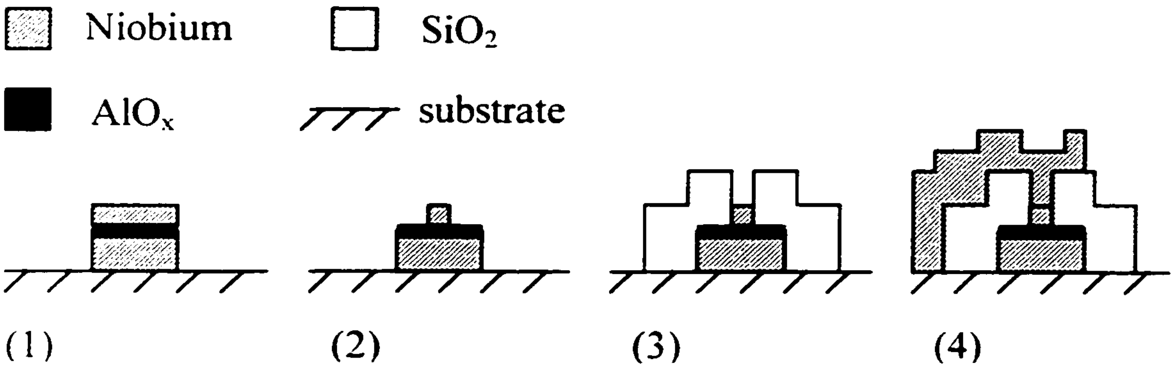

Figure 5.2: Schematic of Nb trilayer process. (1) Deposition of Nb/AlO$_x$/Nb trilayer. (2) Top Nb of trilayer is etched in RIE to define junction region. (3) Etched region is back-filled with SiO$_2$ insulation to isolate junction. (4) Deposition of top Nb wiring layer to make contact to top of junction.

5.1.3 Device parameters

Figure 5.3(a) contains a picture of one of the SQUIDs used in our SSM. The hole in the SQUID washer is 100μm wide. and the single-turn modulation and feedback coil can be seen just beyond the inner perimeter of the washer. This single-turn coil is easier to fabricate than a multi-turn design and provides adequate SQUID performance. The picture in Figure 5.3(b) shows a close-up of the end of the SQUID washer showing the two junctions. each 2μm x 2μm in area. The Cu/Au shunt and damping resistors are off to the sides of the junctions. Our SQUIDs have critical currents of about 50μA. while the shunt resistors are each about 5Ω. The loop inductance of the SQUID washer is 0.5nH. We operate our SQUIDs with a Quantum Design dc SQUID controller (Model 550). This provides a modulation at 500kHz and provides the necessary circuitry for locking onto the SQUID signal and providing feedback. The voltage across the SQUID is coupled to the room temperature amplifier through a cold transformer, providing impedance matching.

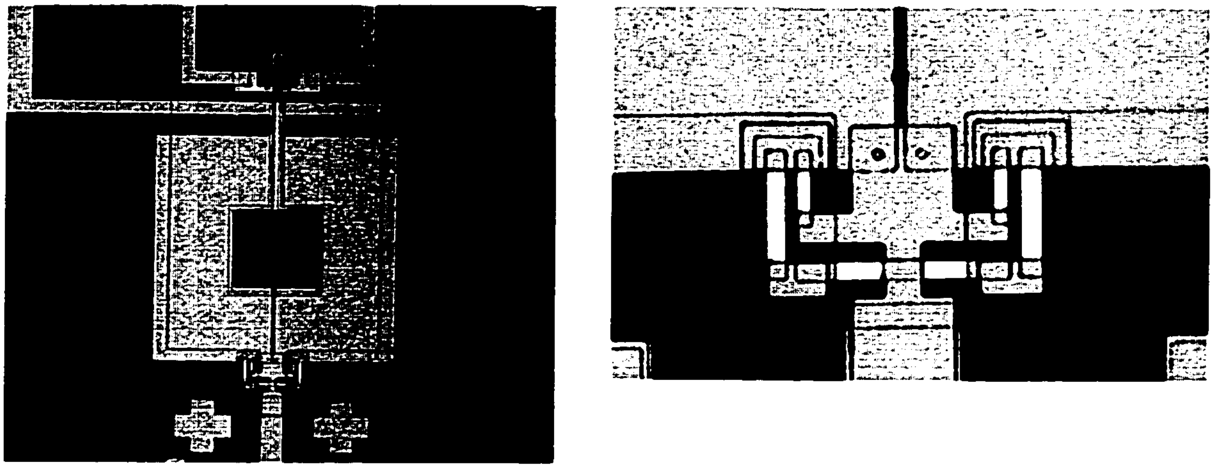

Figure 5.3: (a) Picture of one of our Nb tri-layer SQUID - hole in washer is 100μm wide. (b) Closeup of Josephson junctions - 2μm x 2μm, shunting and damping resistors are off to the sides of the junctions.

5.2 Pickup loop

5.2.1 Design of pickup loop and flux transformer structures

The spatial resolution of the SSM is determined by the size of the pickup loop and its height above the sample surface. As discussed in Section 4.3.8, the ideal SSM design has a superconducting pickup loop which is inductively coupled to the remote SQUID. Magnetic features on the sample surface generate a flux in the pickup loop which is relayed to the SQUID along a superconducting flux transformer. With this arrangement, the pickup loop can be made small, typically 4μm - 10μm in diameter, and can be scanned in close proximity to the sample surface, while the SQUID parameters can be designed to provide optimum response. The remote location of the SQUID prevents magnetic fields generated by the SQUID modulation and feedback signals from affecting the sample.

Two schemes are possible for separating the pickup loop and SQUID for an SSM. One arrangement maintains the pickup loop as an integral part of the SQUID washer, such that a current circulating in the SQUID washer also flows down a flux transformer and through the pickup loop on its return path [8, 9]. This configuration provides strong coupling of the input flux signal imaged by the pickup loop. Also, because of the integrated nature of the design, both the SQUID and the pickup loop are patterned on the same substrate. This can make the fabrication difficult and damage to the pickup loop during scanning makes the entire device unusable. This problem is solved in the other arrangement, in which the SQUID and pickup loop are fabricated on separate substrates. With this design, the pickup loop and flux transformer are patterned on one substrate, with a superconducting input coil at the end of the flux transformer opposite the pickup loop. The input coil is designed to fit directly over the SQUID washer, as the SQUID chip is attached with adhesive to the pickup loop, in a "flip-chip" technique [8]. Our SSM uses this second coupling approach.

In order for the pickup loop to image the sample flux distribution effectively, the flux transformer which carries the flux signal back to the SQUID must be magnetically screened. The simplest design for the flux transformer consists of two coplanar strips which join up with the pickup loop at one end and the input coil at the other end. The inductance of the slot between the strips is screened by covering the slot with a superconducting ground plane. It is important that the end of the ground plane not extend too close to the pickup loop, as the presence of the extra superconducting material of the ground plane can distort the magnetic fields in the vicinity of the pickup loop. In our design, the ground plane ends about 2μm from the edge of the pickup loop. The fabrication for this configuration is relatively straightforward, but this simple screening method allows some external flux to penetrate through the flux transformer, producing ghosting effects in the images, as shown in Figure 5.4.

Figure 5.4: SSM images showing ghosting effect from stray pickup of flux along the flux transformer due to imperfect screening.

The flux transformer can be improved by switching from a coplanar design to a strip-line with the return path directly on top of the outgoing layer of the line. This presents a much lower inductance to the sample flux, however, the fabrication is more difficult, as any short between the top and bottom layers of the strip-line renders the pickup loop useless. Further improvements are possible by using multiple ground planes, while minimizing field distortions around the pickup loop. These considerations are particularly important for developing higher resolution SSM systems with pickup loops of 1μm diameter or less [9].

5.2.2 Pickup loop fabrication

Because our current design uses the flip-chip coupling scheme, we fabricate the pickup loop structure on a separate substrate from the SQUID. We typically use microscope slide glass for the substrate, although we have also made pickup loops on quartz and sapphire substrates. The pickup loop end of the substrate is filed at a shallow angle to produce a double-bevel, as shown in Figure 5.5. During scanning, the apex of the double-bevel is in direct contact with the sample surface, while the 10μm diameter pickup loop is between 25μm and 100μm from this point.

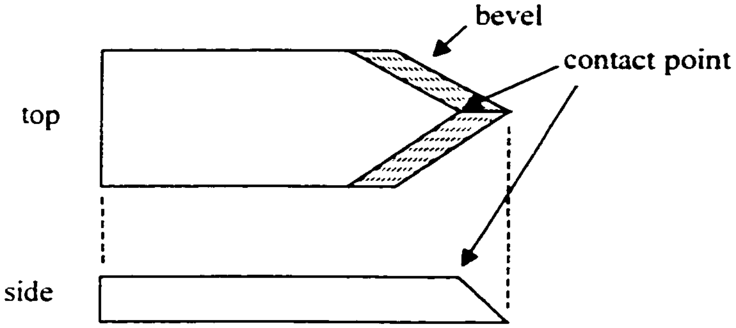

Figure 5.5: Shape of pickup loop substrate with double-bevel to define tip contact point for scanning.

We have made some of our devices by filing the bevel into the substrates before patterning the thin films. This makes the fabrication of the pickup loop more difficult, due to surface tension effects with the photoresist near the beveled edge, but this technique is preferred to the highly delicate task of filing the substrate after the device is complete. The fabrication of our pickup loop structures, shown schematically in Figure 5.6, consists of three steps:

(1) A 70nm thick Nb film is sputtered over the entire substrate. The pickup loop, input coil, and coplanar flux transformer pattern is then etched into the Nb using Reactive Ion Etching in CF_4 and O_2. This produces smoother edges to the Nb lines than a lift-off deposition process, reducing the risk of shorts to the subsequent ground plane layer.

(2) The entire device is coated with insulating SiO_2. This layer is typically about 300nm thick.

(3) A Nb film is sputtered into the pattern for the ground plane, providing a screening of the inductance of the flux transformer slot.

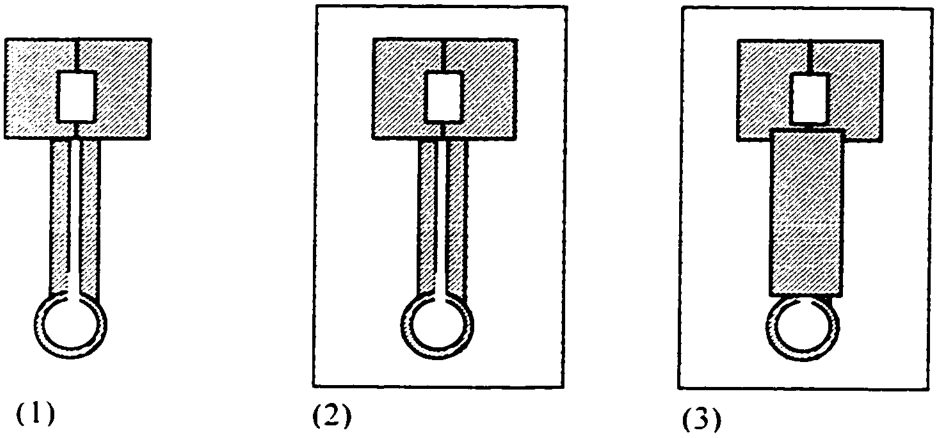

Figure 5.6: Schematic of pickup loop fabrication procedure. (1) Nb film is deposited and then lithographically patterned and etched in RIE to define the pickup loop, flux transformer, and input coil. (2) Blanket deposition of SiO_2 insulation (dotted region) to electrically isolate the flux transformer and the subsequent ground plane. (3) Deposition of Nb ground plane to cover the flux transformer slot.

(a)

(b)

Figure 5.7: (a) 10μm pickup loop from our SSM. (b) Picture of input coil, which mounts directly over SQUID washer.

A picture of a completed pickup loop structure is shown in Figure 5.7. The pickup loop diameter is 10μm, with 2μm linewidths, while the input coil has a 100μm inner width, to fit directly over the SQUID washer.

5.2.3 Flux sensitivity / noise

The flux sensitivity of the SQUIDs made in our cleanroom facility ranges from $10^{-5}\Phi_0/\mathrm{Hz}^{1/2}$ - $10^{-4}\Phi_0/\mathrm{Hz}^{1/2}$, as measured by monitoring the unfiltered SQUID output signal on a spectrum analyzer. We then approximate the noise at the pickup loop from an estimate of the amount of signal flux which is coupled back to the SQUID, based on the relative inductances of the pickup loop, flux transformer, and input coil. This yields an input noise level of $10^{-4}\Phi_0/\mathrm{Hz}^{1/2}$ - $10^{-3}\Phi_0/\mathrm{Hz}^{1/2}$. Improvements to this noise value could be made by better optimizing the SQUID parameters. Also, a more sophisticated ground plane scheme for the flux transformer would improve the coupling to the SQUID and would reduce the relative input noise at the pickup loop.

5.3 Scan mechanism

In order for the pickup loop to image the sample flux effectively, it must be kept less than one loop diameter above the surface. Otherwise, the magnetic features on the sample surface are washed out as they are coupled into the pickup loop. This requirement is most easily satisfied by scanning the pickup loop substrate at a shallow angle, with the tip of the substrate in direct contact with the sample surface. Our SSM uses this arrangement, as shown in the schematic in Figure 5.8. A hinge joining the pickup loop chip to the scan arm can flex so that the pickup loop is able to track the surface topography, maintaining a roughly constant height of the loop above the sample. Typically the pickup loop is 1μm - 5μm above the sample surface during scanning, depending on the angle of the substrate and the distance between the pickup loop and the contact point between the tip and the sample surface. While the contact force between the tip and the sample is relatively weak, the sample must still be coated with a protective insulation layer to prevent damage to the sample surface. We typically coat our samples with about 0.5μm of sputtered SiO_2 and 0.1μm of Al_2O_3.

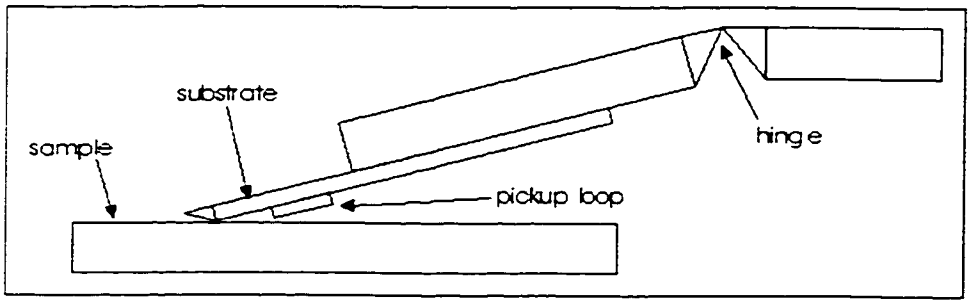

Figure 5.8: Scan assembly and hinge arrangement in the SSM (not to scale).

The scan arm, to which the SQUID and pickup loop are attached, is raster scanned over the surface at the end of a long pivot rod by stepper motors which are located about one meter away. The pivot rod provides an approximately 1/5 reduction of the stepper motor motion. Typical images cover an area several 100μm on a side, while the pickup loop can be translated over a total range of several mm in the x and y directions. During the raster scan, the step size is typically 2μm-4μm per pixel, while the scan speed is about 200μm/s, thus requiring several minutes to acquire an image. Scan speeds could be increased by switching to a piezoelectric-actuator-based scan mechanism, similar to the Scanning Hall Probe Microscope, discussed in Section 4.3.7. It may also be possible to develop a more sophisticated height regulation scheme, allowing for the pickup loop chip to hover out of contact above the sample surface, eliminating the need for protective coatings on the samples.

5.4 Cryogenic insert design

Our SSM is built on a cryogenic insert which fits in a conventional liquid helium dewar. The SQUID, pickup loop, and sample are enclosed in a vacuum can at the bottom end of the insert, and are immersed in the liquid helium bath. A small pressure of helium exchange gas is used in the vacuum can to maintain the SQUID and pickup loop well below the transition temperature of Nb (9K), while the sample, mounted on a heater block, can be temperature-regulated from the bath temperature to around 10K. By pumping on the helium bath, it is possible to lower the temperature down to 1.5 K. Because our SQUID and pickup loop are not well thermally anchored, an increase in sample temperature raises the SQUID temperature. This prevents us from imaging high-T_c superconductor samples at elevated temperatures. It is possible to add extra thermal straps and heat shielding to allow for the operation of a low-T_c-based SSM for sample temperatures up to 100 K [10].

Figure 5.9(a) contains a picture of our SSM insert, showing the stepper motors at the top, well away from the cryogens. The SQUID and pickup loop are located at the bottom of the insert, as shown in the closeup pictures of the cold end of the insert in Figure 5.9(b). The scan arm can be seen at the right side, holding the SQUID and pickup loop assembly above the sample. The sample block can be raised so that the sample contacts the pickup loop tip by turning a threaded rod from the top of the insert. This arrangement prevents damage to the tip by allowing for the sample to remain out of contact when the insert is moved. The threaded rod also makes possible the adjustment of the contact angle of the pickup loop relative to the sample, as raising the sample causes the pickup loop hinge to flex to a new position. The sample and pickup loop are situated in the middle of a Helmholtz coil, which can produce magnetic fields up to 50 Oe, although images are typically acquired in much smaller fields. The strength of the Helmholtz coil was calibrated with a commercial Hall probe.

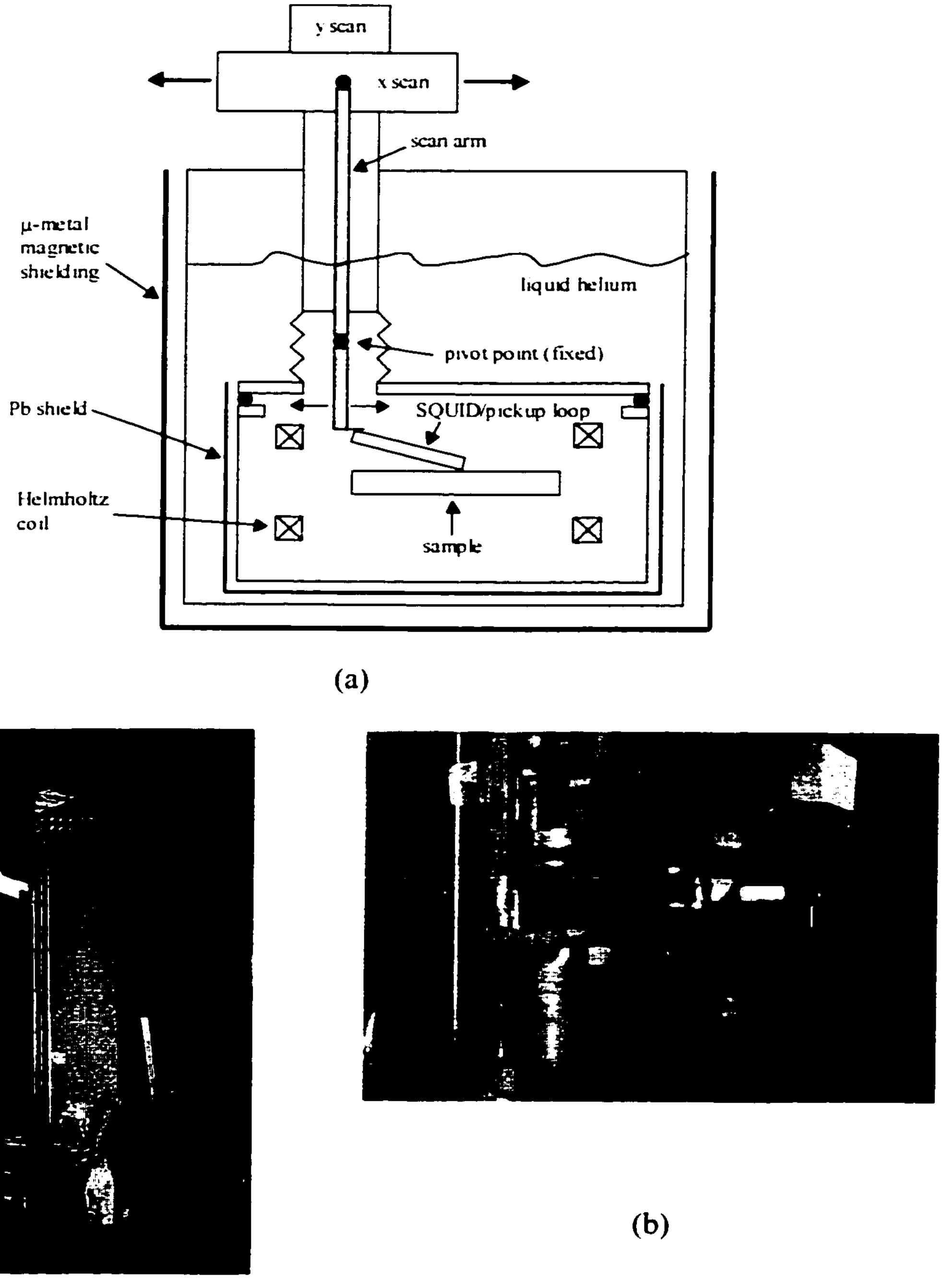

(a)

(b)

Figure 5.9: (a) Cryogenic insert design and dewar arrangement (not to scale). (b) Pictures of insert and close-up of scan assembly.

The sample and SQUID are shielded from external magnetic fields by a superconducting lead bag which encloses the vacuum can. while the dewar is surrounded by a double-walled μ-metal shield for optimum shielding. The background magnetic flux density at the location of the sample is typically less than 1mG. as determined by cooling a superconducting film with no current in the Helmholtz coil. then counting the number of vortices which are trapped in the film over a given area due to any residual field.

The separation between the pickup loop and SQUID in our SSM places the SQUID near the inner edge of the Helmholtz coil. Thus when the SQUID and pickup loop assembly is scanned over the sample with an applied magnetic field to generate an image. the SQUID is moving through a region where the Helmholtz coil field has a strong gradient. This produces a substantial gradient in images taken in an applied field. and is not related to any flux change at the sample surface. We typically remove this background from the images later. by fitting a plane to the image and subtracting it numerically.

5.5 Sample SSM images

Our SSM was originally developed to study fabricated superconducting structures such as superconducting wire networks and Josephson junction arrays in relatively small magnetic fields. We have imaged vortices in both square and triangular arrays with 20μm lattice spacing in various applied magnetic fields. Figure 5.10(a) contains an image of the checkerboard vortex distribution in a square Josephson junction array with a frustration factor of 1/2. i.e. the magnetic field threads a vortex through every other cell in the array [11]. Figure 5.10(b) shows vortices in a triangular array at 1/4-filling. We have also used the SSM to image vortices in continuous superconducting films and crystals. Individual vortices can be resolved as long as they are separated by at least one pickup loop diameter, corresponding to a magnetic flux density of about 0.2 G for our 10μm pickup loop. An image of isolated vortices in a a-MoGe thin film cooled in a field of 30 mOe is shown in Figure 5.10(c). For cooling fields above 0.2 Oe, the vortex images merge together and we can only measure the local flux density. However, with the pickup loop held at a fixed location on the sample, it is still possible to observe dynamical processes involving jumps of a single vortex [12].

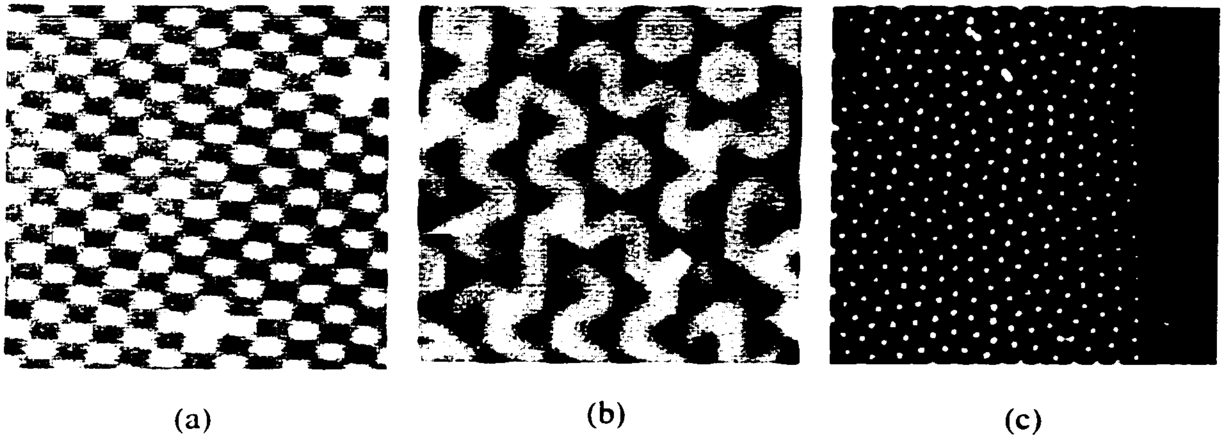
(a) (b) (c)

Figure 5.10: (a) SSM image of vortices in a square Josephson junction array, f=1/2. (b) Vortices in a triangular Josephson junction array, f=1/4. (c) Isolated vortices in a-MoGe thin film cooled in a magnetic field of 30 mOe, with the edge of the film along the right side of the image.

5.6 Interactions between the scanning tip and vortices

In weak-pinning superconductors, we have observed an interaction between the raster scanning and the vortices in the sample. This interaction causes shifts in the positions of vortices in the images, such that two repeated scans over the same area of a weak-pinning sample will yield different distributions of vortices. We did not observe these disturbances previously in images of stronger-pinning Nb films, placing a rough upper bound on the strength of the perturbing interaction.

By studying the shifts of the vortex positions, we have determined that the interaction is localized within a few μm of the contact point between the tip and the sample surface. If we scan a field-cooled distribution of vortices such that the tip passes over the vortices before they are imaged by the pickup loop, the image contains a disordered vortex pattern, with vortices pushed out to the edges of the scan area. However, the first approximately 50μm of such an image contains a well-ordered distribution of vortices. This distance corresponds to the separation of the pickup loop and the tip. Thus at the start of the scan, the pickup loop is located at the bottom of the image area, while the tip contacts the sample this 50μm distance into the scan area. If we reverse the scan direction, such that the pickup loop images a vortex before it is passed over by the tip, then we obtain well-ordered vortex images as shown in the example of Figure 5.10(c). However if we scan this region a second time, the vortex distribution will be scrambled, as the vortices were perturbed by the interaction with the tip during the first scanning. Figure 5.11(a) shows an image where we have scanned a small region of field-cooled vortices, thus perturbing the distribution. We then scanned a larger window surrounding the initial region, producing an image of ordered vortices outside of the initial scan region, and disorder within. If the scan crosses the edge of the superconductor, vortices can be completely swept out of the sample. We were able to generate several narrow stripes where vortices were removed from the superconductor, thus spelling out the letters "UI", as shown in Figure 5.11(b).

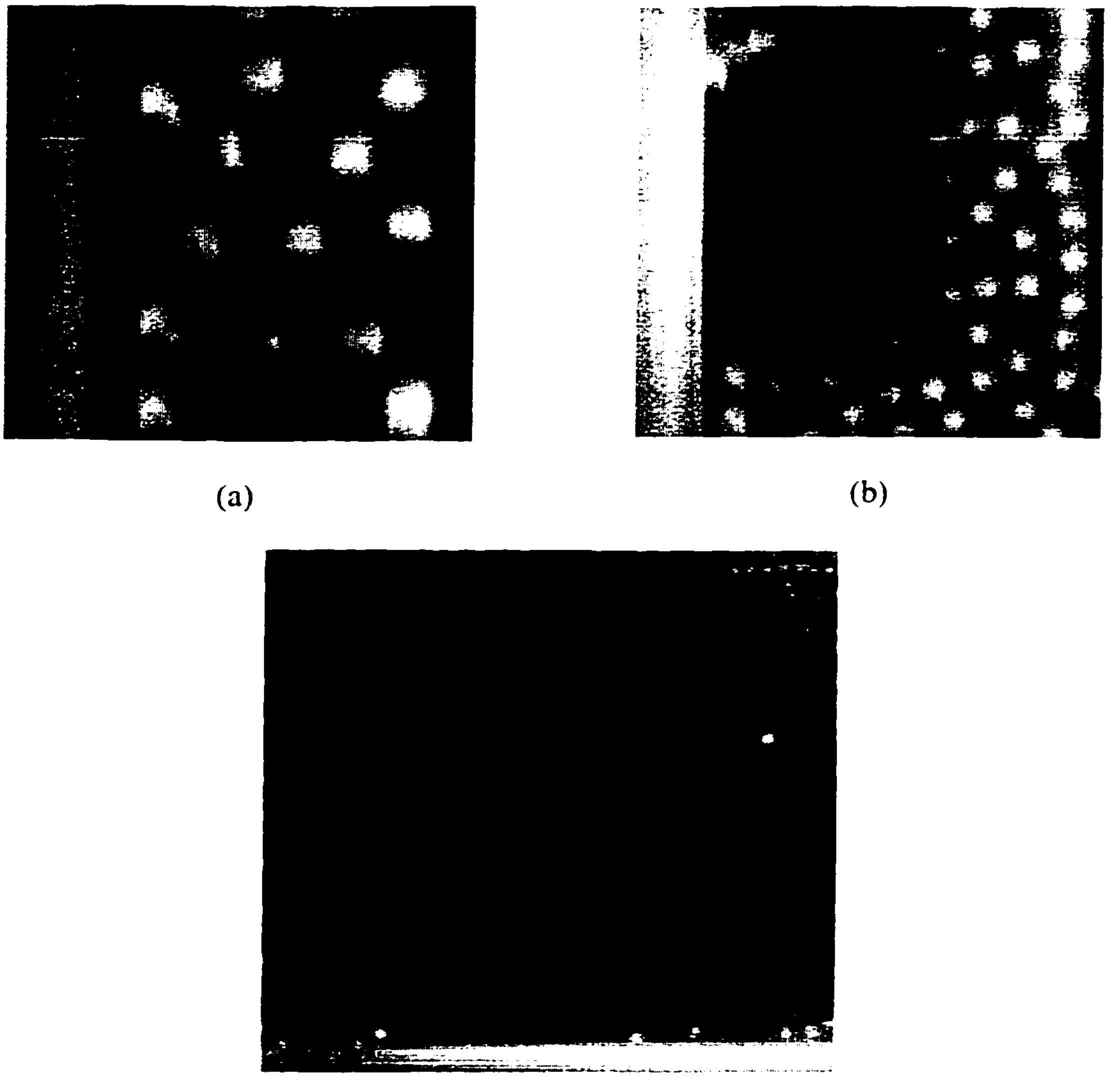

(a) (b)

(c)

Figure 5.11: Images of vortex disturbance due to the tip-sample interaction. (a) The small square region was scanned initially. (b) then the larger area surrounding the first scan area was imaged such that the pickup loop passed over the vortices before they were disturbed by the tip. (c) Regions of vortices have been swept away to spell out the letters. "UI". The edge of the MoGe film is along the bottom of the image.

Based on the above descriptions of the perturbed vortex patterns. we conclude that the interaction is localized at the tip. This can also be seen by repeatedly scanning across the same line. producing no change in the locations of the vortices underneath the pickup loop. This rules out an interaction based on superconducting screening by the pickup loop or SQUID modulation signals being transmitted down to the sample through the pickup loop. One possibility for the tip-vortex interaction mechanism could be local frictional heating at the contact point. If the heat could not be dissipated quickly enough, the superconductor could be locally heated, causing the neighboring vortices to move more easily. However, we have tried varying the speed of the raster scanning, producing no observable change in the interaction strength. Another possible interaction involves a static charge buildup on the scanning tip. Because the sample is coated with a protective insulating layer, scanning an insulating (glass) tip across the surface may cause the buildup of a static charge on the tip. This moving charge could then interact with the magnetic field of the vortex lines. However, a test run with a sample coated with a conducting titanium layer on top of the insulation also exhibited similar vortex perturbations by the scanning tip. It is also possible that the vortices could be interacting with a paramagnetic moment at the tip. We fabricated several of our pickup loops on glass from commercial glass microscope slides. Impurities in this grade of glass produce a paramagnetic moment below about 30 K. While this seems suspicious, we have recently made pickup loops on high-purity fused silica substrates, which do not exhibit any paramagnetism, and we still observe a disturbance of the vortices due to the scanning.

We are still attempting to understand the interaction mechanism between the tip and the vortices. At the present time, all images of weak-pinning superconductors are obtained with the reverse, non-destructive scan direction. This limits our imaging to one pass per temperature cycle over a particular region, as the sample must be heated above T_c and then re-cooled in order to remove the disturbance from the previous scan. In the future, we plan to make all pickup loops on non-paramagnetic substrates. We may also try to develop a piezoelectric-actuator-based scan arrangement in which the pickup loop can be scanned out of contact with the sample.

5.7 References

[1] L. N. Vu, M. S. Wistrom, and D. J. Van Harlingen, *Imaging of magnetic vortices in superconducting networks and clusters by scanning SQUID microscopy*, Appl. Phys. Lett. **63**, 1693 (1993).

[2] L. N. Vu and D. J. Van Harlingen, *Design and Implementation of a Scanning SQUID Microscope*, IEEE Trans. Appl. Supercond. **3**, 1918 (1993).

[3] M. S. Wistrom and D. J. Van Harlingen, *To be published.*

[4] C. C. Tsuei, J. R. Kirtley, C. C. Chi, *et al.*, *Pairing Symmetry and Flux Quantization in a Tricrystal Superconducting Ring of* $YBa_2Cu_3O_{7-\delta}$, Phys. Rev. Lett. **73**, 593 (1994).

[5] J. Clarke, W. M. Goubau, and M. B. Ketchen, *Tunnel Junction dc SQUID: Fabrication, Operation, and Performance*, J. Low Temp. Phys. **25**, 99 (1976).

[6] C. D. Tesche and J. Clarke, *dc SQUID: Noise and Optimization*, J. Low Temp. Phys. **29**, 301 (1977).

[7] J. Clarke, in *SQUID Sensors: Fundamentals, Fabrication and Applications*, edited by H. Weinstock (Kluwer Academic, Maratea, Itlay, 1995), Vol. 329, p. 1.

[8] J. R. Kirtley and J. John P. Wikswo, *Scanning SQUID Microscopy*, Annu. Rev. Mater. Sci. **29**, 117 (1999).

[9] M. B. Ketchen and J. R. Kirtley, *Design and Performance Aspects of Pickup Loop Structures for Miniature SQUID Magnetometry*, IEEE Trans. Appl. Supercon. **5**, 2133 (1995).

[10] J. R. Kirtley, C. C. Tsuei, K. A. Moler, *et al.*, *Variable sample temperature scanning superconducting quantum interference device microscope*, Appl. Phys. Lett. **74**, 4011 (1999).

[11] M. Tinkham. *Introduction to Superconductivity* (McGraw-Hill, Inc., New York. 1996).

[12] B. L. T. Plourde and D. J. Van Harlingen. in *Physics and Materials Science of Vortex States. Flux Pinning and Dynamics*. edited by R. Kossowsky. S. Bose. V. Pan and Z. Durusoy (Kluwer Academic. Dordrecht. 1998). Vol. 356. p. 281.

CHAPTER 6

VORTEX DISTRIBUTIONS AND DYNAMICS NEAR SURFACE FEATURES IN SUPERCONDUCTORS

The range of available magnetic imaging techniques provides many options for the study of flux states in superconductors. Although our present SSM can only spatially-resolve discrete vortices for a magnetic flux density below about 0.2 G, the superior flux resolution makes it possible to observe the motion of individual vortices through the time dependence of the SQUID signal. This allows for an investigation of the vortex dynamics near various isolated pinning structures. We have used our SSM to study the interactions between vortices and surface features in several different superconducting systems. The basic idea of the vortex line energy variation at a surface step was first presented in Section 3.3.3. In this chapter, we begin with a review of previous experimental studies of vortex interactions with surface steps. We then discuss our SSM measurements of vortex distributions and dynamics near surface features in $NbSe_2$ crystals. In Chapter 7, we present the results of our SSM imaging around steps in patterned thin-film superconducting structures.

6.1 Previous studies of vortex interactions with surface steps

6.1.1 Transport measurements

The interaction of vortices with surface features was first considered in the context of transport measurements. Morrison and Rose measured the variation in critical current density J_c for InBi foils with thickness variations produced by surface indentations [1]. Diffraction gratings of various widths were pressed into the surface of the foils, resulting in parallel grooves with a ramp-like profile, such that the grooves were deeper on one edge. The spacing ranged between 12 and 1200 grooves/mm and the groove width was varied between 0.13μm and 6.25μm. The authors measured $J_c(H_a)$ for different directions of current flow relative to the groove direction with the magnetic field always applied normal to the foil surface. Current flow perpendicular to the grooves, such that the Lorentz force was directed along the grooves, produced the same $J_c(H_a)$ curve as an identical film with no surface indentations. For currents flowing parallel to the grooves, with the Lorentz force normal to the steps, the critical current was enhanced by over a factor of two due to the vortex line energy variation. This effect vanished for the narrowest grooves, for which the width was comparable to the coherence length of the material, thus preventing effective pinning of the vortices. The authors also observed an asymmetry in the J_c enhancement with respect to the current polarity due to the ramp profile of the grooves. This appears to be one of the earliest measurements of a ratchet effect in vortex systems.

A similar system of surface channels was studied by Daldini et al. in thin granular Al films [2]. A series of narrow parallel channels spaced by a few microns was etched about 20nm deep into the surface of a roughly 500nm thick film. The authors compared $J_c(H_a)$ for the Lorentz force directed normal to the channels with $J_c(H_a)$ for an identical film with no surface etching. For temperatures just below T_c, the critical current for the channel sample was enhanced and exhibited peaks corresponding to the vortex spacing being commensurate with the channel spacing. At lower temperatures, the channel sample still had an enhanced J_c, but the commensurability peaks were not observed. This was attributed to the shorter penetration length at the lower temperatures which prevented the vortices from forming a lattice which could lock in with the channel spacing.

6.1.2 Imaging of vortex distributions

The interaction of vortices with surface steps can also be probed through direct magnetic imaging of the vortex distribution around surface features. Dai et al. used Bitter decoration to image vortices on the surface of BSCCO crystals containing a large number of surface steps [3]. The samples were cooled to 4.2 K with a magnetic field applied parallel to the c axis, normal to the imaging surface, with 10G < B < 100G. The resulting flux line lattice was significantly distorted in the vicinity of the surface steps. The authors observed a higher density of vortices along the thin side of the surface steps with few vortices near the thick side, as shown in the image in Figure 6.1.

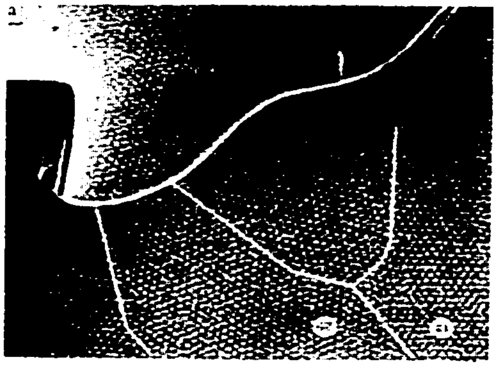

Figure 6.1: Bitter decoration image of vortex lattice around a surface step on a BSCCO crystal cooled in a magnetic flux density of 27 G. The step is the curved region running across the upper portion of the image, with the high side toward the top of the image. Lines indicate grain boundaries in the vortex lattice which originate on the surface step (from Dai et al., 1994, p.749).

Sufficiently large surface steps also disturbed the vortex lattice at large distances from the step, through the formation of grain boundaries which were observed to propagate through the lattice away from the step. The energy scale for grain boundary formation was approximated, based on the elastic moduli of the vortex lattice. This was then compared with the estimated line tension barrier pinning energy of the step, yielding an estimate for the smallest surface step which could produce grain boundaries of 1000Å. After characterizing the surface step heights with an Atomic Force Microscope (AFM), the authors then noted that smaller surface steps did not generate grain boundaries in the vortex lattice, although the vortex distribution was still perturbed locally around the smaller steps.

Vinnikov et al. also imaged vortex distributions near surface steps in BSCCO crystals [4]. Similar to Dai et al., upon field cooling the crystals, the vortices were observed to form higher density rows along the thin side of surface steps with a much lower vortex density on the thick side. This effect vanished when the crystal was irradiated with heavy ions, indicating that the damage-induced pinning was stronger than the vortex interaction with the steps. The step heights were characterized by AFM and ranged between 50nm and 1μm. The width of the vortex-free region was measured from the Bitter decoration images for steps of various heights at two different cooling fields, 1.1mT and 10mT. In general, this width was on the order of a few spacings of the uniform vortex lattice well away from the step. An increase in the width of the vortex-free region with step height was observed, although the error bars are large and there is substantial scatter to the data, allowing one to also draw a flat line, independent of step height through most of the data points. The authors also claim that this width is independent of the magnetic field, although this seems to contradict the data, which show a decrease in the width of the vortex-free regions for cooling in larger magnetic fields. The occurrence of the vortex-free regions is attributed to a geometrical barrier type effect, similar to Section 3.3.2, due to enhanced screening currents flowing along the step which exceed J_c locally, and push vortices away from the thick side of the step.

Harada et al. observed perturbations of the vortex distribution near thickness variations in thin Nb films using Lorentz microscopy [5]. Surface steps less than 0.1μm, as measured by AFM, produced a higher density of vortices in a row along the low side of the step with correspondingly few vortices on the thick side for a magnetic flux density of 20 G. The steps also influenced the vortex dynamics as the vortices tended to move in channels along the surface steps once the magnetic field was removed.

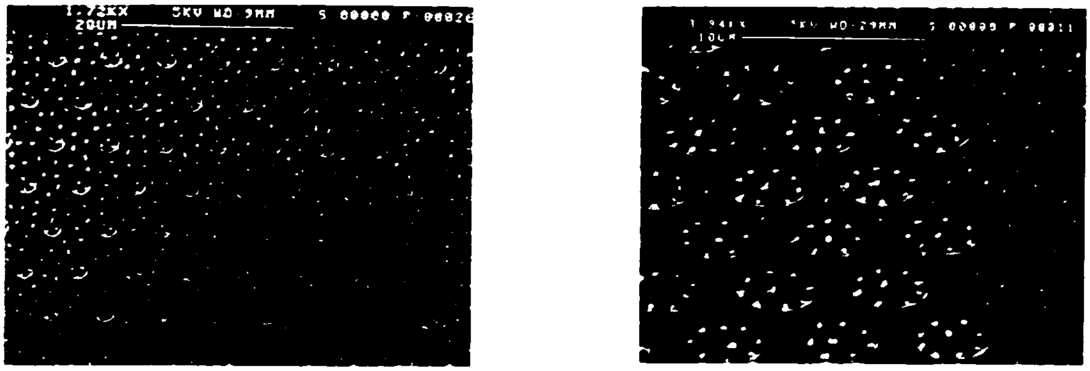

Figure 6.2: Field-cooled images of vortices in circular depressions in the surface of a Nb film obtained with Bitter decoration. The Nb film thickness away from the circles is 170nm, while the thickness in the depressions is 65nm (105nm step height). The radius of the circular regions is 1μm in the left image and 2.2μm in the right image. The sample was cooled in a magnetic field of 6.37 Oe in both images and the sample is tilted in the right image (from Bezryadin et al., 1996, p.8559).

Bezryadin et al. used Bitter decoration to image vortex distributions near circular depressions in the surface of a 170nm thick Nb film [6]. The circular depressions were patterned with electron-beam lithography and reactive ion etching, and ranged in size from 0.15μm to 2.2μm in radius, with depths between 20nm and 170nm, the last value corresponding to a complete hole through the film. Upon cooling the sample to 4.2 K in a perpendicular magnetic field of 6.37 Oe, the authors observed a much higher density of vortices in the circular depressions than in the rest of the film. This increase in vortex density occurred for even the shallowest steps and the magnitude of the effect did not vary significantly with the depth of the depressions. Figure 6.2 contains images of vortices in some of these patterned regions. The authors attributed the observed vortex distributions to the presence of a surface superconducting state along the face of the depression perimeters. This surface state could compress flux into the circular regions as the sample was cooled through T_c in a magnetic field [6]. The possibility of surface superconductivity influencing field-cooled vortex distributions near surface steps will be discussed further in Chapter 7, as we present our SSM imaging around patterned thin-film structures.

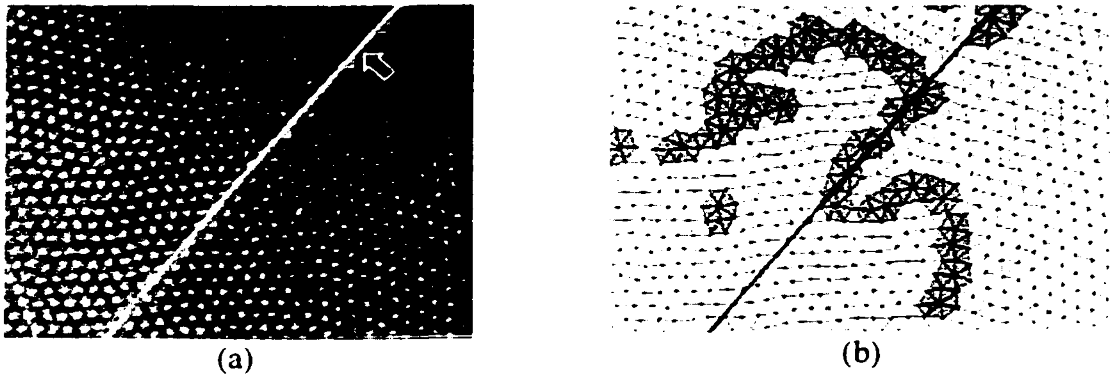
(a) (b)

Figure 6.3: (a) Bitter decoration of image near a 0.35μm surface step on a $NbSe_2$ crystal cooled to 4.2 K in a field of 36 Oe with the field constant during imaging. The step runs diagonally across the image as indicated by the arrow. (b) Delaunay triangulation of the Bitter decoration image. Shaded regions indicate defects in the triangular lattice which do not appear to be correlated with the surface step (from Pardo et al., 1997, p.1370).

Field-cooled vortex distributions and flux creep near surface steps in $NbSe_2$ crystals were studied by Pardo et al. using Bitter decoration [7]. Steps with heights between 30nm and 350nm were produced by cleaving the sample, resulting in different amounts of the crystal peeling away in different locations. Images of the field-cooled vortex pattern did not show any disturbance related to the presence of a 350nm surface step, in contrast to the other imaging experiments discussed previously. This was determined through Delaunay triangulation of the decoration images which showed no correlation between defects in the flux line lattice and the surface step, as shown in Figure 6.3. The authors attribute the lack of influence of the step on the field-cooled patterns to the vortex distribution quenching much closer to T_c in $NbSe_2$ as compared to BSCCO. The weaker intervortex interactions close to T_c prevent the vortices from conforming to the surface step. In contrast to the static field-cooled images, Pardo et al. did observe a significant vortex interaction with the steps once the cooling magnetic field was removed. The crystals were cooled to 4.2 K in a field of 36 Oe, then the field was reduced to zero, and the resulting vortex distribution was imaged 10 minutes later. The resulting flux density gradient tended to push vortices out of the crystal, as in the standard flux creep process. However, vortices were observed to pile up at surface steps which would require the vortex to increase in length on the way out of the sample. A surface step with a thickness decrease did not influence the vortex distribution. From the images, the authors were able to calculate the increase in vortex interaction energy per unit vortex length, ΔE_i, due to the higher density of vortices along the low side of the steps. This energy was observed to increase linearly with the surface step height, as determined by performing this same analysis around several different steps with a range of heights, h. However, a comparison of the interaction energy increase with the surface step energy:

$$h\varepsilon_L = t\Delta E_i, \qquad (6.1)$$

yielded a sample thickness, t, which was considerably less than the measured crystal thickness. The authors attributed the effective thickness to a deformation length for the vortices. Thus the vortices just below the surface bend to accommodate the enhanced pinning of the step, while deeper in the bulk thickness, the vortex distribution would be more uniform. Such a distribution is predicted to produce periodic bursts of flux, as vortices may snap across the step once the interaction energy builds to some critical value. However, these bursts could not be observed with Bitter decoration, as only one image is produced during a cooldown.

6.2 SSM imaging of vortex distributions in NbSe$_2$

We have used our SSM to image both static and dynamic flux structures in NbSe$_2$ crystals cooled in magnetic fields up to 14 Oe. Static images of the vortex distribution in small magnetic fields show a substantial distortion by steps on the crystal surface. Vortex motion is induced by removing the cooling field abruptly, causing vortices to leave the sample. Using the excellent flux sensitivity of the SSM, we can image the changing flux patterns around the steps and we are also able to monitor the local temporal dynamics of the flux exit [8].

6.2.1 Sample properties and preparation

We used high-quality NbSe$_2$ crystals with $T_c = 7.1$ K for our measurements. The anisotropic, layered nature of NbSe$_2$ allows surface steps to develop easily as the crystals are cleaved. We did not directly measure the penetration length in our samples, and there is a wide variation of values quoted in the literature. The original complete study of the superconducting properties of NbSe$_2$ by Gygax et al. [9] indicates an in-plane penetration length (for fields perpendicular to the layers, as in our experiment) of 69nm with κ=30. Due to the large anisotropy, the c-axis penetration length (fields parallel to the planes) is 230nm with κ=9 [9]. However, other values for the in-plane penetration depth quoted in the literature range up to about 250nm. The source of this variation is unclear, although it may be due to a strong sensitivity to impurities. If we take the Gygax values for the in-plane λ and κ, using equation 2.10, we obtain a line tension of 2.0×10^{-5} erg/cm, or 1.4×10^{4} K/nm. The larger values of λ reduce ε_L by up to an order of magnitude. The crystal studied for most of the data presented here had the following dimensions: 3.8 x 2.8 x 0.13 mm^3.

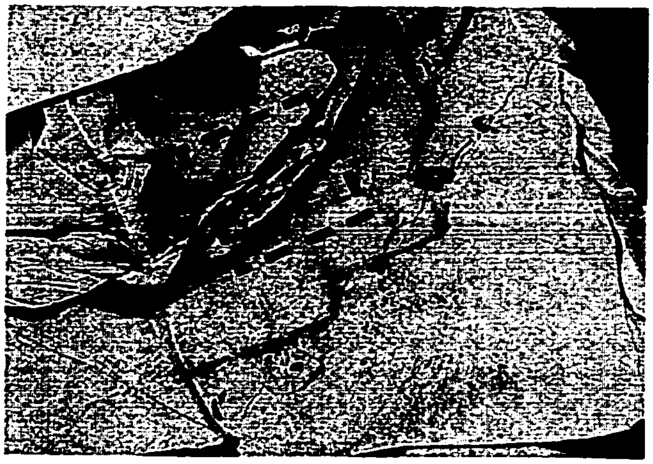

Figure 6.4: Optical microscope image of $NbSe_2$ crystal used in the experiment. The boxed region (0.5mm x 0.5mm) indicates where most of the SSM images and SQUID time traces presented here were taken.

Before cooling down in the SSM, the crystal was cleaved using tape, producing several prominent surface steps where different numbers of crystal layers peeled away. The surface topography across these steps was measured with a profilometer, then the sample was attached to a Si substrate and was coated with a protective layer of sputtered SiO_2 and AlO_x. Figure 6.4 contains an optical microscope image of the crystal used in these measurements. The crystal exhibited many intricate surface features, including a thicker region surrounding the hexagonal spiral growth structure near the corner. Many of the SSM images and SQUID time traces were obtained in the boxed region, somewhat away from the center of the crystal. A commercial SQUID magnetometer was used to measure the time dependence of the magnetization of the crystal under the same conditions as the SSM measurements. i.e. the sample was cooled in magnetic fields up to 13.8 Oe. then the field was removed. The magnetization was observed to decay logarithmically in time. as expected from standard flux creep theory [10]. as discussed in Section 3.2.5.

6.2.2 SSM images of field-cooled flux patterns

The superconducting Helmholtz coil in the SSM was used to apply magnetic fields up to 13.8 Oe with the temperature around 20 K. well above T_c. The temperature was then lowered to 4.2 K, in equilibrium with the surrounding helium bath. SSM images in small cooling fields with the field still on during scanning indicate a higher density of flux at the low side of the surface steps. Figure 6.5 contains an image in a small applied field around surface features on a different $NbSe_2$ sample. showing a higher density of flux along the low side of steps and fewer vortices around the thick rim of the steps.

Figure 6.5: SSM image (508μm x 508μm) near surface pit (roughly 2μm deep, upper-right) and step (about 0.7μm. lower-left) on a different $NbSe_2$ crystal from that shown in other figures. The sample was cooled in $H_a \approx 0.2$ Oe, and the field was kept on during imaging.

This influence of the surface steps on the vortex distribution in field-cooled images is quite different from that observed by Pardo et al. [7], also in $NbSe_2$. This discrepancy could be due to the larger size of the surface steps on our $NbSe_2$ crystals, ranging between 0.5μm and 4μm. The steps in the experiment of Pardo et al., were no larger than 0.35μm. It is also possible that extra pinning defects were generated near the steps during the cleaving of the surface layers in our crystals. We have recently obtained a new batch of high-quality $NbSe_2$ crystals and we plan more studies of the field-cooled flux patterns around a wider range of surface steps.

Imaging field-cooled flux distributions with the magnetic field held constant is difficult for larger fields with our present SSM system. Because of the placement of the SQUID near the inner edge of the Helmholtz coil, where the field varies rapidly with position, significant gradients are produced in the images as the SQUID is scanned in an applied magnetic field. This problem could be solved by modifying the SSM so that the SQUID is fixed in place and the sample is scanned beneath it, always remaining in the center of the Helmholtz coil, where the magnetic field is uniform.

6.2.3 Images of vortex dynamics due to field changes

Upon cooling the sample and removing the field, intricate patterns of flux develop around various surface features as the vortices redistribute themselves. Figure 6.6(a) shows a SSM scan across a surface step approximately 4μm high taken about 30 minutes after the 13.8 Oe cooling field was removed. The vortex spacing at this high flux density is much smaller than we are able to resolve with the 10μm SSM pickup loop, thus these images show the spatial variation of the local flux density averaged over the pickup loop area. We find a substantial buildup of flux at the low side of the surface step as well as a depletion of flux at the high side of the step. The line trace across the step in Figure 6.6(b) shows the rapid variation of the SQUID signal in the vicinity of the step. Using the pickup loop diameter, the estimated loop height above the sample surface, and the SQUID transfer function, it is possible to convert the SQUID voltage signal into a rough estimate of the change in the number of flux quanta, Φ_0, coupled into the pickup loop. With this approximation, the light region at the low side of the step corresponds to a local magnetic flux density which is approximately 30 G larger than that on the high side. This vortex distribution is significantly perturbed within about 30μm on either side of the step.

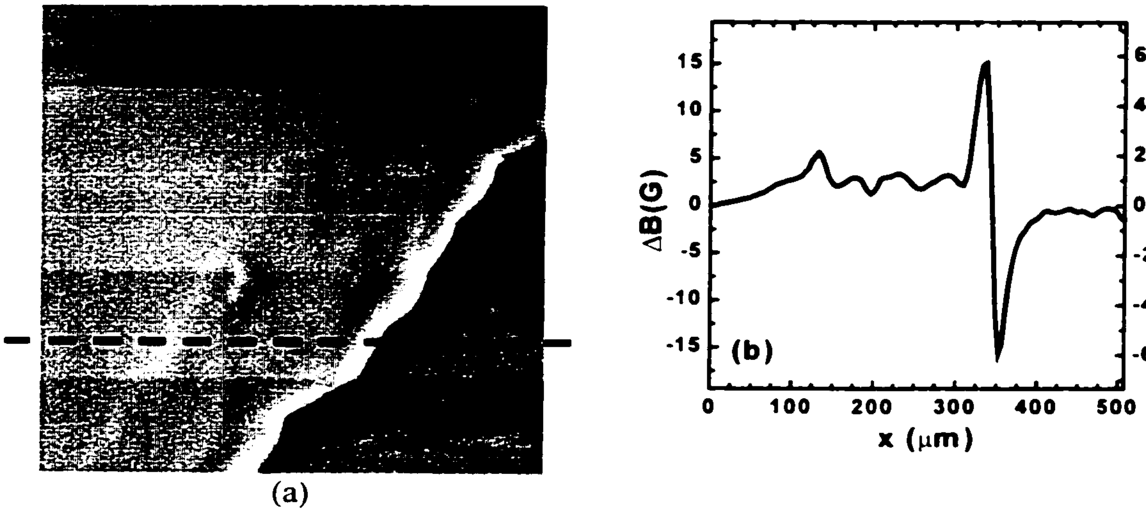

Figure 6.6: (a) SSM image (508μm x 508μm) of flux distribution around surface step in $NbSe_2$ after removing 13.8 Oe cooling field. The low side of the step is at the left. (b) Line trace of SQUID signal across step along indicated line. ΔB(G) and $\Delta\Phi/\Phi_0$ are rough estimates computed from the measured change in SQUID voltage.

The estimates of the local flux density are rather approximate due to the large step height, which is on the order of the pickup loop height above the sample surface. During the imaging, the pickup loop was oriented such that a line joining the scanning tip with the pickup loop was roughly parallel to the step. Thus the tip should have crossed the step at approximately the same time as the pickup loop, keeping the pickup loop height fairly constant over much of the scan. However, if the pickup loop were to cross from the thin to the thick side of the step before the tip, this would put the loop temporarily much closer to the surface, resulting in an artificially larger flux signal. Such errors could be avoided by studying samples where the step height is small relative to the pickup loop height above the surface.

We observe similar perturbations of the vortex distribution at virtually every visible surface feature on several different $NbSe_2$ crystals. For example, Figure 6.7 shows the modulation of the flux density after removing the cooling field in the vicinity of a roughly 2μm deep surface pit on a similar $NbSe_2$ crystal, for the same region which was imaged with a small applied field in Figure 6.5. We have also observed structure in the vortex distribution at locations in the crystal at which the surface appears to be quite flat, possibly indicating the existence of sub-surface defects in the crystal.

Figure 6.7: An SSM image (508μm x 508μm) of vortex redistribution around the surface pit of the same crystal shown in Figure 6.5. The sample was cooled in $H_a \approx 0.8$ Oe, and the field was removed about 15 minutes before imaging, causing vortices to flow and take advantage of the enhanced pinning at the surface steps. Lighter contrast corresponds to a higher flux density, as in all other SSM images shown.

6.3 SSM measurements of local flux dynamics

Once the cooling field is removed. the vortices take several minutes to rearrange around the surface steps. but then the flux distribution remains essentially unchanged. as determined by subsequent scans taken several hours later. We can use the SSM to monitor the formation of the flux pattern and to observe subsequent vortex dynamics by placing the pickup loop at particular locations on the sample surface and recording the time evolution of the SQUID signal. Near surface steps. we observe dramatic flux changes immediately after the cooling field is removed. This can then be converted into an estimate of the change in flux density. ΔB in the same region. using the procedure described earlier. With the pickup loop near the low side of the 4μm step as indicated in Figure 6.8(a). the flux density is observed to increase substantially over several minutes as shown in the time trace of Figure 6.8(b).

The increase of flux in Figure 6.8(b) approximately follows an exponential decay. as indicated in the inset. with smaller flux jumps on top of the exponential background. Following this initial rush of vortices into the region adjacent to the low side of the step. the signal flattens off. and exhibits only small fluctuations about this limiting value. This buildup of flux at the low side of the step is in sharp contrast to the overall decay of the global sample magnetization under the same conditions. as measured in a commercial SQUID magnetometer. Abulafia et al. measured the local flux relaxation in YBCO crystals using a Hall probe array [11]. The authors did observe a logarithmic temporal dependence of the local magnetic flux density at all locations across the width of the crystal. which presumably had no significant surface steps.

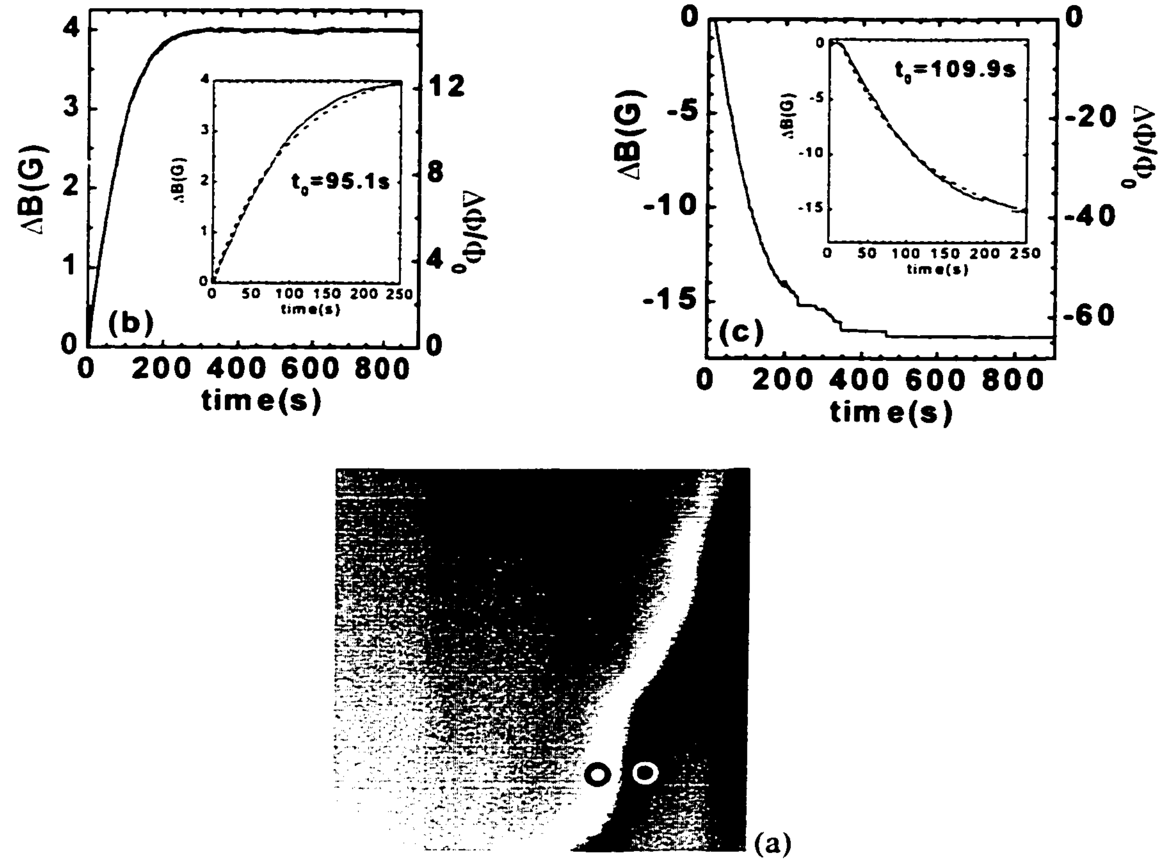

Figure 6.8: (a) Close-up SSM image (252μm x 252μm) of region around step from Figure 6.6(a) where time traces were taken. Time dependence of SQUID signal after removing 13.8 Oe cooling field near (b) low side of step (black circle) (c) high side of step (white circle). Circles indicate approximate size and location of SSM pickup loop during the corresponding time trace. Dashed curves in insets indicate exponential fits to flux buildup and decay.

At the high side of the step on our $NbSe_2$ crystal, the magnetic flux density, shown in Figure 6.8(c), decreases over roughly the same time scale as the corresponding buildup at the low side. The exponential decay of the local flux density on the thick side of the step occurs much more rapidly than the logarithmic decay of the global magnetization for the entire sample, as described by standard flux creep theory. This may be due to the magnetic repulsion of vortices from the high flux density region at the low side of the step, which causes the current density on the thick side to exceed J_c, forcing the vortices on the thick side of the step to depin. The rapid exponential increase in vortex density along the low side of the step may be related to the vortex line energy increase due to the thickness change at the step, as discussed by Pardo et al. [7]. The lower line energy on the low side may allow vortices to move in to take advantage of the enhanced pinning there. This line energy effect may even be enhanced by the cleaving process which created the step. When the upper crystal layers were removed, it is possible that the layers which remained on the low side of the subsequent step may have been partially peeled as well, thus increasing the layer separation in this region and further lowering the line energy of the vortices. Although the time dependence for these flux changes should be correct, the scale of the local flux density is approximate due to the uncertainty in the pickup loop height above the surface in the vicinity of the step as discussed in Section 6.2.3.

Following the large initial flux changes, the vortex density fluctuates with discrete bursts of a few flux quanta in the pickup loop. These jumps may correspond to several vortices which hop in and out of individual pinning sites near the location of the pickup loop. Figure 6.9 shows the long time portion of the time trace near the low side of the step from Figure 6.8(b) on an expanded scale. The SQUID signal exhibits periodic jumps of roughly the same magnitude, corresponding to a fractional change in the number of flux quanta directly underneath the pickup loop. This could be caused by a nearby region of the step where vortices can periodically hop across to the high side, only to have their original position filled by a new vortex. Because the pickup loop is several microns above the sample surface, only a portion of the flux from the hopping vortex is coupled into the pickup loop. This flux coupling is further reduced if the vortex in not directly underneath the pickup loop. Another example of these single vortex resolved jumps is shown in the time trace of Figure 6.9(b), taken on the flat region of the surface about 70μm away from the low side of the step, with the same magnetic field and cooling procedure as the other time traces. The periodic pulses of flux might be due to the motion of vortices in and out of a nearby isolated sub-surface pinning center as they traverse the region. More studies are planned to further investigate this hopping between discrete pinning sites, including temperature dependence measurements.

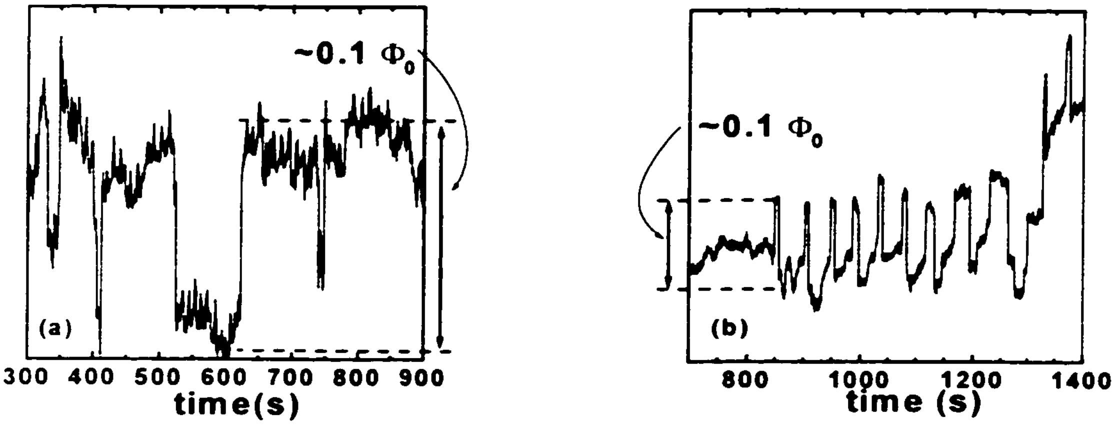

Figure 6.9: Time trace of SQUID signal after large initial changes of flux upon removing the cooling field. Bars indicate the approximate change in the number of flux quanta directly beneath the pickup loop. (a) Discrete vortex jumps at longer times near low side of step from Figure 6.8(b). (b) Vortex jumps through possible pinning site roughly 70μm away from low side of step.

Because of the complex nature of the steps in these $NbSe_2$ crystals, it has been difficult to correlate the flux behavior with the exact structure of individual steps. In the next chapter, we report on our SSM imaging around patterned steps of various heights in homogeneous thin superconducting films, including Nb and weak-pinning a-MoGe. By patterning the surface features in the films, we are able to etch the surface steps controllably, keeping the step heights much smaller than the pickup loop height above the surface. We then discuss the effects of variations in the step height on the vortex distributions around the steps for different magnetic field strengths.

6.4 References

[1] D. D. Morrison and R. M. Rose, *Controlled Pinning in Superconducting Foils by Surface Microgrooves*, Phys. Rev. Lett. **25**, 356 (1970).

[2] O. Daldini, P. Martinoli, J. L. Olsen, *et al.*, *Vortex-line Pinning by Thickness Modulation of Superconducting Films*, Phys. Rev. Lett. **32**, 218 (1974).

[3] H. Dai, J. Liu, and C. M. Lieber, *Surface Pinning and Grain Boundary Formation in Magnetic Flux-Line Lattices of* $Bi_2Sr_2CaCu_2O_{8+\delta}$ *High-*T_c *Superconductors*, Phys. Rev. Lett. **72**, 748 (1994).

[4] L. Y. Vinnikov, T. L. Barkov, B. Irmer, *et al.*, *Vortex arrays in the BSCCO (2212) single crystals in the vicinity of steps on the sample surface*, Physica C **308**, 99 (1998).

[5] K. Harada, H. Kasai, T. Matsuda, *et al.*, *Real-Time Observation of the Interaction between Flux Lines and Defects in a Superconductor by Lorentz Microscopy*, Jpn. J. Appl. Phys. **33** (1994).

[6] A. Bezryadin, Y. N. Ovchinnikov, and B. Pannetier, *Nucleation of vortices inside open and blind microholes*, Phys. Rev. B **53**, 8553 (1996).

[7] F. Pardo, F. de la Cruz, P. L. Gammel, *et al.*, *Real Space Images of the Vortex Lattice Structure in a Type II Superconductor during Creep over a Barrier*, Phys. Rev. Lett. **79**, 1369 (1997).

[8] B. L. T. Plourde and D. J. Van Harlingen, in *Physics and Materials Science of Vortex States, Flux Pinning and Dynamics*, edited by R. Kossowsky, S. Bose, V. Pan and Z. Durusoy (Kluwer Academic, Dordrecht, 1998), Vol. 356, p. 281.

[9] P. de Trey, S. Gygax, and J.-P. Jan, *Anisotropy of the Ginzburg-Landau Parameter* κ *in* $NbSe_2$, J. Low Temp. Phys. **11**, 421 (1973).

[10] Y. Yeshurun, A. P. Malozemoff, and A. Shaulov, *Magnetic relaxation in high-temperature superconductors*, Rev. Mod. Phys. **68**, 911 (1996).

[11] Y. Abulafia, A. Shaulov, Y. Wolfus, *et al.*, *Local Magnetic Relaxation in High-Temperature Superconductors*, Phys. Rev. Lett. **75**, 2404 (1995).

CHAPTER 7

SSM IMAGING OF VORTEX DISTRIBUTIONS IN PATTERNED THIN-FILM SUPERCONDUCTORS

In order to explore the interactions between vortices and surface steps and sample edges further, we have used the SSM to image patterned structures of thin-film superconductors. The superconducting films are first etched into a simple geometry, such as a large square or rectangular strip. The strip layout allows for the application of a transport current which exerts a Lorentz force on the vortices in the strip. Once the basic pattern is defined, it is possible to fabricate isolated surface steps of controlled height. In addition to surface steps and sample edges, the vortex distribution can also be influenced by the presence of bulk pinning in the film. For this reason, we have studied films with different pinning strengths.

7.1 Experimental techniques

7.1.1 Superconductor film parameters

Some of the weakest pinning superconducting thin-films are transition-metal glasses, including amorphous NbGe, NbSi, MoSi, and MoGe. The nature of the vortex pinning in these amorphous films was studied by Kes and Tsuei [1]. The dominant pinning mechanism was determined to be dislocation loops in the film structure. To pin vortices effectively, the loops must be on the order of the coherence length in size ($\xi(0) \sim$ 4 - 10nm). Because most of the dislocation loops in these films are smaller than ξ, the films have weak pinning. Critical current densities, J_c, can be as low as 10 A/cm^2.

For our vortex imaging experiments, we have patterned samples from a-MoGe films (the 'a' indicates "amorphous"). These films were sputter-deposited from a composite target with 77% molybdenum and 23% germanium. The silicon substrates were cooled during the deposition in order to quench the films in the amorphous state. The films studied have a nominal thickness of either 100 or 200nm, and the characteristic parameters for most of the films are:

$$T_c = 6.5\ \text{K}$$

$$\rho_n = 180\ \mu\Omega\text{-cm}$$

$$S = dB_{c2}/dT|_{T_c} = 2.8\ \text{T/K}.$$

The normal state resistivity, ρ_n, exhibits a very slow temperature dependence, following $\rho_n^{-1}d\rho_n/dT \approx -10^{-4}\ \text{K}^{-1}$ [2]. Because of the disorder in these films, the electronic mean free path is quite short, such that the films are in the dirty-limit. Using the dirty-limit expressions presented in Section 2.2.5, it is possible to calculate the following superconducting parameters:

$$\lambda(0) = 550\text{nm}$$

$$\xi(0) = 4.2\text{nm}$$

$$\kappa = 80$$

$$B_{c2}(0) = 13\ \text{T},$$

where the zero in the parentheses denotes the zero temperature value. The penetration depth at 4.2 K is in the range of 650 - 700nm and will be discussed in detail in the next chapter. The critical current density, J_c, in these a-MoGe films is less than 10^4 A/cm^2 at low magnetic fields [3].

Thin sputtered films of niobium provide much stronger vortex pinning. Because the films grow in a fairly well-ordered state, extended defects such as vacancies and grain boundaries can provide substantial pinning. The Nb films used in these imaging experiments were deposited onto Si substrates by dc sputtering at rates of ~ 1.5 - 2.0 nm/s. This relatively high rate resulted in critical temperatures, T_c, between 8.5 and 9 K, close to the bulk value. The penetration depth was measured with a two-coil screening technique, yielding the value: $\lambda(4.2\text{ K}) \approx 110\text{nm}$, and the temperature dependence of λ fit reasonably well to the two-fluid approximation, $(1-t^4)^{-1/2}$ [4]. The critical current density was estimated to be on the order of 10^6 A/cm^2 from critical current measurements of strips patterned from the same Nb films.

7.1.2 Pattern definition

SSM imaging was performed primarily on two different patterns. A series of large squares allowed for imaging of vortex distributions around surface steps and near sample edges. The basic square pattern, consisting of a square which was 2mm on a side is shown in Figure 7.1. Each sample contained four copies of this square pattern, spaced by several 100μm. After defining the squares, a series of 100μm wide octagonal bands was patterned onto the surface of each square. These bands were etched to various depths, creating trenches in the surface of the film. The use of four different squares made it possible to study up to four different trench depths for each sample.

In order to apply a tunable Lorentz force to the vortex distributions, we have also imaged patterns of 150μm wide strips with current injection leads. This pattern is shown in Figure 7.2. The current leads are brought well away from the scanning region, such that wires can be attached, making it possible to pass a transport current through the strip and drive the vortices along the strip width. Some of these strips have been fabricated with a surface step running along the center-line of the strip, as indicated in the figure.

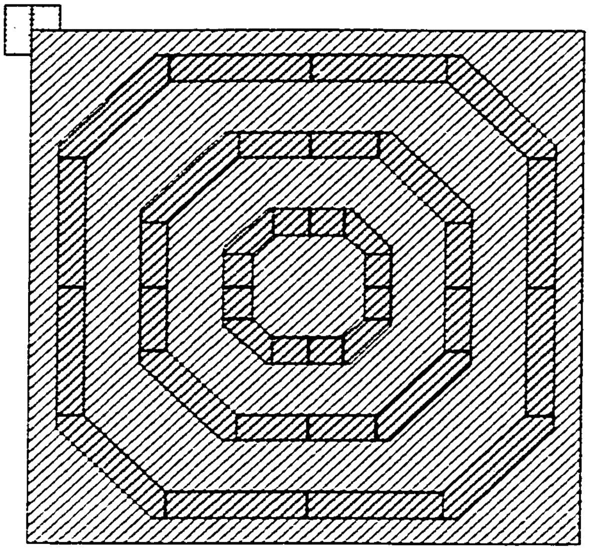

Figure 7.1: Layout of 2mm wide square pattern. The three 100μm wide octagonal trenches were etched into the surface after the square was defined. Up to four different squares with different trench depths could be located on one sample.

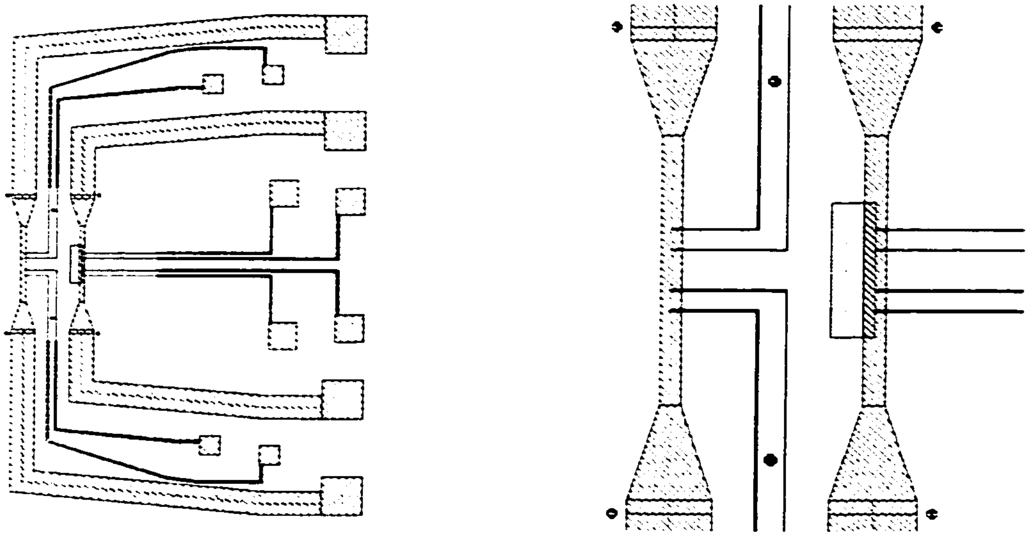

(a) (b)

Figure 7.2: (a) Strip pattern used for SSM imaging. The strips were 150μm wide and the current and voltage leads were brought well away from the scan region, such that the wiring did not interfere with the scanning process (dot spacing = 1mm). (b) Close-up of the strip region. The rectangle on the right strip shows the region which is partially etched to generate the surface step along the center of the strip (dot spacing = 100μm).

The transfer of the patterns into the films was accomplished with standard photolithographic techniques. AZ 1518 photoresist with striation-free dye was spun onto the films. The resist was exposed with a Karl Suss contact aligner and was then developed in a solution of AZ 351, diluted with de-ionized water, 1:5. The large square and strip patterns were transferred onto the continuous film (a-MoGe or Nb) using a light-field lithographic mask. The subsequent surface step windows were patterned onto the structures with etch windows in a dark-field mask. The photoresist pattern provided a mask for the etching of the films. For the niobium films, etching was accomplished with a Reactive Ion Etching system in CF_4 and O_2. The much softer a-MoGe films are easily etched with Ar ion milling. Upon completion of the patterning, the surface step heights were measured with a Dektak profilometer. After the step measurement, the samples were coated with a protective insulation layer, as described in Chapter 5.

7.2 SSM field-cooled images around surface steps and sample edges

Completed samples were loaded into the SSM for imaging. Unless otherwise noted, the images presented in this chapter are of field-cooled vortex distributions, obtained with the cooling magnetic field held constant during the imaging. The distributions were generated by first heating the sample well above T_c using a non-inductively wound manganin wire heater on the sample stage. At this elevated temperature, the magnetic field was set by driving a current through the Helmholtz coil with a home-built dc current supply. The current level was later converted to a magnetic field strength using the Helmholtz coil calibration value. Upon setting the field, the sample was cooled quickly through T_c. All of the images presented in this chapter were obtained with the sample at 4.2 K, unless otherwise noted. Samples of the square and strip patterns were imaged for applied magnetic fields below about 0.1 Oe. This ensured that the average vortex spacing was greater than about 15μm, larger than the SSM pickup loop diameter and height above the sample surface.

7.2.1 Strong-pinning Nb films

Figure 7.3 contains images of a 150μm wide, 110nm thick Nb strip. The images in the left column, (a)-(d), were obtained on a region of the strip beyond the 55nm surface step. Thus the thickness is constant across the strip width over the left ~75% of these four images, with the surface step starting at the upper right. For each image, the sample was heated above T_c and the magnetic field was adjusted before the field cooling. In this region with no surface step, at the lowest magnetic fields, the vortices generally quench in the middle of the strip and are roughly evenly spaced. This behavior is caused by the Meissner screening current distribution which is peaked at the strip edges, such that the corresponding Lorentz force is directed toward the strip center. This favors vortex nucleation away from the strip edges. For cooling in stronger magnetic fields, the vortices occupy more of the strip width, remaining approximately evenly spaced, although the distribution is significantly disordered. Because of the strong pinning in these Nb films, for the large intervortex spacing in these images, each vortex can minimize its energy by finding a nearby pinning site, resulting in the disordered vortex patterns in these regions of uniform strip thickness.

The field-cooled vortex distributions are significantly altered in the vicinity of the patterned surface steps, as shown in the right column of Figure 7.3(e)-(h). In this region of the same Nb strip, a 55nm surface step runs along the center of the strip, with the thin side of the strip towards the top of the image. For the smallest cooling fields, the vortices order into a single row along the low side of the step. As the strip is cooled in larger magnetic fields, the density of vortices pinned along the step increases. Additional vortices nucleate away from the step in broad rows which are parallel to the step, generally avoiding the thick region of the strip adjacent to the step.

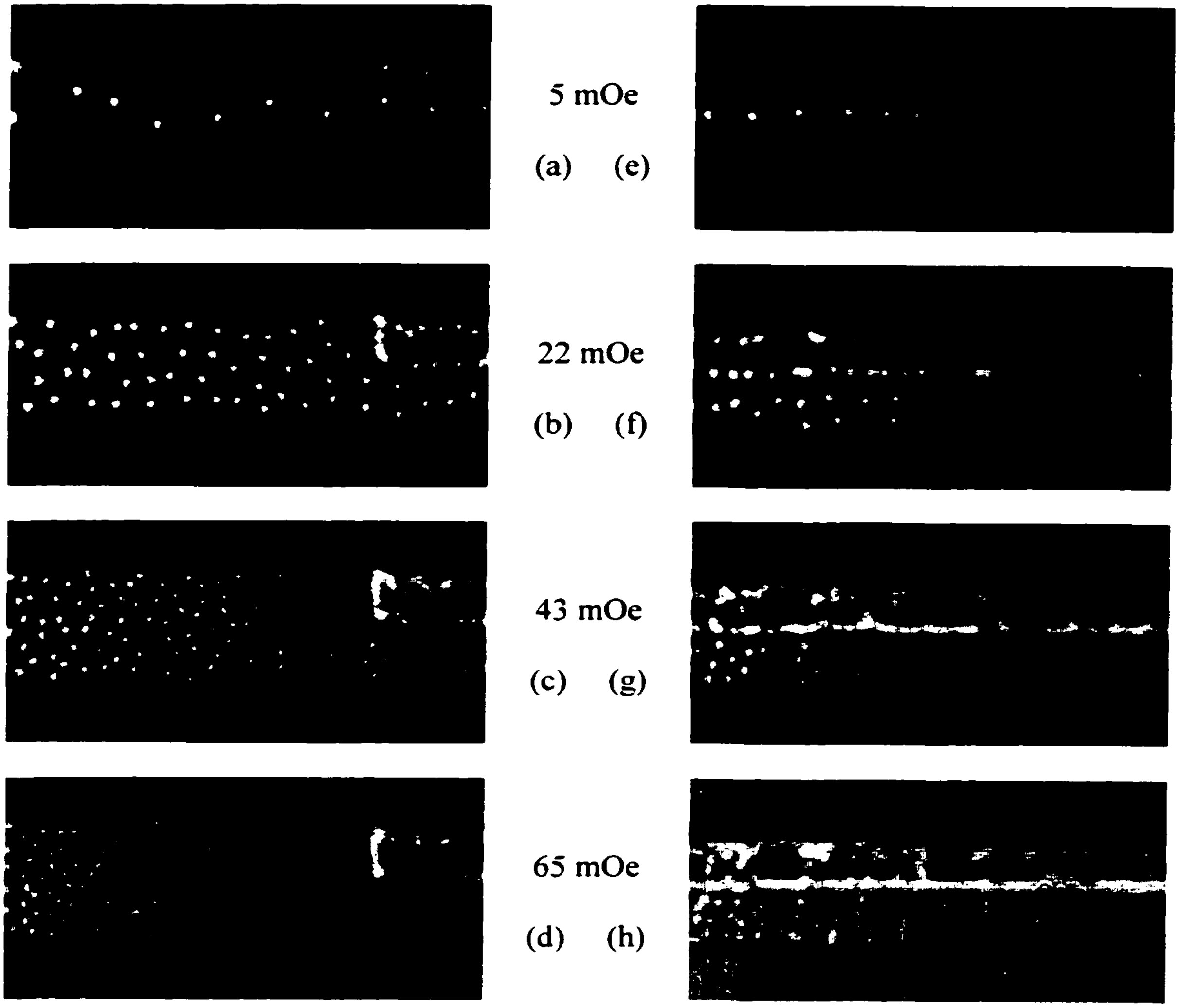

Figure 7.3: Images of vortices in a 150μm wide, 110nm thick Nb strip cooled in four different magnetic fields, as indicated. The images in the left column (a-d) were obtained in a region of uniform strip thickness, except for the upper right 1/4 of the strip where a 55nm surface step begins. The right column (e-h) contains images in the step region, with the 55nm surface step running along the center-line of the strip, such that the thin side is near the top of the image. Image size = 508μm x 254μm.

In the images of Figure 7.3, the density of the vortices away from the step is substantially less than that of the vortices pinned along the step. This behavior is shown in Figure 7.4, which contains line traces of the vortex density across the width of the strip for different magnetic field strengths. This plot was obtained by fitting the approximate location of each vortex in the images, then averaging the vortex density along the length of the strip for each image. The increased vortex density near the step is clearly shown as a large peak at the low side of the step.

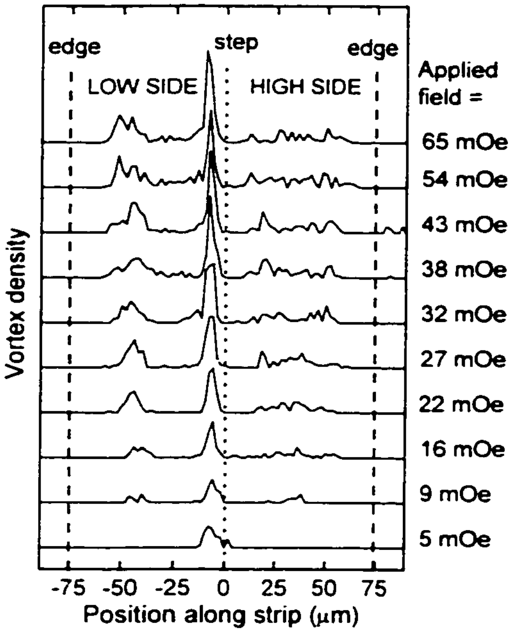

Figure 7.4: Line trace of the vortex density across the width of the strip for various magnetic field strengths, showing the concentration of vortices along the low side of the surface step. The vortex distribution was averaged along the length of the strip.

The disturbance of the vortex distribution by the surface steps can also be seen in images of Nb squares with octagonal surface trenches. Figure 7.5(a) contains an image of a Nb square which was 160nm thick, with a 30nm deep trench, such that the film thickness in the trench is 130nm. The image was obtained around the central octagonal trench in a magnetic field of 65 mOe. The increased vortex density along the low side of the steps and the depletion of vortices at the thick side of the steps is clearly visible. Similar behavior is observed at lower magnetic fields, as in Figure 7.5(b), obtained near the edge of a Nb square with a 50nm deep trench. The sample was cooled in a magnetic field of 22 mOe, and the outer octagonal trench can be seen in the left half of the image. Thus despite the strong bulk pinning in these Nb films, the surface steps provide an attractive force on the vortices, resulting in the high-density rows of vortices along the steps in the SSM images.

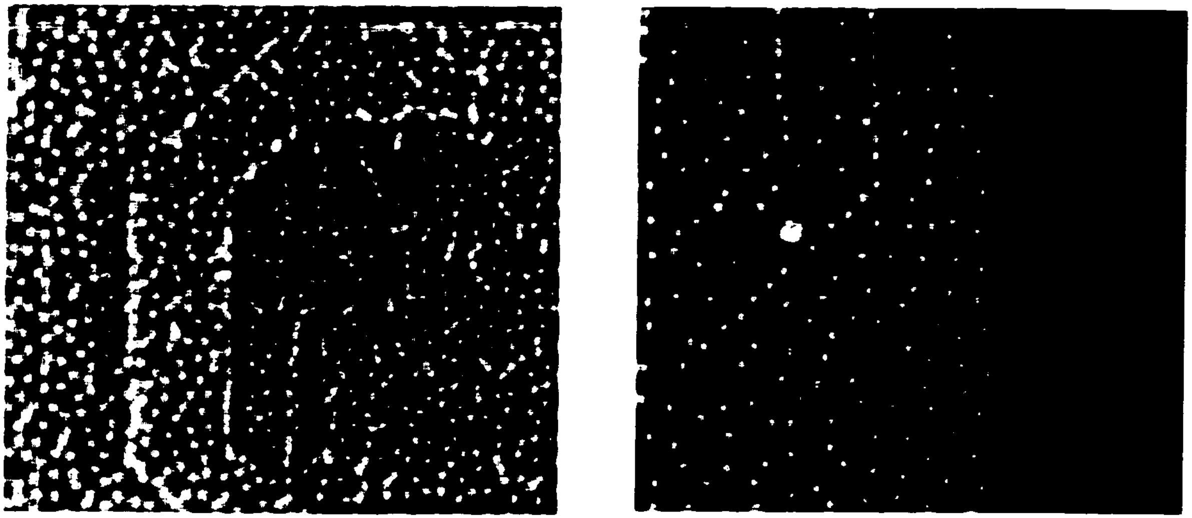
(a) (b)

Figure 7.5: (a) Image around 30nm deep central octagonal trench in a 160nm thick Nb square, cooled in 65 mOe. (b) Image around 50nm deep trench in a 160nm thick Nb square, cooled in 22 mOe. Edge of square towards right side of image. Image size = $(508\mu m)^2$.

7.2.2 Weak-pinning a-MoGe films

We have studied samples of the square pattern with octagonal trenches, fabricated from 200nm thick weak-pinning a-MoGe films. Because of the lack of pinning, field cooling results in well-ordered vortex distributions. Figure 7.6 contains an image of a

200nm thick a-MoGe square with no surface steps which was cooled in a magnetic field of 30 mOe. The vortex distribution exhibits many regions of six-fold orientational order, although there is no clear long-range translational order. This is not surprising, as the vortex spacing at this low magnetic field is about 27μm. This is much greater than $\lambda_\perp$ (= 2.2μm), such that the vortices are only weakly interacting. The vortices are also observed to avoid the edge of the square, located near the right side of the image. This is related to the fact that the Meissner screening current distribution is peaked at the edge of the square, producing a Lorentz force on the vortices which is directed in towards the square center.

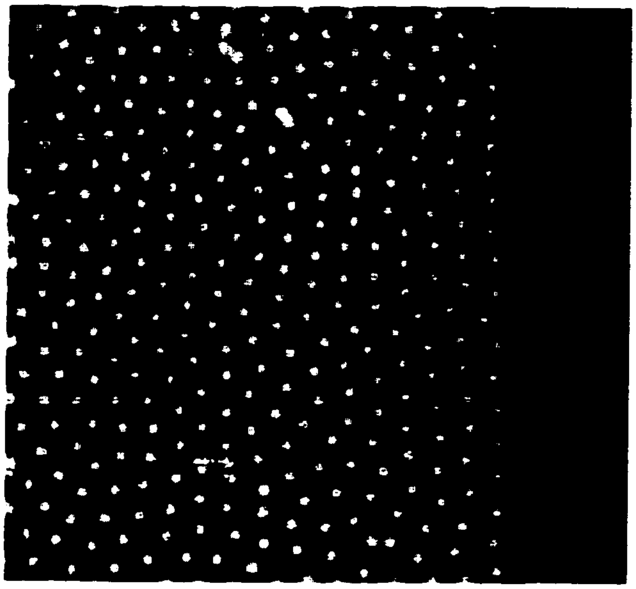

Figure 7.6: Vortex distribution in a 200nm thick weak-pinning a-MoGe square with no surface steps. The sample was cooled in 30 mOe and the edge of the square is visible at the right side of the image. Image size = $(508\mu m)^2$.

Trenches etched into the surface of the a-MoGe squares produce similar distortions of the vortex patterns as were observed in the Nb samples. Figure 7.7 contains SSM images on a square of 200nm thick a-MoGe with trench depths of 125nm, such that the film in the trench was only 75nm thick. The images were obtained for cooling field strengths of 27 mOe and 54 mOe. Again, the images show a much higher density of vortices along the low side of the surface steps. At the thick side of the steps, the vortices form a row which is parallel to the step but offset away from the step. The vortices in the middle of the trenches have a density which is slightly larger than the vortex density in the thick region of the sample, away from the surface steps. For the larger cooling field in Figure 7.7(b), the vortex density increases, with the same general behavior of a concentration of vortices along the low sides of the steps. The variation in the brightness level between vortices in the trench and those outside of the trench is related to the change in the thin-film penetration depth between the two regions, the stray pickup in the SSM flux transformer, and the higher vortex density in the trenches. These contrast variations will be discussed further in Section 7.2.4.

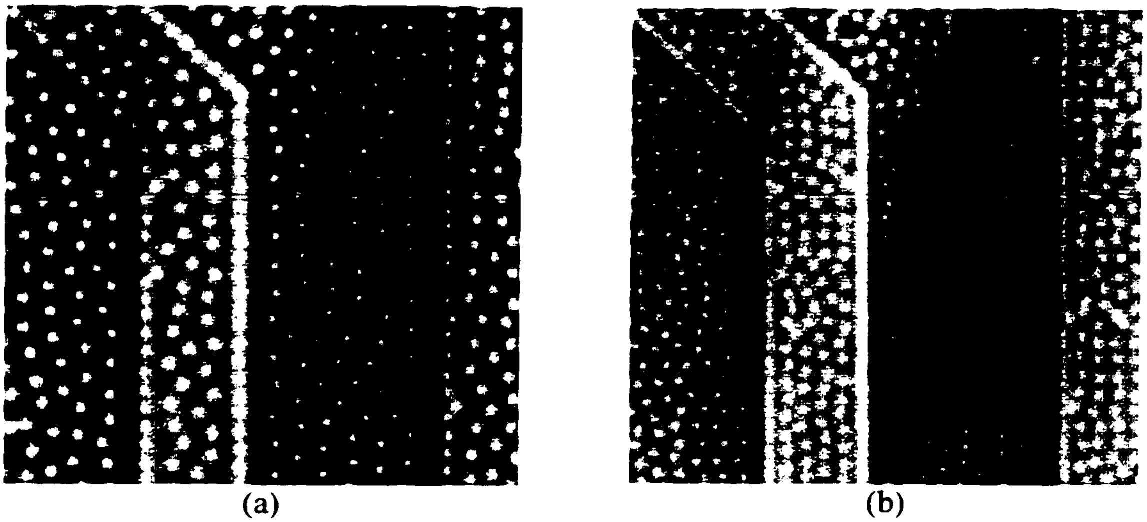
(a) (b)

Figure 7.7: Images near 125nm deep trenches on the surface of a 200nm thick a-MoGe square, cooled in (a) 27 mOe, (b) 54 mOe. Image size = $(508\mu m)^2$.

Figure 7.8 contains an image of another 200nm thick a-MoGe with a 60nm deep trench, cooled in 65 mOe. This image was obtained around the central octagonal trench.

The rows of vortices in the thick region parallel to the step follow the trench as it bends around. This results in regions of enhanced disorder in the vortex distribution which propagate out radially from the bends in the trench, as the vortices must adjust in order to accommodate the formation of rows parallel to the steps. This image also contains several double vortices. These are regions where two or more vortices were attracted to a strong pinning site, such that the vortices were separated by less than the pickup loop diameter, thus appearing as one flux bundle.

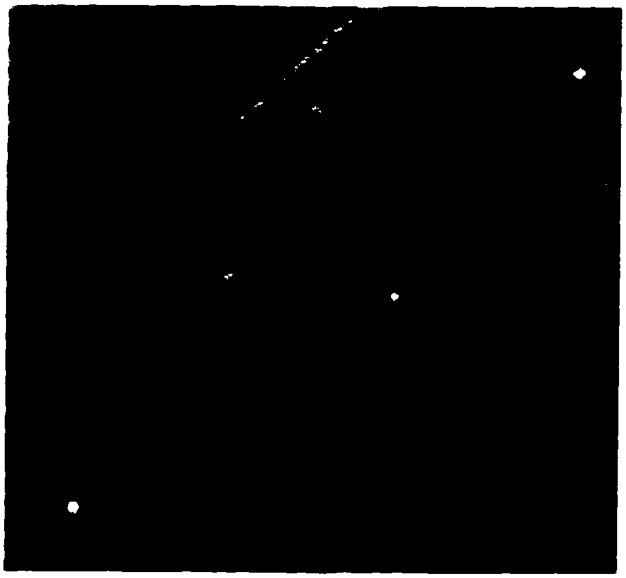

Figure 7.8: Vortex distribution around the central 60nm deep octagonal trench in a 200nm thick a-MoGe square, cooled in 65 mOe. The bending of the vortex rows in the thick regions parallel to the steps generates enhanced disorder in the vortex distribution which propagates outward (towards the left of the image) away from the steps. Image size = $(508\mu m)^2$.

The vortex ordering along the edge of the square can be seen in the image of Figure 7.9(a). This image was obtained around the outer 90nm deep trench near the bottom edge of the square. Vortices are pushed in from the edge of the square, as described earlier for Figure 7.6, although one vortex appears to be pinned near the strip edge at the right side of the image, perhaps due to a strong pinning defect located there. The vortices in the thick region between the trench and the square edge are also pushed away from the outer surface step forming the standard row of vortices parallel to the step. This results in a compression of the vortices between the outer step and the edge of the square, such that the vortices form two nearly perfect staggered rows which are parallel to the step and the square edge.

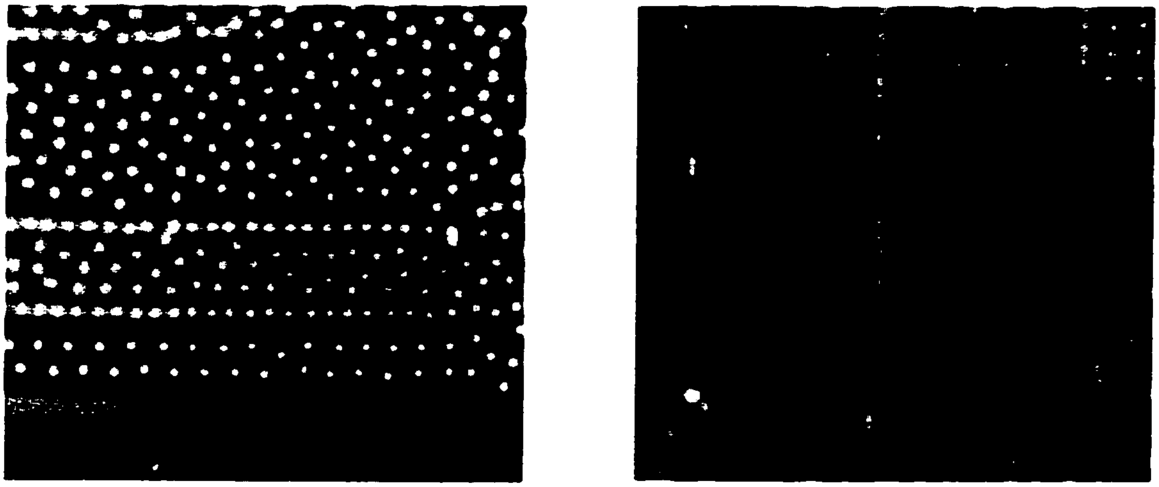
(a) (b)

Figure 7.9: (a) Image near the bottom edge of a 200nm thick a-MoGe square with a 90nm deep trench, cooled in 27 mOe. The vortices between the outer surface step and the square edge are compressed into 2 staggered rows. (b) Vortex distribution around 25nm deep trench on a 200nm thick a-MoGe square, cooled in 27 mOe. Excess defect pinning, combined with the reduced step pinning in this square may play a role in the increased vortex disorder in this image. Image size = $(508\mu m)^2$.

Figure 7.9(b) contains an image of another 200nm thick a-MoGe square with a much shallower 25nm deep trench. The sample was cooled in 27 mOe, and the edge of the square is visible at the left side of the image. The vortex distribution around the surface steps is qualitatively similar to that of the other squares with larger steps, with a higher density of vortices along the low side of the steps. However, the rows of vortices along the steps contain many vacancies, where vortices were most likely attracted away from the step by stronger pinning sites elsewhere. Also, the vortex distribution away from the steps in this square is somewhat more disordered than in the other squares presented above. It is possible that the region of the film occupied by this square contained stronger pinning defects.

The possibility of enhanced vortex pinning due to damage in the trench region caused by the ion milling was tested by fabricating another a-MoGe square sample where the entire surface of the square was partially milled before the trenches were patterned. After etching the square shape into the film, the entire surface of the 200nm thick square was ion milled down to a thickness of 150nm. Octagonal trenches were then patterned and milled to a depth of 43nm. SSM images in the vicinity of the trench displayed the standard concentration of vortices along the low side of the steps and a vortex-free region adjacent to the step. Thus if the milling caused any surface damage in the thick region away from the trench, it did not affect the observed vortex distributions.

7.2.3 Variations of vortex distributions with magnetic field strength and surface step height

In order to quantify the influence of the surface steps on the vortex distributions, we have studied the effects of varying the magnetic field strength and the surface step height around select locations of the a-MoGe squares. Figure 7.10 contains four images obtained around the same section of the middle trench on the a-MoGe square with 90nm deep trenches for different cooling field strengths. The trench runs vertically in the images, such that as one scans across the width of the image, the sample is thinner in the middle, i.e. in the trench, while the sample is thicker at either edge of the image. As the sample is cooled in larger magnetic fields, both the vortex density along the steps and the overall vortex density increase. The width of the vortex-free region adjacent to the thick side of the steps decreases for larger fields. The images in Figure 7.11 were obtained around the same trench region in four different a-MoGe squares, all of which had different trench depths and each square was cooled in the same magnetic field of 32 mOe. The vortex distribution in the vicinity of the trench can be described by four quantities: the vortex spacing in the high-density region along the surface steps, the vortex density in the thick region away from the trench, the vortex density in the trench excluding the high-density vortex row along the steps, and the width of the vortex-free region adjacent to the step.

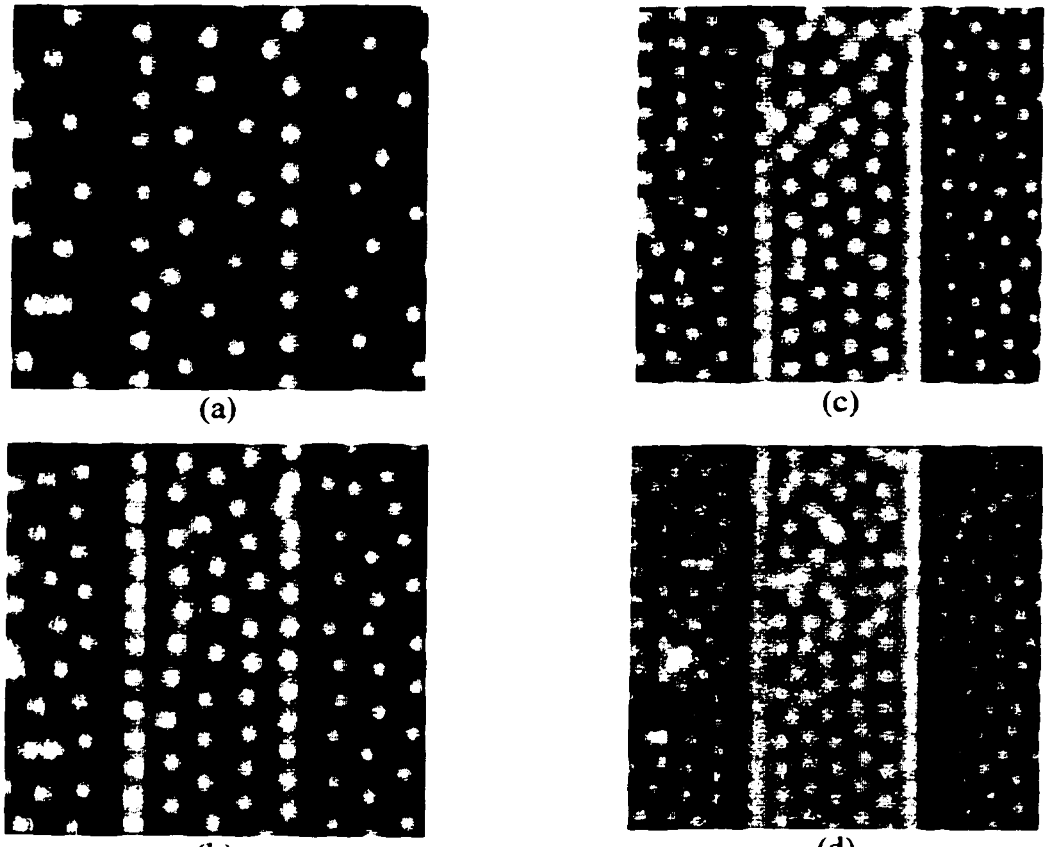

Figure 7.10: SSM images around the middle trench of a a-MoGe square with 90nm deep trenches for cooling magnetic field strengths of (a) 16 mOe, (b) 32 mOe, (c) 48 mOe, (d) 65 mOe. Image size = $(254\mu m)^2$.

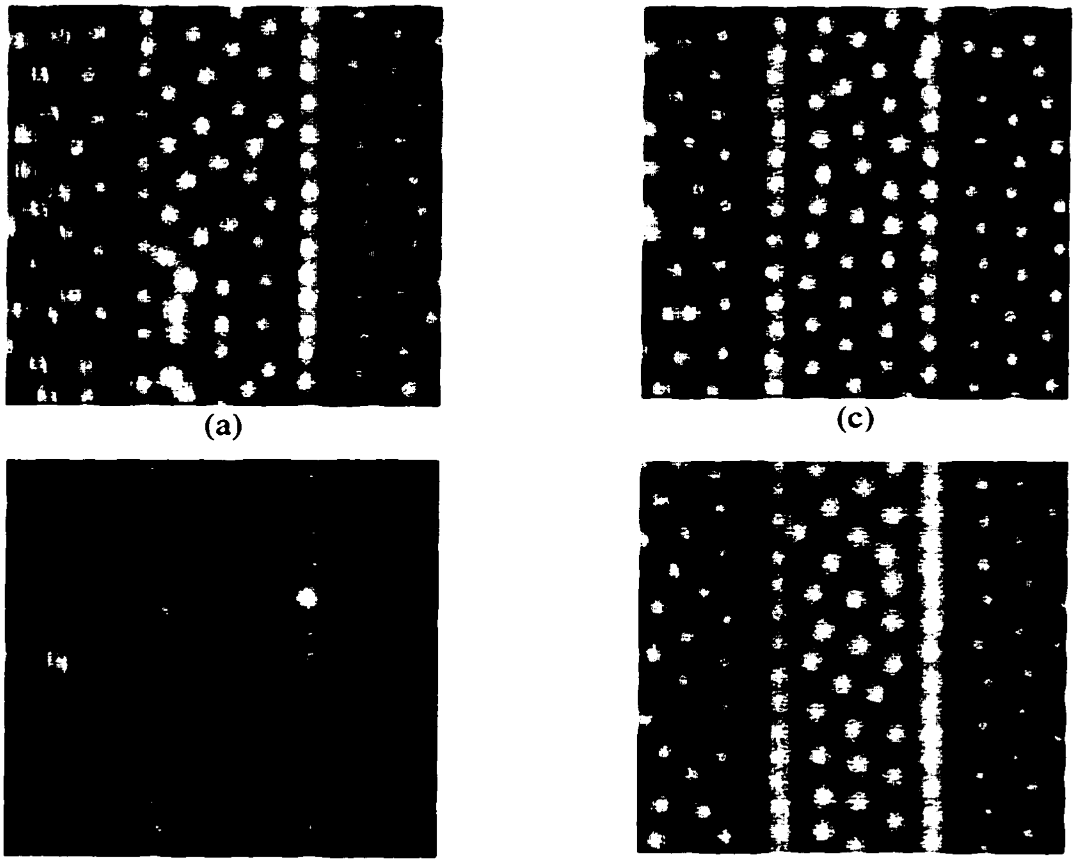

(a) (c)

(b) (d)

Figure 7.11: SSM images around the middle trench of four different a-MoGe squares cooled in 32 mOe with trench depths of (a) 25nm, (b) 60nm, (c) 90nm, (d) 125nm. Image size = $(254\mu m)^2$.

The vortex spacing in the high-density row along the low side of the surface step can be obtained directly from the image by counting the number of vortices in the row along a given length. If the vortex spacing is fairly uniform, then this technique yields a reasonable approximation for the vortex spacing with an estimated uncertainty of 3μm (1.5 scan steps for the images of Figures 7.10 and 7.11). Alternatively, the spacing can be determined by examining the flux variation directly from the image data in a graphing program. A fast Fourier transform (FFT) can be performed on the row of image data along the step, yielding a peak corresponding to the dominant vortex spacing. The two techniques agree within the 3μm error bars except for some of the images at the lowest magnetic fields, as in Figure 7.10(a). In this case, the vortex distribution along the step sometimes contains vacancies, causing the counting technique to overestimate the vortex spacing.

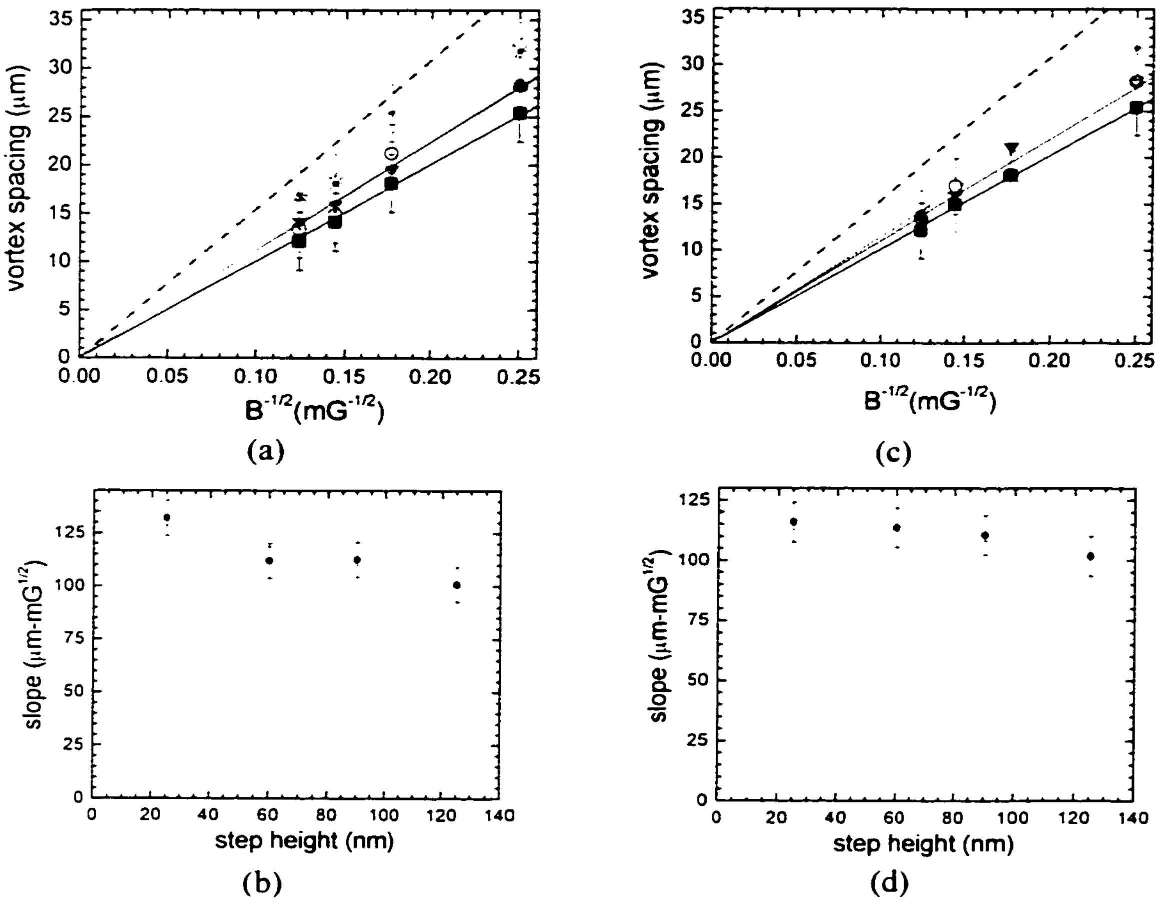

(a) (c)

(b) (d)

Figure 7.12: Plot of the vortex spacing in the high-density row along the low side of the steps for the a-MoGe squares. (a) Vortex row spacing plotted against $B^{-1/2}$ for the four different step heights along the step closer to the edge of the square. The dashed line represents the vortex spacing for a uniform triangular lattice. (b) Plot of the slopes from the fits in (a) showing a small decrease with increasing step height. (c) Vortex row spacing plotted against $B^{-1/2}$ along the step closer to the center of the square. (d) Plot of the slopes from the fits in (c) showing a small decrease with increasing step height. For the symbols in (a) and (c), the solid square=125nm step, open circle=90nm step, solid triangle=60nm step, asterisk=25nm step.

The magnetic flux density in which the sample was cooled can be assumed to be equal to the cooling magnetic field strength for the flat plate geometry of these squares. i.e. $B \approx H_a$. The measured vortex spacing in the rows along the steps can then be plotted against $B^{-1/2}$, as in Figures 7.12(a) and 7.12(c) for the four a-MoGe squares shown in Figure 7.11. The values in Figure 7.12(a) were obtained along the step closer to the edge of the square, while the values in Figure 7.12(c) correspond to the spacing along the step closer to the center of the square. For a uniform triangular vortex lattice, this plot would yield a straight line with a slope of $1.075\sqrt{\Phi_0}$. The spacing along these high-density vortex rows also fits to a straight line passing through the origin, as the spacing should vanish as the field approaches infinity (or H_{c2}). However the vortex spacing in the row along the step increases more slowly than the uniform triangular lattice, corresponding to the increased vortex density observed in the images. For each step height, a linear fit was drawn through the data plotted in Figures 7.12(a) and 7.12(c). The slopes of these fits are plotted against the step height in Figures 7.12(b) and 7.12(d). These graphs show a small decrease in the fit slopes from Figures 7.12(a) and 7.12(c) with increasing step height, corresponding to a slightly greater compression of vortices along the low side of the step for deeper trenches.

The vortex density in the trench, excluding the high-density vortex rows along the steps, can be estimated by counting the number of vortices between the high-density row along each step. The vortex density obtained in this manner is consistently ~10 - 15% higher than the density expected for a uniform vortex lattice with the corresponding value of flux density, $n = B/\Phi_0$. This vortex density is slightly higher for shallower trenches, but this is offset by the somewhat greater compression of vortices along the taller steps, as shown in Figure 7.12. Thus the total number of vortices in the trench, i.e. the sum of the number of vortices in the trench away from the high-density rows and the number of vortices in the high-density rows, is essentially independent of the step height. This behavior can be seen in Figure 7.13(a), where the total number of vortices in the trench for the different step heights is plotted against the cooling flux density, B.

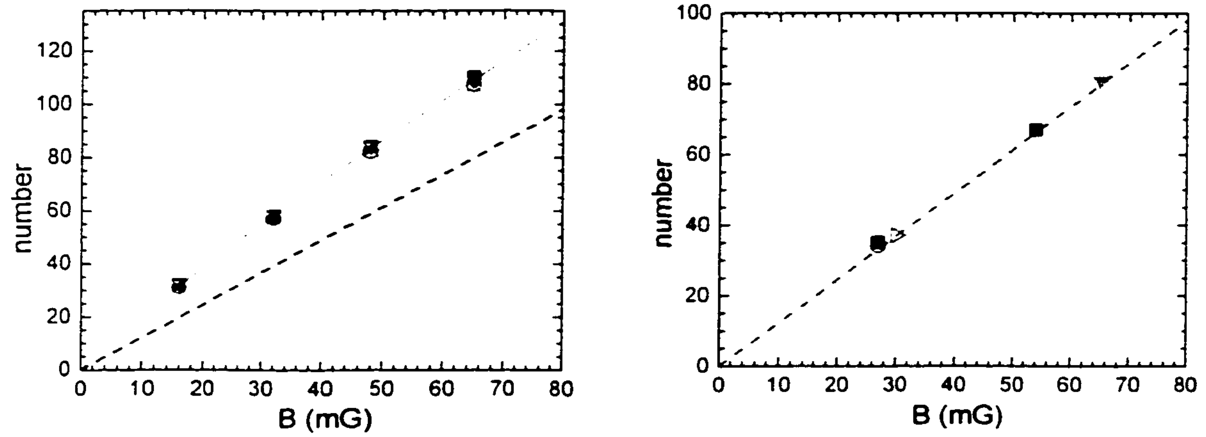

(a) (b)

Figure 7.13: (a) Total number of vortices located in a 254μm long segment of the trench for the four different step heights plotted as a function of B. The solid line through the data points is a best fit given by $2.77 \cdot B^{0.88}$. Dashed line corresponds to the number of vortices expected from B/Φ_0 multiplied by the area (254μm x 100μm). (b) Number of vortices contained in the same area in the thick regions of the squares, away from the trenches. Again, the dashed line corresponds to the B/Φ_0 dependence. Solid square=125nm step, open circle=90nm step, solid triangle=60nm step, asterisk=25nm step, hollow triangle=no step.

For a given value of B, the data for the different step heights vary by no more than 3%. The plot in Figure 7.13(a) also contains a straight line indicating the expected number of vortices for a uniform lattice in the trench, given by B/Φ_0 multiplied by the area of the trench region. The total number of vortices in the trench is up to 60% larger than that expected for a uniform lattice and the data are well fit by a power law with an exponent of 0.88. The slight downward curvature of this fit implies that if this dependence should continue for larger fields, then the density of vortices in the trench should approach the density of a uniform vortex lattice when B ~ 0.9 G.

The vortex density in the thick region of the square, away from the trenches, can be estimated by counting the number of vortices in a given area directly. Such an approach yields a vortex density which is within 5% of the uniform vortex lattice for the corresponding value of B. Figure 7.13(b) contains a plot of the number of vortices in a 254μm x 100μm box drawn entirely in the thick region, away from the steps, for several of the different a-MoGe square samples presented in previous images. All of these data fall close to the uniform vortex lattice dependence, indicated by the dashed straight line.

The width of the vortex-free regions in the thick portion of the square adjacent to the step can be estimated by measuring the distance between the high-density vortex row and a vortex adjacent to the vortex-free region. In order to account for irregularities in the edge of the vortex-free region, this distance was measured at several different locations for each step, and the values were averaged. The widths of the vortex-free regions are plotted against $B^{-1/2}$ in Figures 7.14(a) and 7.14(c) for the four different trench depths. The values in Figure 7.14(a) were obtained near the step closer to the edge of the square, while the values in Figure 7.14(c) correspond to the width near the step closer to the center of the square. The data generally fall along a straight line which is slightly steeper than the intervortex spacing in a uniform triangular lattice. If the square contained a uniform triangular vortex lattice only, then the spacing between the row of vortices along the low side of the step and the first row of vortices parallel to the step on the thick side should be $\left(\sqrt{3}/2\right)a_0$. Figures 7.14(b) and 7.14(d) show that, within the error of the measurement, the width of the vortex-free regions is essentially independent of the step height, over the range of trench depths imaged. However, the vortex-free region near the step which is closer to the center of the square is somewhat wider than the width of the region near the step which is closer to the edge of the square. This difference may be related to demagnetizing effects due to the thin platelet geometry of these squares.

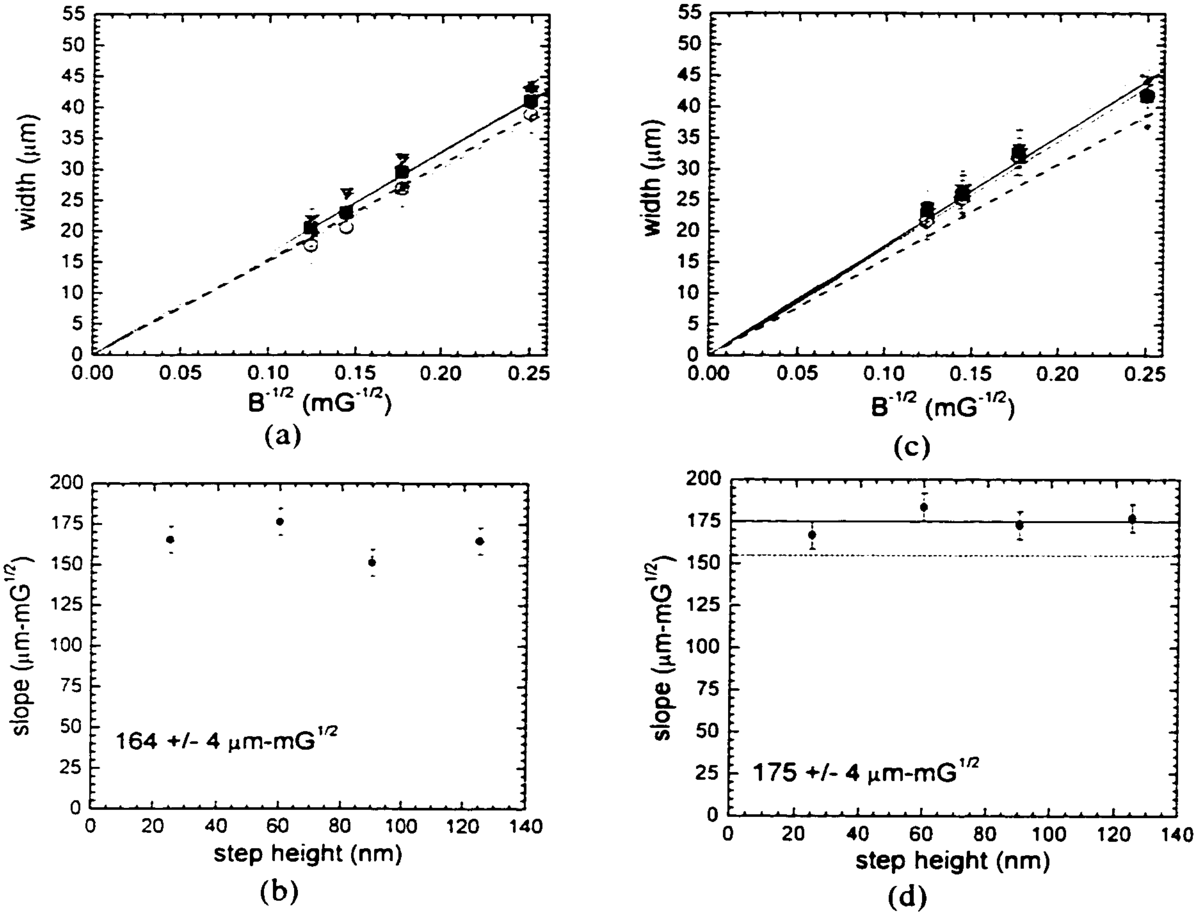

Figure 7.14: Plot of the width of the vortex-free regions adjacent to the surface steps. (a) Width plotted against $B^{-1/2}$ for the four different step heights along the step closer to the edge of the square. The dashed line represents the vortex spacing for a uniform triangular lattice. (b) Plot of the slopes from the fits in (a) showing an independence of step height. (c) Vortex-free width plotted against $B^{-1/2}$ along the step closer to the center of the square. (d) Plot of the slopes from the fits in (c) showing an independence of step height. For (a) and (c), the solid square=125nm step, open circle=90nm step, solid triangle=60nm step, asterisk=25nm step.

The change in the number of vortices contained in the square relative to the number expected for a uniform lattice can be estimated by summing the various quantities described above. For a given value of B, we define the number of "extra" vortices in each trench region as the difference between the total number of vortices in the trench and B/Φ_0 multiplied by the area of the trench. The number of "missing" vortices due to the vortex-free regions is given by the fraction of missing vortex rows multiplied by the number of vortices in a row for that value of B. The missing row fraction is the difference between the fit slopes for the vortex regions, shown in Figures 7.14(b) and 7.14(d), and $\left(\sqrt{3}/2\right)\cdot 154.7\mu m\sqrt{mG}$. This last quantity is the slope of the vortex row variation with B for a uniform triangular lattice. Over the range of magnetic fields we have studied, the number of extra vortices in the trenches is considerably larger than the number of missing vortices in the vortex-free regions. Thus the overall vortex density is roughly 25% larger than the density expected from the expression $n = B/\Phi_0$ over the field range of the images. The field dependence of the various quantities described earlier in this section suggest that this increased vortex density should diminish for larger cooling fields, and should vanish when B approaches 1 G. The increased vortex density could be confirmed by more careful measurements of the vortex spacing over the entire surface of the square. By fitting the vortex positions directly in the image data numerically, it would be possible to extract the vortex spacing more accurately than the counting technique. If the total vortex density is indeed larger than B/Φ_0, then there may be a paramagnetic moment as the square is cooled in small magnetic fields.

7.2.4 Estimates of energy scales

In addition to measuring the vortex spacing from the observed distributions, the energy potential experienced by a vortex can be estimated from the images. Because of the vortex line tension, given by equation 2.10, the vortices in the trench have a lower line energy than vortices in the thick portions of the square. For these a-MoGe films, with λ(4.2 K) = 670nm and κ = 80, the vortex line tension is $2.7x10^{-12} J/m$, or $190 K/nm$. For step heights ranging between 25nm and 125nm, the corresponding change in vortex line energy between the thick and thin parts of the sample varies from $4.8x10^{3} K$ to $2.4x10^{4} K$. These large energy differences are of the same order of magnitude as the increase in the vortex interaction energy due to the distortion of the vortex distribution observed in the images. A "test" vortex located in one of the high-density rows along the low side of a step will experience a higher interaction energy due to the increased density of vortices along the step with respect to a uniform triangular lattice. These intervortex interactions decay slowly, due to the thin-film geometry, as discussed in Section 3.1.2. The potential can be expressed in convenient units in terms of two interacting monopoles of appropriate strength, separated by r_{ij} [5] :

$$V_{ij} = \frac{3.9x10^{4} K - \mu m}{r_{ij}}. \tag{7.1}$$

The interaction potential experienced by the test vortex can be estimated by summing equation 7.1 over the vortex distribution. A rough approximation to the distribution in the images was made by assuming a single high-density row of vortices (i.e. a step) extending across the entire width of the square in the middle. The region below the high-density row was assumed to have the uniform triangular lattice density, while the region above the high-density row was assumed to also have the uniform triangular lattice density, but with an offset corresponding to the vortex-free region. The interaction terms between the test vortex and all the other vortices in the square were summed. The corresponding sum for a uniform triangular lattice occupying the entire square, with the test vortex again at the center of the square, was subtracted from the previous sum. This energy difference should be a rough estimate to the increase in vortex interaction energy due to the distorted vortex distributions around the surface steps observed in the SSM images. Using the measured values for the vortex spacing from the images, this calculation of the energy difference yields values between 10^3 K and 10^4 K, comparable to the scale for the vortex line energy difference at the step.

The interaction energy would be larger still if the somewhat higher density of vortices in the trench excluding the high-density rows were accounted for in the sum. Also, the potential experienced by the test vortex may include terms related to the distortion of the vortex screening currents and magnetic field near the surface steps. A estimation of the associated energy scales would require a full three-dimensional treatment of the profile of a vortex near a surface step, when the step height is much less than the thin-film penetration depth.

7.2.4 Contrast variations around trenches in SSM images

The SSM images of vortices around trenches in a-MoGe squares show a substantial variation in the appearance of vortices located in the trenches compared with those in the thick regions. This behavior can be seen in many of the preceding images, especially Figure 7.7. Vortices in the trench appear brighter and broader than the vortices away from the trenches and the effect is enhanced as the trench depth increases. One factor contributing to this contrast variation is the difference in the thin-film penetration depth between the two regions. In the thick regions of the a-MoGe squares, $\lambda_\perp = 2.2\mu\text{m}$.

while in the trenches this quantity ranges between 2.6μm for the 25nm deep trench and 6.0μm for the 125nm deep trench. This larger value of 6.0μm is comparable to the SSM pickup loop size as well as the height of the pickup loop above the sample surface. The enhanced thin-film penetration depth accounts for the broader appearance of the vortices in the trenches. The enhanced brightness of the images in the trenches is probably related to both the increased vortex density in the trench and the enhanced $\lambda_\perp$. These effects are not observed in images of the vortex distribution around trenches in Nb squares, as these squares are thicker than λ, such that λ does not vary between the thick regions and the trenches.

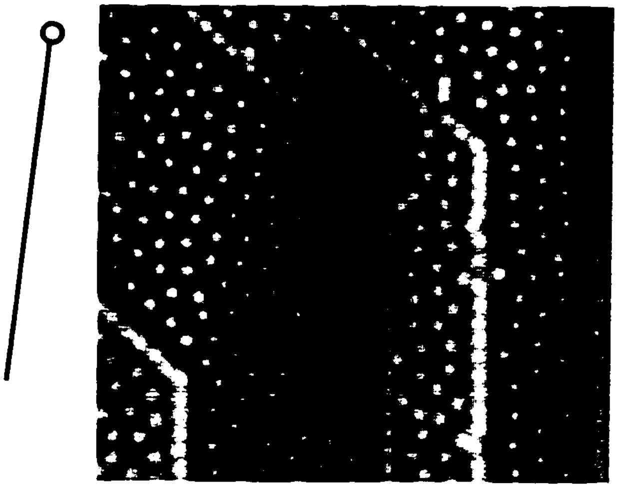

Figure 7.15: SSM image showing the ghosting effect which produces a brighter image of vortices in the thick region beyond the end of the 125nm deep trench. The orientation of the pickup loop and flux transformer relative to the sample is shown to the left of the image. Image size = (508μm)^2.

Other unusual features in the images of a-MoGe squares include the variation in brightness between the left and right steps for a vertically oriented trench, as in Figure 7.7, and the bright regions which extend beyond the trenches, as in Figure 7.15. Both of these facts are related to the ghosting problem due to the pickup of stray flux along the flux transformer away from the pickup loop, as discussed in Chapter 5. The orientation of the pickup loop and flux transformer is shown in Figure 7.15. When the pickup loop passes from the left to the right across the trench, more of the flux transformer sits over the higher-vortex density trench, leading to an increase in the brightness from the left to the right sides of the trench. The bright regions extending beyond the trench are due to the stray pickup of flux as the flux transformer is situated above the higher-vortex density trench while the pickup loop is imaging the vortices beyond the trench. This effect also seems to be enhanced by the large thin-film penetration depth in the deep trenches on the a-MoGe squares, perhaps because this results in a greater variation of the vortex profile at the level of the pickup loop. These ghosting problems could be reduced by improving the screening of the flux transformer inductance.

7.3 Dynamics of vortices near steps

The application of a transport current in the strip samples should probe the vortex response in the vicinity of the surface steps. Moderate transport currents applied to the 150μm wide Nb strips did not shift the field-cooled vortex distributions. Presumably the Lorentz force related to the transport current did not exceed the strong pinning forces in these Nb films. The application of larger transport currents, with average current densities on the order of $10^5 A/cm^2$ produced avalanche-like entry of flux into the strip. Figure 7.16 contains two images of the Nb strip with a surface step running along the center of the strip for large applied transport currents. The flux has burst primarily into the thin side of the strip in large bundles containing many vortices. This behavior was not reproducible, with different flux bundle distributions for a repetition of the same conditions. This process seems to be related to a thermomagnetic instability, as discussed in Section 3.2.6.

(a) (b)

Figure 7.16: SSM images of flux instabilities in a 150μm wide, 110nm thick Nb strip with a 55nm surface step, such that the thin side of the strip is towards the top of the image. There is no external applied magnetic field, and transport currents are applied to the strip, triggering flux avalanches of flux bundles (dark regions) primarily into the thin part of the strip. The transport current was increased to (a) 99.1 mA, (b) 50.4 mA ($\approx 4x10^5 A/cm^2$). Image size = $(254\mu m)^2$.

In the weak-pinning a-MoGe strips, small transport currents easily shifted the vortex distribution across the strip width. Figure 7.17(a) contains an image of the field-cooled distribution in a 150μm wide a-MoGe strip with no surface step and no transport current. In Figure 7.17(b), the transport current was increased to +0.35mA ($\approx 2x10^3 A/cm^2$), with a corresponding Lorentz force towards the top of the image. The vortices are observed to shift towards the top of the image, and the self-field of the transport current can be seen as a brighter contrast of the bottom edge of the strip relative to the top edge. Figure 7.17(c) shows the shift of the vortex distribution towards the bottom edge of the strip for the opposite polarity of transport current.

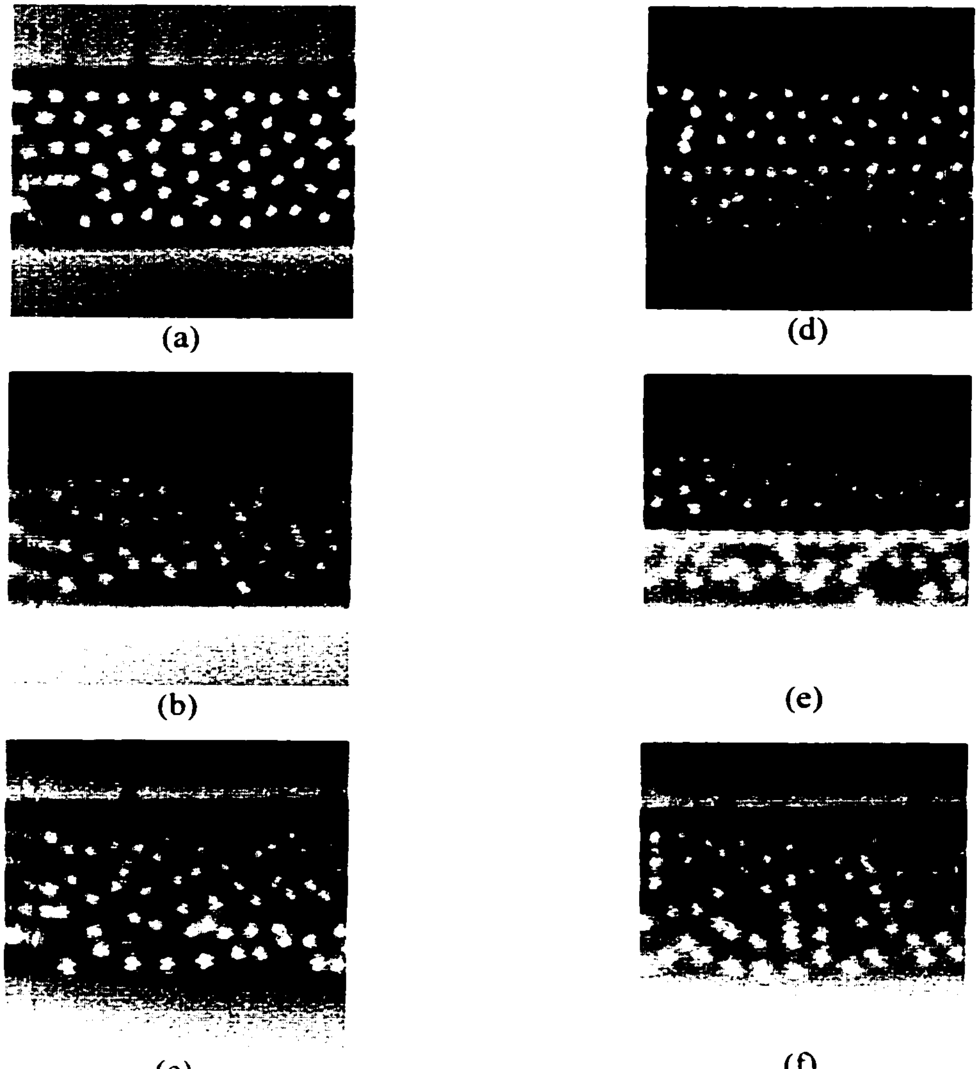

(a) (d)

(b) (e)

(c) (f)

Figure 7.17: Images of vortex shifting in 150μm wide, 100nm thick a-MoGe strips. (a) Strip with no step cooled in 43 mOe, no applied transport current. (b) Strip with no step cooled in 43 mOe, then transport current increased to $+0.35mA$ $(\approx 2x10^3 A/cm^2)$, shifting the vortices towards the top edge of the strip. (c) Strip with no step cooled in 43 mOe, transport current increased to $-0.35mA$, shifting the vortices towards the bottom edge of the strip. (d) Strip with a 40nm step cooled in 43 mOe, no applied transport current. (e) Strip with a 40nm step cooled in 43 mOe, then transport current increased to $+0.25mA$ $(=2x10^3 A/cm^2)$, shifting the vortices towards the top edge of the strip, i.e. against the step. (f) Strip with a 40nm step cooled in 43 mOe, transport current increased to $-0.25mA$, shifting the vortices towards the bottom edge of the strip, i.e. away from the step. Image size = $(254\mu m)^2$.

The addition of a surface step to the strip makes the vortex response asymmetric. Figure 7.17(d) shows the field-cooled vortex distribution in a 150μm wide, 100nm thick a-MoGe strip with a 40nm surface step and no transport current. This image shows the typical vortex distribution, with a higher density of vortices along the low side of the step and relatively few vortices on the thick side adjacent to the step. As the transport current is increased with the Lorentz force directed against the step, the vortices are compressed into the step, but they do not cross from the thin side of the strip to the thick side, as shown in Figure 7.17(e). Thus the vortex line tension barrier at the step impedes vortex motion up the step. For the opposite current polarity, with the Lorentz force directed away from the step, the vortices depin from the step and move towards the bottom edge of the strip, as shown in Figure 7.17(f). At larger values of applied transport current, the images are complicated by the entry of new vortices into the strip due to the self-field of the transport current at the edges of the strip.

7.4 Possible mechanisms for non-uniform vortex distributions near steps

The SSM images presented in the preceding sections show that surface steps have a substantial influence on the vortex distributions in the samples. We propose several possible mechanisms to account for the flux patterns observed in the images.

7.4.2 Flux compression in trenches

The SSM images indicate an increased vortex density in the trenches. The decrease in vortex line energy in the thin trenches could attract vortices from the rest of the square into the trench. The lowering of the line energy would be offset by the increase of vortex interaction energy due the decreased vortex spacing. However, this mechanism should produce a larger vortex compression in the trench for taller surface steps, in contrast to our observations that the number of vortices in the trenches in the SSM images is independent of the trench depth, as shown in Figure 7.13(a).

The vortex distributions around the trenches are reminiscent of the Bitter decoration imaging experiments of Bezryadin et al. [6], discussed in Section 6.1.2. In this work, the authors imaged field-cooled vortex distributions around small ($\leq 2.2\mu$m in radius) circular surface depressions in Nb films. The vortices were compressed into the thinner depressions up to a density which was considerably larger than that in the rest of the film away from the depressions. Also, the vortices were located primarily around the inside of the perimeter, i.e. at the low side of the surface steps. In addition, the observed compression was essentially independent of the depth of the depression. Bezryadin et al. proposed that the increased vortex density in the depressions was caused by a surface superconducting state which developed along the face of the perimeter of the depressions. As the sample was cooled from above T_c in a magnetic field, the faces of the surface steps which are parallel to the field could become superconducting at a slightly higher temperature than the rest of the sample due to the surface superconductivity phenomenon, described in Section 2.2.6. Thus there could be a narrow temperature interval below the temperature at which the faces of the steps become superconducting, $T(H_{c3})$, and above the T_c of the rest of the sample. The requirement of continuity of the surface superconducting order parameter around the perimeter of the depression would cause the compression of flux into the region, with a stepwise increase as more loops are added to the order parameter. As the temperature is lowered through T_c, the flux compression results in a higher vortex density in the depression. A theoretical treatment of this behavior indicated that the amount of flux compression would be independent of the height of the surface steps, as long as the step height remained finite [6].

For the square samples we have imaged, it is unlikely that a single continuous surface superconducting order parameter would exist along the face of the entire perimeter of each of the trenches, as this would cover a length on the order of 1cm. Any surface superconducting state would probably be broken into patches by defects along the length of the steps. Thus the flux could still be compressed into the trenches during the cooling process due to the distortion of the magnetic field lines by the superconducting faces for temperatures between $T(H_{c3})$ and T_c. It may be possible to test for the presence of this surface superconducting state by measuring the resistance along a film with patterned longitudinal trenches as a function of temperature. Upon cooling the film in a small magnetic field, the resistance should drop at some temperature above T_c ($T(H_{c3})$), when the faces of the trenches become superconducting.

The increased vortex density we observe in the trenches seems to imply a total number of vortices in the squares which is higher than expected, based on the value of B, as discussed in Section 7.2.3. This excess flux could result in a paramagnetic moment for the squares at these low magnetic fields. Paramagnetic moments have been reported in magnetization measurements on various superconductors over the past decade, and have been called the Paramagnetic Meissner Effect (PME) [7, 8]. The PME appears as a small positive increase in the field-cooled magnetization upon passing through T_c, instead of the typical diamagnetic response. This effect has only been observed at the smallest magnetic fields, typically less than 1 Oe, while cooling in larger magnetic fields results in diamagnetism below T_c. Samples which exhibit the PME are typically granular or have substantial surface damage [9]. Several mechanisms have been proposed to explain the PME. but many questions about the effect remain.

7.4.2 Increased vortex density along steps

In addition to the higher vortex density observed in the trenches. our SSM images also indicate a substantially smaller vortex spacing in the row of vortices pinned along the low side of each surface step. This may be caused by the increased repulsion of vortices in the higher-density trenches pushing outwards on the vortices. The vortices would then be compressed into the steps. as the line energy barrier of the step would prevent these vortices from moving across to the thick region of the square.

It is also possible that a vortex in a thin region of the sample is attracted to the low side of the surface step due to a distortion of the vortex field and screening current density distribution at the step. An understanding of such an attraction would require a detailed calculation of the field lines and current distributions in three-dimensions in the vicinity of a surface step. Mkrtchyan and Schmidt treated the interaction of vortices with the interface between two superconducting regions with different penetration depths [10]. The authors calculated the formation of a vortex potential minimum located near the interface. leading to the pinning of a row of vortices along the interface. Such a mechanism could be applied to the a-MoGe square trench samples presented in this work. as the thin-film penetration depth is indeed different between the thin region in the trench and the thick regions in the rest of the square. However. the treatment must be altered to account for the change in line energy at the step and to include possible distortions of the magnetic field at the face of the step.

The vortex-free regions adjacent to the surface steps are probably caused by the screening currents associated with the increased vortex density in the trench. A calculation of the screening current distributions in a similar situation was performed by Mkrtchyan et al. [11]. The authors treated the interaction of a vortex with a circular cavity in a superconductor. If flux was trapped in the cavity, then the screening currents associated with this flux were peaked near the perimeter of the cavity. Thus a vortex outside of the cavity would be pushed away due to the Lorentz force associated with the screening currents. If more flux was trapped in the cavity, then the current density peak moves in closer to the perimeter of the cavity, and the width of the vortex-free region adjacent to the cavity should decrease.

7.5 Conclusions and future work

We have studied vortex interactions with surface steps through direct magnetic imaging of the vortex distributions using an SSM. Near a surface step, we observe a higher density of vortices along the thin side of the step, along with a smaller amount of vortices in the thick region adjacent to the step. The vortices pinned along the low side of the step exhibit an asymmetric response, as a Lorentz force directed away from the step causes the vortices to depin easily, while a Lorentz force against the step causes the vortices to compress, but not cross the step. Also, a larger step pins vortices somewhat more effectively, as observed in images around surface trenches. The presence of a trench etched on the surface of the superconductor causes a compression of flux to a density which is larger than the magnetic flux density in which the sample was cooled. The enhanced vortex density in the trench as well as the width of the vortex-free regions adjacent to the trenches are independent of the step height over the range we have studied. By accounting for the vortex density over the entire sample, the images indicate an overall enhancement in the flux density on the order of 10% beyond that expected from the value of B during the field cooling process.

The vortex distributions around the surface trenches may possibly be explained by a surface superconductivity mechanism along the face of the surface steps, causing a compression of vortices into the trenches. The amount of flux compressed into the trench would be constant, as long as the step height remained finite. However, a taller step may lead to the enhanced pinning of vortices along the step, such that squares with shallower trenches would show more disorder in the vortex row along the low side of the step. This would be consistent with our images which show vacancies and a lower density of vortices along the low side of the smaller steps. The higher vortex density in the trench causes screening currents to flow along the thick region of the sample adjacent to the step. Such a screening current distribution could lead to the repulsion of vortices away from the thick side of the step, as studied by Mkrtchyan et al. [11].

In order to test these possible mechanisms, it would be useful to image more samples with an even wider range of trench depths. Also, if the thick region of the square were thinner as well, it is possible that the thin-film penetration depth could exceed the pickup loop diameter and height above the sample surface. In this case, the vortex images would no longer be resolution-limited, and it might be possible to resolve the distortion of the vortex fields near a surface step. If the flux compression is caused by a surface superconducting state, then it should be possible to destroy the surface superconductivity by coating the sample with a normal metal layer, such as copper. The presence of the normal metal would change the order parameter boundary conditions at the step face and would prevent the higher transition temperature in these regions. Also, it would be instructive to perform global magnetization measurements on these square samples with surface trenches. If the total number of vortices in the samples is higher than the flux density in which the sample was cooled, then the samples may show a paramagnetic response upon field cooling.

7.6 References

[1] P. H. Kes and C. C. Tsuei, *Two-dimensional collective flux pinning, defects, and structural relaxation in amorphous superconducting films*, Phys. Rev. B **28**, 5126 (1983).

[2] M. H. Theunissen and P. H. Kes, *Resistive transitions of thin film superconductors in a magnetic field*, Phys. Rev. B **55**, 15183 (1997).

[3] M. V. Marchevsky, Ph. D. Thesis (Leiden University, Leiden, 1997).

[4] K. Osborn, *Private Communication* (2000).

[5] D. A. Huse, *Magnetic-flux patterns on the surface of a type-II superconductor*, Phys. Rev. B **46**, 8621 (1992).

[6] A. Bezryadin, Y. N. Ovchinnikov, and B. Pannetier, *Nucleation of votices inside open and blind microholes*, Phys. Rev. B **53**, 8553 (1996).

[7] W. Braunisch, N. Knauf, V. Kataev, *et al.*, *Paramagnetic Meissner Effect in Bi High-Temperature Superconductors*, Phys. Rev. Lett. **68**, 1908 (1992).

[8] D. J. Thompson, M. S. M. Minhaj, L. E. Wenger, *et al.*, *Observation of Paramagnetic Meissner Effect in Niobium Disks*, Phys. Rev. Lett. **75**, 529 (1995).

[9] D. J. Thompson, L. E. Wenger, and J. T. Chen, *Inducing the paramagnetic Meissner effect in Nb disks by surface ion implantation*, Phys. Rev. B **54**, 16096 (1996).

[10] G. S. Mkrtchyan and V. V. Shmidt, *Interaction Between a Vortex and the Boundary Between Two Superconductors*, JETP **36**, 352 (1973).

[11] G. S. Mkrtchyan and V. V. Schmidt, *Interaction between a cavity and a vortex in a superconductor of the second kind*, JETP **34**, 195 (1972).

CHAPTER 8

TRANSPORT MEASUREMENTS OF VORTEX DYNAMICS IN THIN-FILM SUPERCONDUCTING STRIPS

The behavior of vortices in thin superconducting strips in a perpendicular magnetic field is a complex problem due to the large demagnetizing effects. The associated geometrical and surface barriers are frequently encountered in thin-film superconductor device applications and in transport measurements on typical high-Tc superconductor crystals. A description of the vortex dynamics is difficult, due to divergent terms in the solutions for the current density near the strip edge, but reasonable approximations as well as numerical solutions can be made. Many of the predictions from these theoretical approaches, particularly for small applied magnetic fields, have not yet been tested experimentally.

8.1 Theoretical treatments of critical currents in thin strips

For the case of a thick superconducting slab, currents in the slab flow primarily at the surfaces, decaying exponentially into the slab with the penetration depth as the characteristic length. This distribution can be obtained by solving the London equation and the Maxwell equation for the slab, as in Section 2.1.3. The current can be due either to an applied transport current or screening currents in response to an external magnetic field, or both. If the superconductor is a thin, wide strip with the external magnetic field oriented along the thin axis, as shown in Figure 8.1, then the current distributions are significantly altered due to the large demagnetizing effects.

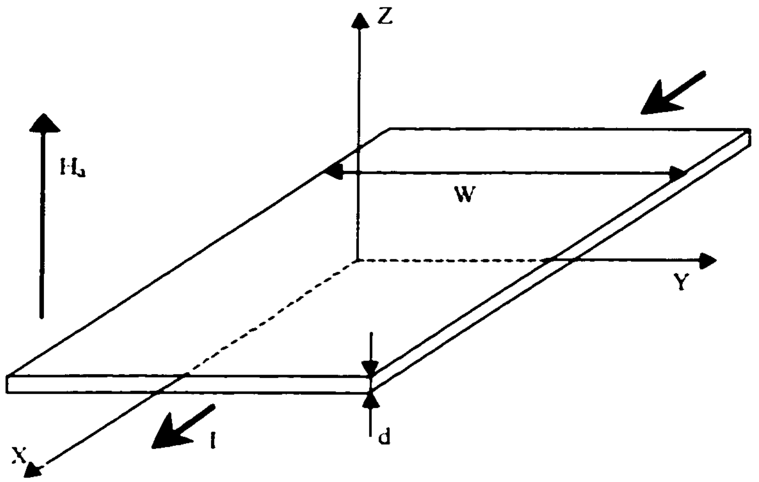

Figure 8.1: Thin superconducting strip in a perpendicular magnetic field.

8.1.1 Basic equations for the current density in a thin strip

An equation for the current density or the vector potential in the strip can be obtained by again applying both the London equation and the Maxwell equation. This problem has been addressed by many groups, including Kupriyanov and Likharev [1], Vodolazov and Maksimov [2], Benkraouda and Clem [3], and Brandt and Indenbom [4]. If the strip is oriented as in Figure 8.1, the symmetry of the problem dictates that J and A should be directed along the X-axis and should only vary in the Y and Z directions. The following boundary conditions should apply:

$$\left.\frac{\partial A_x}{\partial Y}\right|_{Y\to\pm\infty} = -H_a, \quad \left.\frac{\partial A_x}{\partial Z}\right|_{Z\to\pm\infty} = 0. \tag{8.1}$$

thus the magnetic field should approach the external applied field at large distances from the strip. Also, the current density integrated over the cross-section of the strip must equal the applied transport current:

$$\int_{-d/2}^{+d/2} dZ \int_{-w/2}^{+w/2} dY \big(J(Y,Z)\big) = I. \tag{8.2}$$

The Maxwell equation relating A and J is:

$$\nabla^2 \vec{A} = -\frac{4\pi}{c}\vec{J}. \tag{8.3}$$

This relation can be can be inverted using the Green's function for the 2D Laplacian operator. From the London equation:

$$\vec{J} = -\frac{c}{4\pi\lambda^2}\vec{A}. \tag{8.4}$$

the inverted expression from 8.3 can be written as an integral equation for A_x:

$$A_x(Y.Z) = -H_a Y + \frac{1}{2\pi\lambda^2}\int_{-w/2}^{w/2} dY' \int_{-d/2}^{d/2} dZ' \left(\ln\left|\vec{R} - \vec{R'}\right| + C \right) A_x(Y'.Z'). \tag{8.5}$$

where $\vec{R} = (0.Y.Z)$. and C is a constant which can be evaluated by applying the boundary condition of equation 8.2. For the thin strip geometry. W/d >> 1. and equation 8.5 can be simplified by averaging over the thickness. yielding an equation for the thickness averaged vector potential:

$$\frac{\lambda_\perp}{W}\overline{A}(y) = -H_a y \frac{\lambda_\perp}{2} + \frac{1}{4\pi}\int_{-1}^{1} dy' \ln\left|y - y'\right| \overline{A}(y'). \tag{8.6}$$

where the dimensionless coordinate y=2Y/W has been introduced. and $\lambda_\perp$ is the thin-film penetration depth. discussed in Section 3.1.2. Equation 8.6 is valid for the entire strip width except within about a penetration depth of the strip edge (y=+/-1).

The above equations have been derived for the Meissner response of the strip. If flux is present in the strip. then the spatial variation of J and A due to the vortex screening currents must be accounted for. The Laplacian operator in equation 8.3 must now be applied in 3D. After inverting the Maxwell equation with the 3D Green's function. then averaging over x and y on length scales much larger than the intervortex spacing and averaging over the thickness, one obtains an equation for the thickness averaged current density, j(y):

$$\frac{8\pi\lambda_\perp}{cW}\frac{dj(y)}{dy}+\frac{2}{c}\int_{-1}^{+1}dy'\,\frac{j(y')}{y-y'}=-H_a+n(y)\Phi_0. \tag{8.7}$$

The quantity n(y) describes the spatially averaged vortex distribution across the strip width [1, 2]. For the Meissner state of the strip (no flux), n(y)=0, and equation 8.7 is equivalent to 8.6.

8.1.2 Solution for current density and critical current in the Meissner state

The integral equation 8.7 was solved by Kupriyanov and Likharev [1] for the limit of a wide strip, $W/\lambda_\perp >> 1$. In this limit, the term on the left-hand side can be neglected.

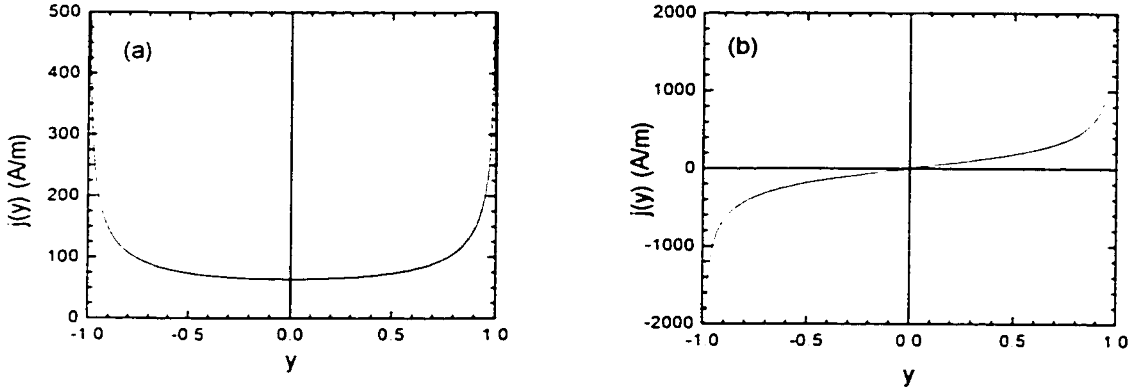

Figure 8.2: Current density for a thin strip in the wide strip limit ($W/\lambda_\perp >> 1$) from equation 8.8, using SI units, such that the thickness-averaged current density, j, is in units of A/m, strip width = 10μm. (a) Current density distribution for applied transport current, I = 10mA, while $H_a = 0$. (b) Current density distribution for applied magnetic field, H_a = 500 A/m (6.3 Oe), I = 0.

The resulting equation can be solved by conformal mapping [1, 3], giving the thickness-averaged Meissner current density response to a transport current, I and external magnetic field, H_a:

$$j(y)=\frac{2I}{\pi w\sqrt{1-y^2}}+\frac{cH_a y}{2\pi\sqrt{1-y^2}}. \tag{8.8}$$

This expression diverges near the strip edges, as shown in the plots in Figure 8.2. A similar expression for the Meissner screening current alone was presented earlier in equation 3.27. An expression for j(y) which is valid over the entire strip width and for strips of finite width was obtained by numerically solving the complete equation for A_x, equation 8.5 with the term on the left hand side (or, equivalently the dj/dy term in 8.7) included [2], resulting in the approximate expression:

$$j(y)=\frac{I}{\gamma W\sqrt{1-y^2+\delta}}+\frac{cH_a y}{4\pi\sqrt{\alpha\left(1-y^2\right)+\beta}}. \tag{8.9}$$

The parameters in equation 8.9 are given by:

$$\beta\approx\frac{2\lambda_\perp}{\pi W}+4\left(\frac{\lambda_\perp}{W}\right)^2 \tag{8.10}$$

$$\alpha\approx\frac{1}{4}-\frac{0.63}{\left(W/\lambda_\perp\right)^{0.5}}+\frac{1.2}{\left(W/\lambda_\perp\right)^{0.8}} \tag{8.11}$$

$$\delta\approx\frac{8}{\pi}\frac{\lambda_\perp}{W}+\left(\frac{33.76}{\frac{W}{\lambda_\perp}+21.45}\right)\frac{\lambda_\perp}{W} \tag{8.12}$$

$$\sin\gamma=\frac{1}{\sqrt{1+\delta}}. \tag{8.13}$$

The variation of these parameters with the ratio, $W/\lambda_{\perp}$, is shown in Figure 8.3. In the wide strip limit, equation 8.9 approaches equation 8.8 away from the strip edges.

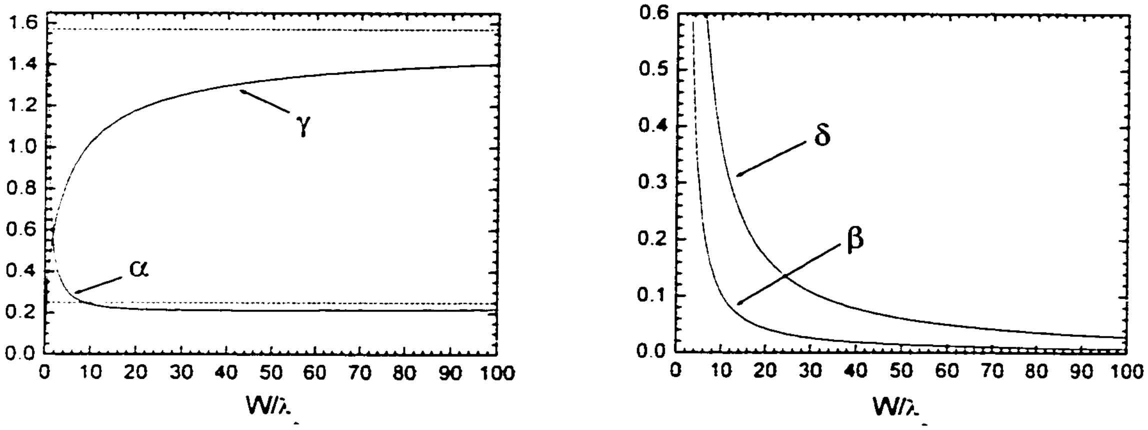

Figure 8.3: Variation of the dimensionless parameters α, β, δ, and γ with $W/\lambda_{\perp}$ using equations 8.10 - 8.13. For large $W/\lambda_{\perp}$, α approaches 1/4, while γ approaches $\pi/2$, as indicated by the dashed straight lines. β and δ approach zero as $(W/\lambda_{\perp})^{-1}$ for large $W/\lambda_{\perp}$.

Upon obtaining the current density, j(y), it is possible to calculate the critical current of the strip, I_c, by expressing the condition for vortex entry at the right edge of the strip. Vodolazov and Maksimov assumed that vortex entry occurs when the current density at the strip edge reaches some critical surface entry current density:

$$j(+1) = j_s . \qquad (8.14)$$

Vodolazov, Maksimov, and Brandt studied vortex entry into thin-film superconductors by numerically solving the time-dependent Ginzburg-Landau equations in 2D [5]. The authors found that an instability occurred when the current density at the edge, j(+1), approached the Ginzburg-Landau depairing current, $j_{GL} = d \cdot J_{GL}$ (J_{GL} given by equation 2.7) [5, 6]. At this instability, a chain of vortices nucleates along the strip edge. In the absence of bulk pinning in the strip, these edge vortices are swept completely across the strip as the current density at the edge is increased further. The vortex motion generates a longitudinal voltage, and the strip is no longer in the supercurrent state. The critical current of the strip then corresponds to the condition:

$$j(+1) \approx j_{GL}. \tag{8.15}$$

If the edge contains defects, then this instability occurs for a lower current density, as the current is concentrated near defects, facilitating vortex nucleation. Thus $j_s < j_{GL}$ for an edge with imperfections [6]. The reduction of the surface barrier by surface defects was considered by Aladyshkin et al. [7].

The critical current as a function of applied field can be found by equating j(+1) from equation 8.9 with j_s and by assuming $I = I_c$:

$$I_c(H_a) = I_c(0) - \gamma\sqrt{\frac{\delta}{\beta}}WH_a. \tag{8.16}$$

$$I_c(0) = j_s W\gamma\sqrt{\delta}, \tag{8.17}$$

with the expressions written in SI units for later comparison with experimental measurements [6]. In the wide strip limit, $\gamma\sqrt{\delta/\beta} \approx \pi$, and expression 8.16 coincides with the result obtained by Kupriyanov and Likharev [1]. From equation 8.16, the critical current for a thin-film strip with no bulk pinning should initially decrease linearly with an increase of the applied magnetic field. For wide strips, the slope, dI_c/dH_a should scale with the strip width, W, while for finite width strips, the width dependence of the parameters, γ, δ, and β must be considered, as plotted in Figure 8.3. In the wide strip limit, the zero-field critical current, $I_c(0)$ scales with the width and thickness as:

$$I_c(0) \propto \sqrt{W}.\sqrt{d}, \tag{8.18}$$

because $j_s = d \cdot J_s$. In the opposite limit of a narrow strip, $I_c(0)$ approaches the behavior:

$$I_c(0) \propto W.d. \tag{8.19}$$

As stated earlier, the above derivations apply for the thin-film limit, $d < \lambda$. If the strip thickness is greater than the penetration length, then the vortices are allowed to bend, as the tilt modulus becomes finite. Vortex entry is then a more complex process, as tilted vortices can initially cut across the corners at the edge of the strip. This is related to the problem of the geometrical barrier, discussed in Section 3.3.2. Vodolazov and Maksimov considered the entry of vortices into a thick strip by calculating the z dependence of the current density [2]. The authors found that the current density, $j(y,z)$ reached a maximum at the corners of the edge, providing a reduction in the order parameter and allowing the entry of tilted vortex segments. However, entry of complete vortices cannot occur until the edge current density at z=0, $j(1,0)$ reached j_s. If vortex entry at the edge is delayed until the field at the edge, $H(1,0)$ reaches H_c, then the process is similar to the Bean-Livingston surface barrier. However, if edge defects reduce the critical surface entry current density such that vortices enter the strip when $H(1,0) \approx H_{c1}$, then the situation is reduced to the geometrical barrier discussed in Section 3.3.2 where the vortex line tension effects dominate the vortex entry and motion.

Benkraouda and Clem studied the field dependence of the critical current for a wide, thick superconductor strip, W >> d > λ, with rounded edges (radius of curvature = d/2) [3]. The authors obtained the expression:

$$I_c(H_a) = I_c(0) - \pi W H_a\left(\frac{R+1}{R}\right), R = \sqrt{\frac{W}{d}}. \tag{8.20}$$

$$I_c(0) = \frac{\pi W H_s}{R}. \tag{8.21}$$

for the low-field Meissner response of the strip. In the limit of W/d >> 1 and W/λ >> 1, these expressions approach the thin-film critical current values from equation 8.16 and 8.17.

8.1.3 Solution for current density and critical current with flux present

The critical current expressions obtained in the previous section only apply at sufficiently low magnetic fields, when the strip is in the Meissner state. As the magnetic field is increased, vortices can enter the strip and form a static mixed state. To compute the critical current in this case, one must solve equation 8.7 for the current density with a non-zero vortex distribution, n(y), as first done by Kupriyanov and Likharev [1]. With no applied transport current, as the magnetic field is increased, vortices will enter the strip at both edges when the screening current density at the edges, j(+/-1) reaches j_s. If there is no bulk pinning in the strip, the vortices will be pushed towards the strip center from both sides. The mutual repulsion of the vortices results in a dome-like vortex distribution with a maximum at y = 0. Because of the lack of pinning, no current can flow in the vortex dome region, thus displacing the screening currents out to the sides of the strip, i.e. between the dome and the strip edges. Conversely no vortices can reside in the current flow regions, as the Lorentz force would immediately sweep these vortices into the vortex dome. If a transport current is then applied to a strip in the vortex state, the dome will be shifted to one side of the strip due to the Lorentz force.

The solution of Kupriyanov and Likharev for equation 8.7 in the wide, thin-film limit assumes that the dome extends from y_1 to y_2 with width 2Θ. The center of the dome is given by:

$$y_0 = \frac{y_1 + y_2}{2} = -\frac{4I}{cWH_a}. \tag{8.22}$$

$$a = \frac{y - y_0}{\Theta}. \tag{8.23}$$

where a is the displacement relative to the dome center. We have returned to Gaussian units for the computation of j(y). The solution for the dome profile is then:

$$n(y) = \frac{\Theta H}{\Phi_0}\sqrt{\frac{1-a^2}{1-y^2}}, |a| < 1. \tag{8.24}$$

The thickness-averaged current density away from the dome is given by:

$$j(y) = \frac{\Theta Hc}{2\pi}\sqrt{\frac{a^2-1}{1-y^2}}, |a| > 1. \tag{8.25}$$

The spatial variation for the vortex dome and the current density are plotted in Figure 8.4. As with the solution for the Meissner state, these solutions break down within about a penetration length of the strip edge. Vodolazov and Maksimov obtained expressions for j(y) and n(y) which are valid over the entire strip width and for finite width strips by solving the complete equation for the vector potential with flux present [2]. These expressions again contain parameters from the numerical solution and approach equations 8.24 and 8.25 in the wide strip limit.

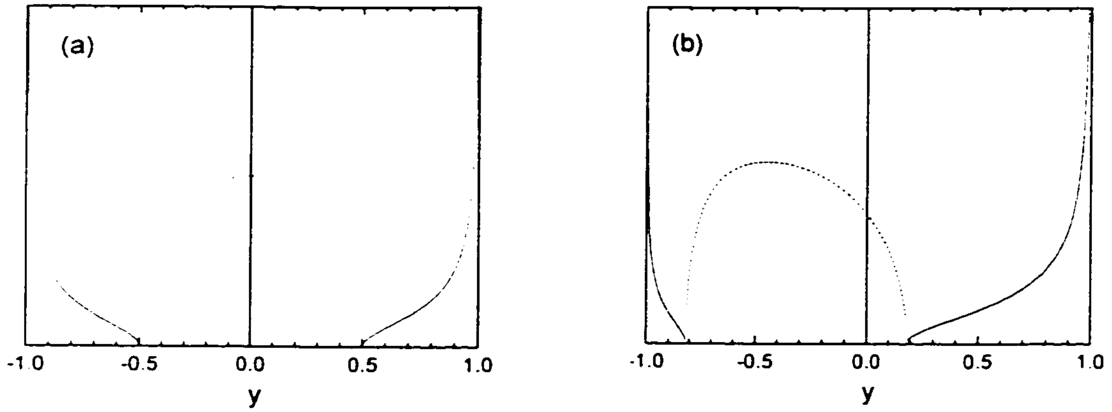

Figure 8.4: Distribution of the vortex dome and the current density distribution across the strip width in the wide strip limit. (a) I = 0. (b) I ≠ 0. The dashed line indicates the qualitative behavior of B(x), corresponding to the flux dome, while the solid lines represent j(y). An exact calculation would require knowledge of the specific entry conditions, hence the lack of a vertical scale in these two plots.

The critical current for a strip in the vortex state is reached when the dome is shifted such that the left edge of the dome reaches the left edge of the strip, $y_l = -1$, and the vortex entry condition at the right edge of the strip is satisfied, $j(+1) = j_s$. Applying these conditions to the dome and current density distributions, Vodolazov obtained the field dependence of the critical current (again, switching to SI units) [2]:

$$I_c(H_a) = \frac{I_c^2(0)}{4WH_a}\gamma^{-1}\sqrt{\frac{\beta}{\delta}}, \tag{8.26}$$

where β, δ, and γ are given by equations 8.10, 8.12, and 8.13. Using equation 8.17 to replace $I_c(0)$ yields:

$$I_c(H_a) = \frac{j_s^2 W}{4H_a}\left(\gamma\sqrt{\beta\delta}\right). \tag{8.27}$$

The quantity $(W/\lambda_\perp)\gamma\sqrt{\beta\delta}$ varies only slightly with $W/\lambda_\perp$, as shown in Figure 8.5 and equation 8.27 matches up with the expression for $I_c(H_a)$ in the wide strip limit, obtained by Kupriyanov and Likharev.

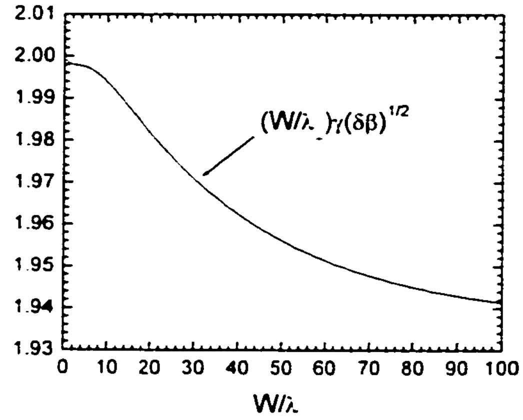

Figure 8.5: Variation of the numerical factor $(W/\lambda_\perp)\gamma\sqrt{\delta\beta}$ with $W/\lambda_\perp$, showing almost no change over the range studied in our measurements. This corresponds to the independence of the critical current with respect to the strip width in the vortex dome regime.

Taking into account this lack of width dependence of $(W/\lambda_\perp)\gamma\sqrt{\beta\delta}$, equation 8.26 shows that in the vortex dome regime, the critical current is essentially independent of the strip width. Thus a narrower strip will have a larger average critical current density, I_c/Wd, than a wide strip. This is in contrast to the case of bulk pinning, where the critical current density is constant, such that a wider strip will support a larger critical current. The crossover from the linearly decreasing $I_c(H_a)$ of the Meissner state to this H_a^{-1} dependence occurs for:

$$I_c = H_a W\gamma\sqrt{\delta/\beta}\,. \tag{8.28}$$

For transport currents just below this critical current, this condition corresponds to the first point at which vortices can enter the strip and not be swept completely across the strip, i.e. this is the first step in the formation of the vortex dome.

Benkraouda and Clem also solved for the critical current in the vortex dome regime for a thick, wide strip with rounded edges. The authors obtained:

$$I_c(H_a)=\frac{\pi W H_s}{2R^2}\left(\frac{H_s}{2H_a}-1\right), R=\sqrt{\frac{W}{d}}. \tag{8.29}$$

For a defect-free edge, the surface field, H_s is expected to approach the thermodynamic critical field, H_c [3]. If the critical surface entry current, j_s in equation 8.26 is taken to be j_{GL}, then equation 8.26 can be rewritten in terms of the surface field for the wide strip limit as:

$$I_c(H_a)\approx\frac{H_c^2 d}{2H_a}. \tag{8.30}$$

For moderate fields, $H_a << H_c$, equations 8.29 and 8.30 agree within a numerical factor of about $\pi/2$.

8.1.4 Critical current at large fields: influence of bulk pinning

As the magnetic field is increased, the critical current due to the edge barrier will continue to decrease with H_a^{-1} and the critical current remains finite in the model of Vodolazov and in the model of Kupriyanov and Likharev. For the solution of Benkraouda and Clem, equation 8.29 describes a vanishing critical current when $H_a = H_s/2$. This discrepancy may be related to an effect of the rounded strip edges assumed in the Benkraouda and Clem model. If weak bulk pinning is present in the strip, then eventually, for sufficiently large magnetic fields, the critical current due to the edge barrier will be reduced to the point where the residual bulk pinning can influence the vortex transport.

Vortex entry over a surface barrier for a thin strip was considered in a somewhat different context by Burlachkov. Koshelev. and Vinokur [8]. The authors studied the problem of vortex activation over surface energy barriers and found that even at large applied magnetic field. $H_a >> H_c$. the surface barrier can still provide an enhancement of the critical current density. The authors considered the total critical current to be composed of a surface barrier contribution and a bulk pinning critical current:

$$I_c = I_c^s + I_c^b . I_c^b = J_c^b \cdot Wd . \qquad (8.31)$$

As in the standard Bean-Livingston surface barrier. vortex entry over the barrier occurs for some penetration field. H_p. which. for an ideal surface. can approach H_c. From the vortex entry and exit conditions at the strip edges. Burlachkov et al. derived an expression for the surface critical current. I_c^s:

$$I_c^s(H_a) \approx \frac{H_p^{\,2} d}{2H_a} . \qquad (8.32)$$

for $H_a >> H_p$. consistent with the expression of Vodolazov in equation 8.30. Because this surface critical current is independent of the strip width. while the bulk pinning critical current is proportional to the width. a wider strip will show the effects of bulk pinning earlier. i.e. for lower applied magnetic fields. Of course. the bulk pinning strength can also have a field dependence. which can be calculated in the context of the Larkin-Ovchinnikov collective pinning theory. discussed in Section 3.2.4.

8.1.5 Current-voltage curves for a strip with an edge barrier

The above derivations have shown that the presence of an edge barrier can have a substantial influence on the behavior of the critical current of a thin superconducting strip. The dynamical, finite voltage state of a thin strip is also affected by edge barriers. Blok and Lempitskii studied the resistive state of a wide strip in an applied magnetic field [9], following an earlier study of vortex transport in wide strips in zero field by Aslamazov and Lempitskii [10]. Blok and Lempitskii treated equation 8.7, replacing n(y) with an expression for the dynamic vortex distribution, written in terms of the electric field and the flux flow viscosity. By solving the resulting expression in the wide strip limit with the vortex entry conditions characteristic of an edge barrier, Blok and Lempitskii obtained relationships for the current and voltage in the strip for various regimes of applied magnetic field and transport current.

At low magnetic fields, for an initial Meissner state of the strip, an increase of the current beyond the critical current results in a linear increase of the electric field, as more vortices are brought into the right edge of the strip and are swept across the strip more quickly:

$$E = \frac{1}{2} E_0 \left(\frac{I - I_c}{I_c} \right), \quad E_0 = \frac{8 I_c^2(0) \Phi_0}{c^3 \eta W^2}, \tag{8.33}$$

where η is the flux flow viscosity given by equation 3.16. As the current is increased further, the self-field of the transport current at the left edge can become large enough to bring anti-vortices into the strip. These anti-vortices are swept to the right by the Lorentz force, where they annihilate with the left-moving positive vortices somewhere in the middle of the strip. This process leads to a doubling of the rate of electric field increase, thus the current-voltage curve should switch to a state with twice the initial differential resistance:

$$E = E_0 \left(\frac{I - I_c}{I_c} \right). \tag{8.34}$$

For still larger transport currents, the vortex density increases more quickly as new rows of vortices enter the strip before the previous row has annihilated. This leads to a quadratic increase of the electric field with the current:

$$E \approx E_0\left(\frac{I}{I_c}\right)^2, \quad I >> I_c. \tag{8.35}$$

Eventually the transport current is large enough that the current density in the middle of the strip reaches the depairing current density, at which point the strip is driven into the normal state [9].

Blok and Lempitskii describe a different scenario for vortex transport at larger magnetic fields, when a vortex dome is present in the strip. The solution in this case, leads to a linear current-voltage relation for moderate transport currents above I_c:

$$E = \frac{\Phi_0}{c^2 \eta W} H_a \left[I - I_c(H_a)\right]. \tag{8.36}$$

This regime corresponds to the standard flux flow, with the differential resistance scaling linearly with the magnetic field and inversely with the strip width. However, at larger currents, the rapid increase of vortex density with transport current again causes a quadratic increase of the voltage with current. The onset of the quadratic dependence occurs at larger transport current values as the magnetic field is increased. For applied fields close to H_{c2}, the linear flux flow behavior should cover almost the entire current-voltage characteristic before the strip switches out to the normal state resistance [9].

In the above derivations for current-voltage characteristics, Blok and Lempitskii did not consider thermal activation over the edge barriers. Burlachkov et al. studied the activated nature of the surface barrier for a strip [8]. The related flux creep type processes lead to curvature in the current-voltage characteristic, primarily for currents just above the critical current, where vortices first enter the strip over the barrier. For larger transport currents, depending on the temperature, the vortex transport should approach the standard flux flow behavior.

8.2 Summary of previous experimental work

The critical currents and current-voltage characteristics of thin superconducting crystals and thin-film strips have been studied extensively over the years. However, many of the properties discussed in Section 8.1 have not been observed yet due to various influences, such as bulk pinning or defective sample edges.

8.2.1 Low-field Meissner regime of $I_c(H_a)$

There are few measurements in the literature of the critical current in superconducting strips for small magnetic fields. Most published studies of strips involve critical current measurements at larger fields such that flux is present in the strip. Lefloch et al. studied the critical current and current-voltage characteristics for strips of TiN films in a perpendicular magnetic field [11]. The authors observed a plateau in $I_c(H_a)$ for fields less than about 1 Oe (80 A/m), with data measured down to 0.01 Oe. The plateau value of I_c, about 2mA, divided by the strip width, 7.5μm is greater than the value of H_a (80 A/m) at the end of the plateau multiplied by π. This is the condition from equation 8.28 for the crossover from a linear to H_a^{-1} dependence of $I_c(H_a)$ in the wide strip limit. Thus the measurements for $H_a < 1$ Oe fit the condition for the possibility of observing a linear decrease of $I_c(H_a)$. The strip in these measurements is most likely not in the wide strip limit, although the value of λ for these films is not stated, but this would only reduce the multiplicative factor for H_a, thus the condition for a linear $I_c(H_a)$ would still be satisfied. The lack of any linear decrease of $I_c(H_a)$ indicates that the vortex transport is dominated most likely by bulk pinning, such that vortices which enter over the edge barrier are prevented from traversing the strip by bulk pinning in the strip.

8.2.2 Critical current measurements in the vortex dome regime

More extensive measurements of the critical current in superconducting strips have been performed at larger magnetic fields, when flux is present in the strip. Castro et al. studied the critical current in type-I superconducting strips and performed magneto-optical imaging of the flux distribution in the strips [12]. The strips were made from high-purity Pb and were approximately 3mm wide and between 0.2mm and 0.6mm thick. The critical current was measured by recording the current-voltage characteristics for different magnetic fields, then extrapolating the linear resistance back to zero voltage. The critical current was observed to decrease as H_a^{-1} over the entire field range of the measurement, reaching zero at $H_a = H_c$, the thermodynamic critical field. The authors were able to fit the $I_c(H_a)$ curves to the following expression:

$$I_c(H_a) = I^*(T)\left(\frac{H_c}{H_a} - 1\right). \tag{8.37}$$

This dependence is similar to the expression derived by Benkraouda and Clem for wide strips, given by equation 8.29, except the results of Benkraouda and Clem predicted a vanishing I_c at $H_a = H_c/2$. This discrepancy was attributed to the type-I nature of the Pb, where superconductivity is destroyed at H_c, while the calculations of Benkraouda and Clem were performed for a type-II strip. Also, the coefficient, $I^*(T)$ did not scale linearly with strip thickness as in the Benkraouda and Clem model, most likely due to the difference between the square edges of the measured strips and the rounded edges treated by Benkraouda and Clem. The authors examined the influence of the edge shape on $I^*(T)$ by beveling one or both of the edges at a 30° angle on some of the strips. A strip with one beveled edge and one square edge exhibited an asymmetry in $I^*(T)$ with respect to the transport current polarity, as the direction with vortex entry on the square (non-beveled) side had a larger value of $I^*(T)$. Castro at el. did not study the width dependence (or independence) of $I^*(T)$.

Castro et al. also directly studied the flux dome profile in the same Pb strips by magneto-optical imaging. The strips were imaged at various magnetic fields, with and without an applied transport current. For $I = 0$, the authors observed the formation of a symmetric flux dome with flux-free regions on either side for magnetic fields above a certain value (about 0.2 H_c). Application of a transport current caused the dome to shift to one side of the strip, and the critical current was found to correspond to the edge of the dome reaching the edge of the strip [12]. The vortex dome has also been observed in type-II superconductors. Zeldov et al. measured the profile of flux penetration, $B(x)$, across the width of wide, thin crystals of BSCCO using an array of Hall probes [13]. The flux was observed to be concentrated into a dome in the middle of the strip, with little flux in the region between the dome and the sample edge.

8.2.3 Measurements of current-voltage characteristics in strips

The vortex transport properties of thin superconducting strips in the finite voltage regime have been studied by many groups. Horn and Parks studied the flux-flow behavior of thin strips made from weak-pinning granular Al films [14]. The authors observe a linear resistance above I_c over a large portion of the current-voltage characteristic, although the flux-flow resistivity exhibited a strange dependence on the magnetic field strength. At large values of the transport current, the voltage was observed to increase more quickly than linearly and the crossover from the linear behavior to the region with positive curvature occurred for larger transport current as the magnetic field was increased. The authors ruled out heating effects as the cause of the curvature and tentatively ruled out self-field effects as well. However, this behavior appears to qualitatively fit the dependence predicted by Blok and Lempitskii (Section 8.1.5), although these measurements predate this theory by over ten years. Tholfsen and Meissner measured flux flow in wide, thin type-I Sn strips [15]. For temperatures close to T_c, the authors observed current-voltage characteristics with a linear flux-flow region above I_c, followed by a curved region, and eventually a sudden jump to the normal state. This behavior persisted down to the lowest magnetic fields measured. The curved region was attributed to a self-field effect, as heating was ruled out as a possible cause. The authors measured the field dependence of the instability current corresponding to the sudden voltage jump and found that this quantity decreased roughly linearly with magnetic field. These measurements again seem to fit qualitatively with the theory of Blok and Lempitskii, but the finite voltage response of the strips in the low-field Meissner state does not appear to have been studied yet.

White et al. investigated the activated nature of the finite voltage state of thin a-MoGe strips [16]. The authors measured the differential resistance, dV/dI, of strips as a function of transport current and temperature for magnetic fields greater than 1kG. At large values of the transport current, dV/dI approached the flux flow resistance and obeyed the standard scaling with strip width and field strength. At lower currents, plots of dV/dI against the transport current exhibited substantial curvature and unusual structure. For the large magnetic fields of these measurements, the strip had a true supercurrent for the lowest temperatures only, while for higher temperatures, the strips had a finite resistance even at zero transport current. The authors studied this zero-bias resistance (R_0) as a function of strip width and temperature. For magnetic fields below

10kG. R_0 was independent of strip width, leading the authors to attribute this behavior to an edge barrier mechanism. At larger fields, R_0 scaled inversely with the width, suggesting the influence of bulk effects. The temperature dependence of R_0 fit to an activation energy model. The corresponding energy scale is most likely related to the surface barrier activation energies studied by Burlachkov et al. [8].

8.3 Experimental techniques for performing transport measurements on thin-film superconducting strips

In order to study edge barrier effects in the transport properties of thin superconducting strips, the strips must be fabricated from materials which are as weak-pinning as possible. The superconductors must also allow for easy patterning into strips with defect-free edges. For these reasons, we have studied strips patterned primarily from the same weak-pinning a-MoGe films presented in the previous chapter on vortex imaging near surface steps.

8.3.1 Sample fabrication

Strips were fabricated from a-MoGe films which were deposited by sputtering onto Si substrates which were either 16mm x 16mm or 8mm x 16mm. These films were obtained from the same batch used for vortex imaging samples. The patterning process was also identical to the a-MoGe step imaging samples: a photolithographic transfer of the strip pattern onto the film followed by Ar ion milling to remove the film away from the pattern. The milling time was chosen to allow for up to a 50% overetch, to ensure the complete removal of any residual a-MoGe away from the strips. During ion milling, care was taken to prevent the sample from overheating in the energetic ion beam. Initially, milling was performed in short intervals of about 1.5 minutes with a 3 minute cooling period in between. Thermocouple measurements of the sample stage temperature indicated that the sample remained below 100°C for such a procedure. More recently, strip samples were ion milled with the sample stage cooled with liquid nitrogen. This maintained the stage temperature between -5 and +10°C during milling. The sample pattern consisted of four parallel strips, with separate current and voltage leads for each strip, as shown in Figure 8.6.

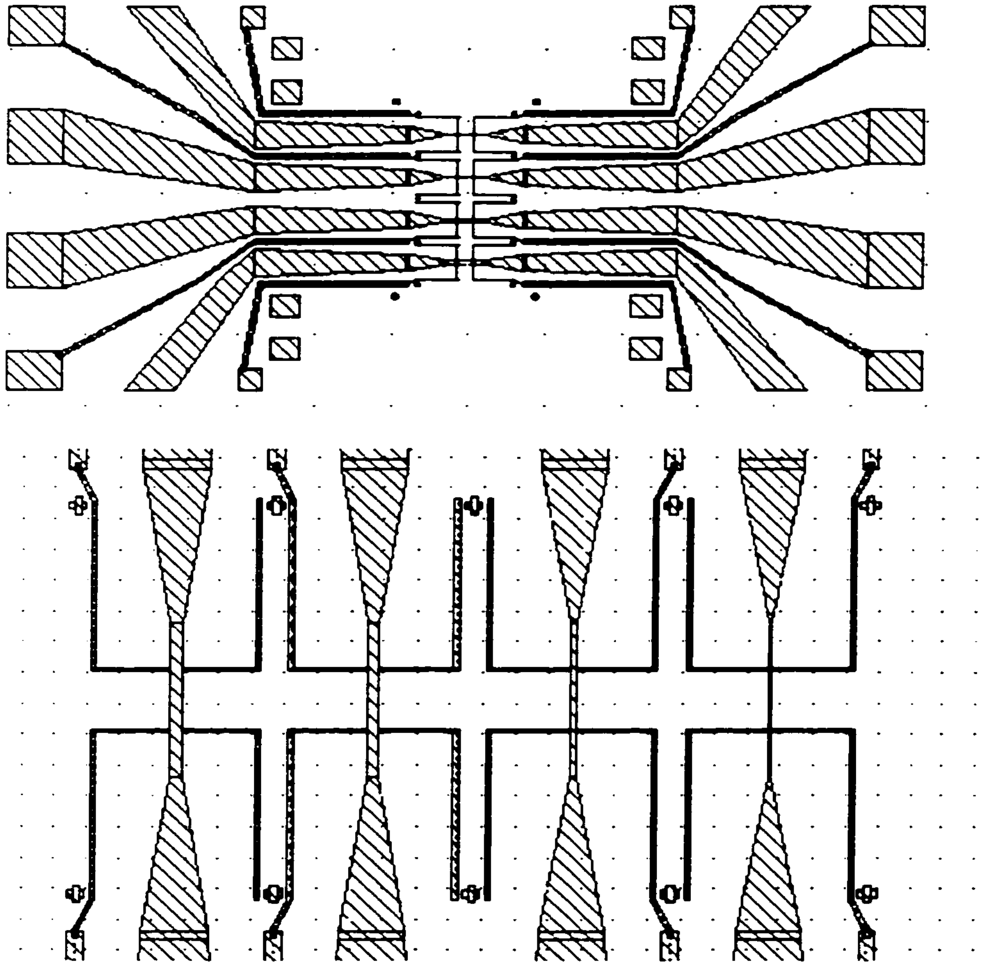

Figure 8.6: Layout of strip pattern used to measure critical currents and current-voltage characteristics in a-MoGe films. Upper diagram shows the layout of the current and voltage leads, with the four strips at the center (dot spacing = 1mm). Bottom diagram is a close-up of the strip region (dot spacing = 100μm).

The voltage leads are spaced by 200μm. Each strip also had two dummy voltage leads on the opposite edge of the strip from the actual voltage leads. These dummy leads were added to rule out any asymmetric behavior due to the possible nucleation of vortices at the intersection point of the voltage leads with the strips. One of the patterns produced four strips with widths of 10, 20, 30, and 40μm, while a different pattern contained four strips, all of which were 25μm wide.

8.3.2 Cryogenic insert

Most of the transport measurements were performed in a non-magnetic cryogenic insert. The insert has a superconducting Helmholtz coil which generates a magnetic field of 106 +/ 0.2 Oe for a current of 1 A, as measured with a Lake Shore Hall probe system. A stage at the cold end of the insert allowed the sample to be placed in the center of the Helmholtz coil, such that the magnetic field was perpendicular to the strips. The insert was cooled in a standard glass helium dewar which was surrounded by a liquid nitrogen dewar. The dewar was surrounded by a double-walled μ-metal shield which reduced the residual field at the sample below 1 mOe. During measurements, the strip sample was immersed in the liquid helium for maximum cooling. Twisted pairs of 40 gauge copper wires were used for the +/-I and +/-V leads for each strip. The wires were attached to the contact pads of the strips with standard indium press contacts.

The critical current measurements at large magnetic fields which will be presented in Section 8.4.3 were performed in a separate dewar. A superconducting solenoid capable of producing magnetic fields up to 8 T in a helium flow-through dewar was used. The sample was again immersed in liquid helium during the measurements.

8.3.3 Measurement technique

The current-voltage characteristics and critical currents were measured by applying a transport current to the strip with a voltage-controlled current supply, capable of providing up to 140mA. The magnitude of the current through the strip was measured with a voltage monitor, consisting of a standard resistor in the output path of the current supply. The sample voltage was measured with a low-noise preamplifier with a voltage gain of up to 10^4. The noise amplitude at the preamplifier output with the strip in the supercurrent state typically corresponded to a sample voltage of less than 0.3μV.

The current-voltage characteristics of the strips were obtained by ramping the transport current up from zero while recording the sample voltage. The process was run from a Labview data acquisition program on a personal computer. The digital-to-analog outputs were configured such that one channel provided a voltage drive for the transport current ramp, while the other channel controlled the current supply for the Helmholtz coil. For each current value on the ramp, 200 voltage readings were averaged, with the readings obtained at between 1kHz and 6kHz by one of the analog-to-digital channels on the computer. The current was first ramped out to the predetermined maximum, then reduced through zero and down to the maximum value for a negative current polarity, and finally the current was ramped back to zero. During this bipolar ramp, the computer recorded each current value from the current supply monitor along with the corresponding average sample voltage.

Most of the strip critical current measurements were performed primarily with a voltage criterion technique. Using a different computer data acquisition program, the transport current was slowly ramped until the sample voltage exceeded a threshold of 1μV. The initial current ramp took roughly one minute to increase from zero to the critical current. In order to reduce the measurement time, subsequent ramps began with a jump to some fraction, typically 50% - 75%, of the previously measured critical current. Repeated measurements of the critical current for zero magnetic field yielded a spread in the measured critical currents of less than 0.5mA for a typical zero-field critical current on the order of 50mA. During a measurement of the field dependence of the critical current, $I_c(H_a)$, for each value of magnetic field, this ramp process was repeated three times and the resulting critical current values were averaged. The computer program recorded the averaged critical current and the corresponding magnet current supply drive voltage. Using the measured Helmholtz coil calibration, this drive voltage was later converted to a field strength, for use in plots of $I_c(H_a)$.

The critical currents at large magnetic fields were measured by an extrapolation of the linear flux flow slopes to obtain the dynamic critical current. At large fields, the strips had little or no true supercurrent portion of the current voltage characteristic, thus determining the critical current with a voltage criterion would have been difficult. For each value of magnetic field, the same data acquisition software was used to record the current-voltage characteristic for each strip. Afterwards, the flux flow slopes were fit to the data and extrapolated back to zero voltage in a graphing program.

8.4 Critical currents in weak-pinning a-MoGe strips

Because of the low bulk-pinning, a-MoGe films are excellent systems for studying the edge barrier effects associated with the strip geometry. We have measured current-voltage characteristics and critical currents for strips patterned from 200nm and 100nm thick films in the layout described in Section 8.3.1. Figure 8.7 contains a plot of the critical current of a 25µm wide, 200nm thick strip, measured with a voltage criterion of 1μV, as described earlier. The variation of I_c with the applied magnetic field exhibits a linear decrease at low magnetic fields, characteristic of vortex entry into the Meissner state, as the current density at the edge of the strip exceeds the critical surface entry current density. At larger magnetic fields, the critical current decreases more slowly, and a line drawn through the origin and this point of initial deviation from the linear dependence has approximately the same magnitude of slope as dI_c/dH_a in the Meissner regime. The intersection point of these two lines should correspond to the first formation of a vortex dome in the strip. The $I_c(H_a)$ curves for these a-MoGe strips exhibit no hysteresis upon sweeping the magnetic field from large values down to zero. This indicates the lack of bulk pinning effects on the vortex dynamics in these strips. The magnetic field strength is plotted in SI units of A/m, such that the linear fits conveniently have a slope in meters.

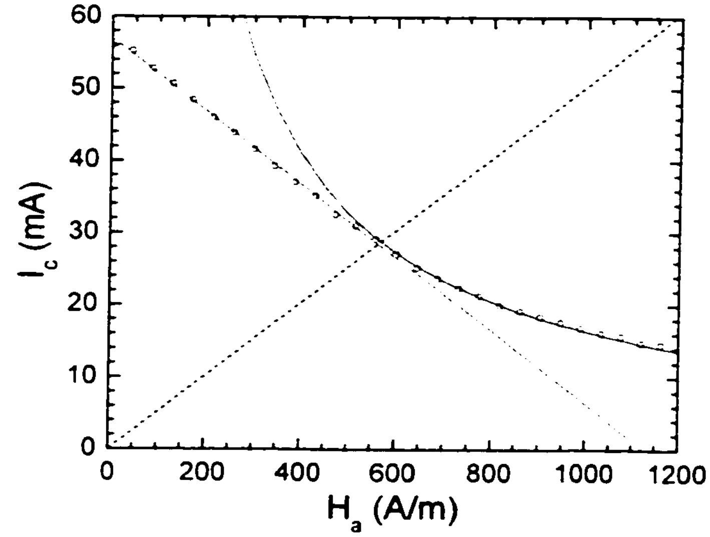

Figure 8.7: $I_c(H_a)$ for a 25μm wide, 200nm thick a-MoGe strip, showing the low-field linear Meissner fit and H_a^{-1} dependence at larger magnetic fields. The dashed line through the origin has the same magnitude of slope as the fit to dI_c/dH_a at low magnetic fields.

$I_c(H_a)$ measurements have been performed on strips with widths between 10μm and 40μm. The wider strips have a larger zero-field critical current, $I_c(0)$, and a steeper slope, dI_c/dH_a in the Meissner regime. At larger magnetic fields, the $I_c(H_a)$ curves for the different width strips join up, and the critical current becomes essentially independent of the strip width, as expected for the edge barrier effect with a vortex dome present. At much larger fields, on the order of 10^6 A/m ($\mu_0 H_a \sim 1$ T), residual bulk pinning in the strips influences the dynamics and the critical current curves separate, such that wider strips have a large critical current.

8.4.1 Low-field Meissner regime and fits to theory

Figure 8.8 contains plots of $I_c(H_a)$ at 4.2 K for a sample with 10μm, 20 μm, 30 μm, and 40 μm wide strips patterned from a 100nm thick a-MoGe film. This particular film had an anomalously low normal-state resistivity (85μΩ-cm) and T_c (6.2 K), corresponding to a shorter zero-temperature penetration depth of 390nm, as calculated in the dirty limit. The critical current was measured for both polarities of applied field and except for the 10μm wide strip, the bipolar plots of $I_c(H_a)$ show a symmetric field dependence within the error of the linear fits. The linear fits were calculated numerically in a graphing program and the range of the fit was determined by varying the endpoints such that the fit intercepted as many data points as possible. The error in the slope was computed by using error bars (not shown) as weights in the linear fit. The error in I_c was estimated for each strip by repeatedly measuring I_c up to 50 times in zero-field, then recording the variation in the obtained values. This error ranged between 0.1mA and 0.5mA for different strips with $I_c(0)$ on the order of 50mA. The error in the applied magnetic field was estimated from the error in the Helmholtz coil field calibration and the uncertainty in the magnetic field current supply, about 0.5mA.

The low-field linear behavior for the 100nm thick strips in Figure 8.8 persists down to the lowest magnetic fields for which the critical current was measured. This set of strips was patterned with the sample stage cooled with cold nitrogen gas during the ion milling. The cooling may have reduced the formation of defects at the strip edges due to the milling process.

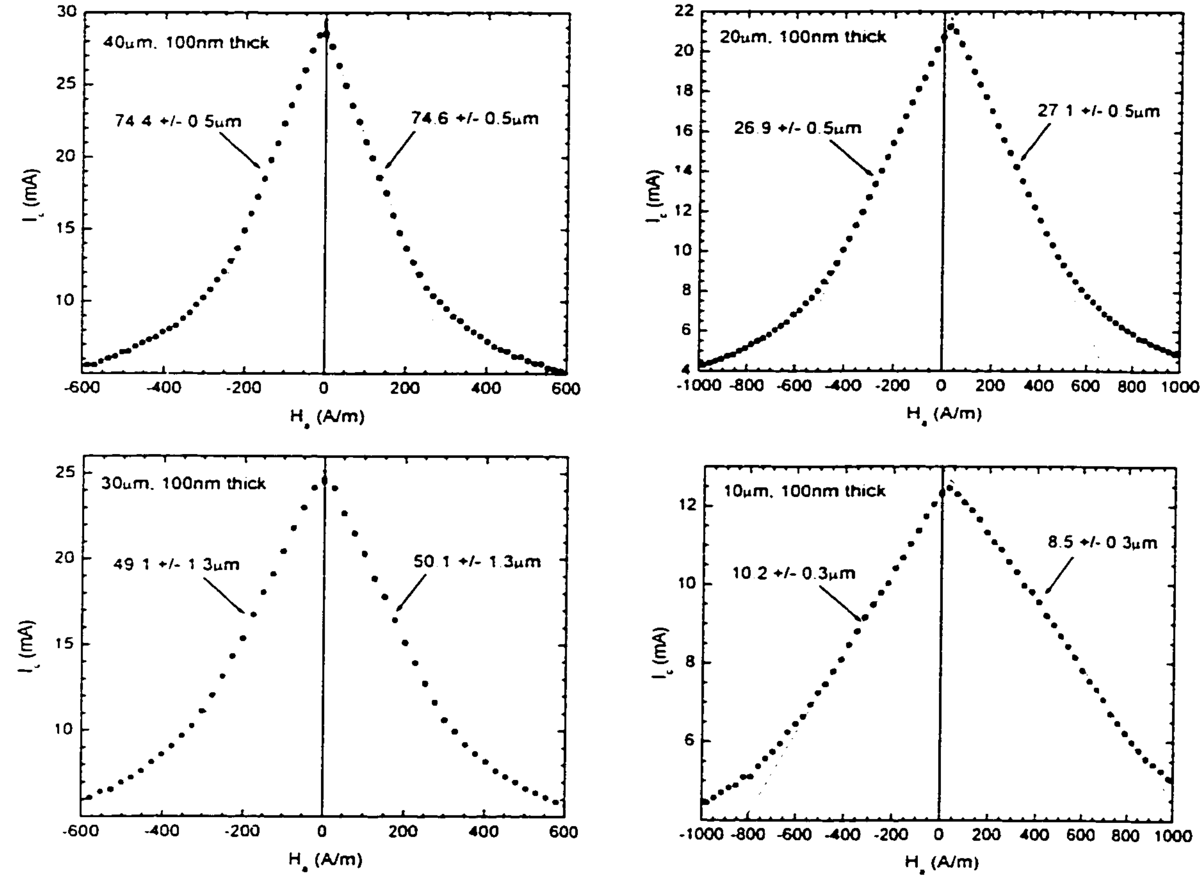

Figure 8.8: $I_c(H_a)$ for the 10, 20, 30, and 40μm wide, 100nm thick a-MoGe strips with fits to the linear behavior at low magnetic fields.

Figure 8.9 contains bipolar $I_c(H_a)$ for a set of the same four strip widths patterned from a 200nm thick a-MoGe film with no stage cooling during the milling. These strips show qualitatively the same dependence as the 100nm thick strips, however, the critical current at the lowest magnetic fields is generally reduced below the extrapolated value from the linear fits of dI_c/dH_a. This breakdown of the linear $I_c(H_a)$ dependence at low fields in the 200nm thick strips may be related to a thermomagnetic instability along the strip edge which is only significant for large values of transport current.

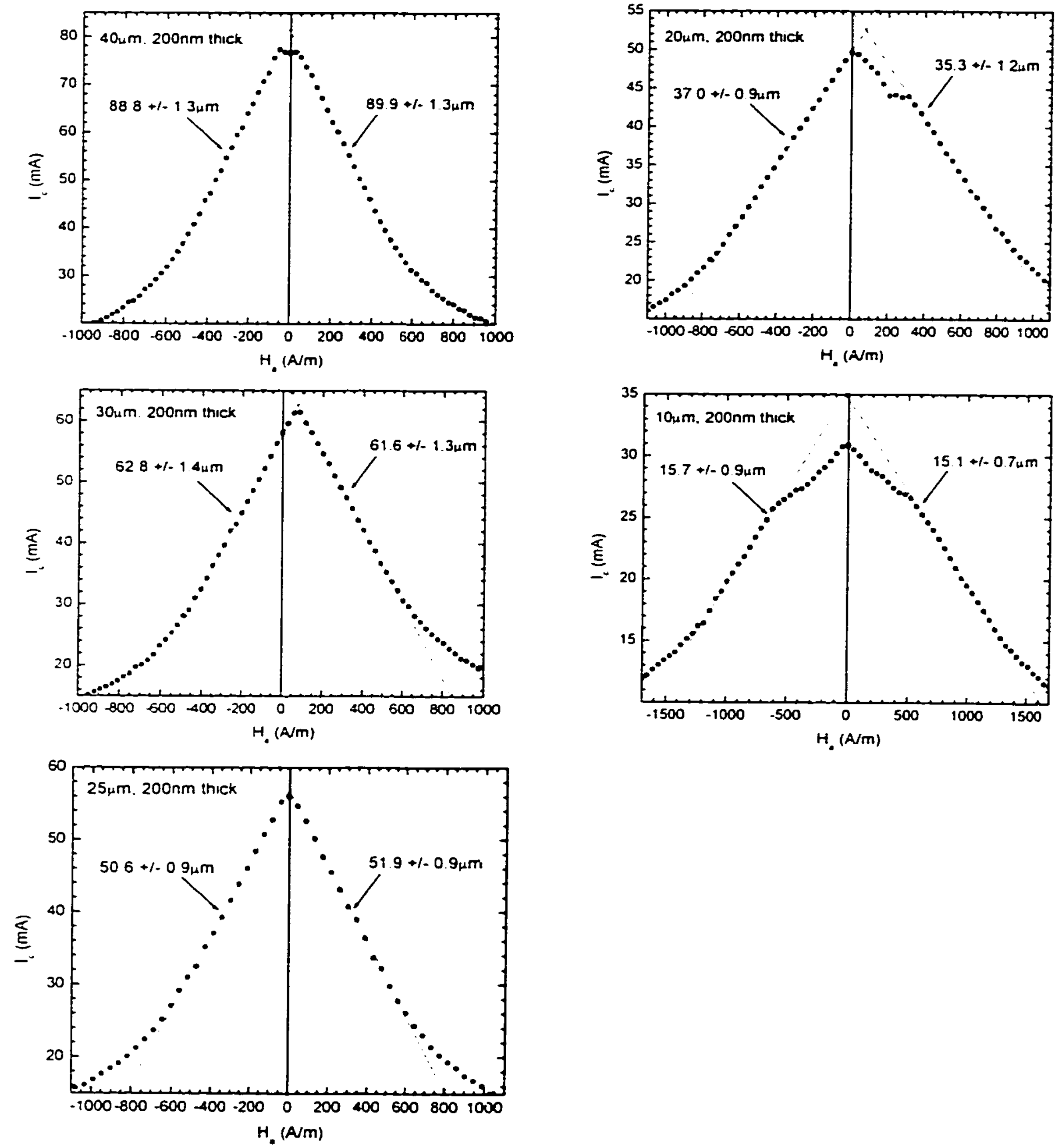

Figure 8.9: $I_c(H_a)$ for the 10, 20, 30, and 40μm wide, 200nm thick a-MoGe strips with fits to the linear behavior at low magnetic fields.

As the magnetic field is increased, the critical current decreases and eventually the transport current required to exceed I_c would be small enough that the power dissipated would not trigger the flux instability. The presence of excess edge defects in the 200nm thick strips could accentuate this instability problem.

Some of the $I_c(H_a)$ plots show the unusual property of a small initial increase of the critical current for one polarity of the applied magnetic field. Thus linear fits of $I_c(H_a)$ for the two polarities of H_a intersect at a maximum value of the critical current which is offset from $H_a=0$. This effect is most pronounced in the 30μm wide and 200nm thick strip shown in Figure 8.9. The offset maximum in $I_c(H_a)$ does not appear to be related to the self-field from the current leads, as the polarity of about half of the offset maxima we have observed is opposite from that which a current lead self-field would cause. Also, we obtain the same offset upon reversing both the magnetic field and transport current polarity, as expected from time-reversal symmetry.

This offset in $I_c(H_a)$ could be caused by an asymmetric amount of roughness between the two edges of the strip. For the magnetic field polarity corresponding to the entry of vortices parallel to H_a at low fields, the self-field from the transport current in the strip may be large enough to allow for the entry of anti-vortices along the rough edge before the entry condition for positive vortices at the smoother edge is satisfied. As H_a is increased, a larger transport current would be required to introduce anti-vortices along the rough edge, resulting in an *increasing* critical current. Eventually, H_a becomes large enough that the entry of positive vortices along the smoother edge becomes favored. For larger values of the applied magnetic field, the critical current should decrease linearly, as the vortex entry is determined by the current density along the clean edge. This process is described schematically in Figure 8.10.

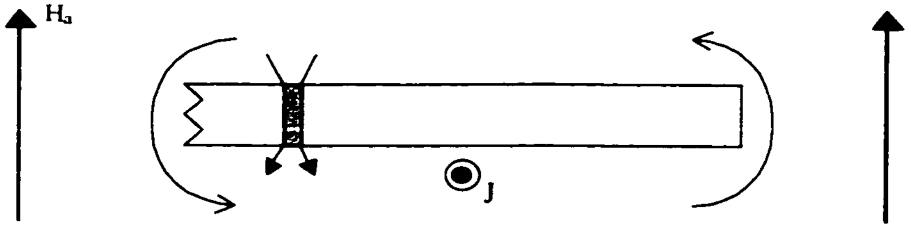

Figure 8.10: Schematic showing entry of anti-vortices along a rough edge of a strip (wavy line along left edge denotes roughness). This mechanism may explain the offset maximum of I_c observed in some of the strips.

We have also measured $I_c(H_a)$ for some of the a-MoGe strips at temperatures below 4.2 K. With the sample immersed in liquid helium, the temperature can be reduced by lowering the pressure above the helium bath with a vacuum pump. The maximum pumping speed available from our pumps results in a bath temperature of about 1.3 K, as determined by a precision pressure gauge and the standard calibration between helium vapor pressure and temperature. Temperatures between 1.3 K and 4.2 K can be achieved by adjusting the pumping rate with an in-line diaphragm flow regulator.

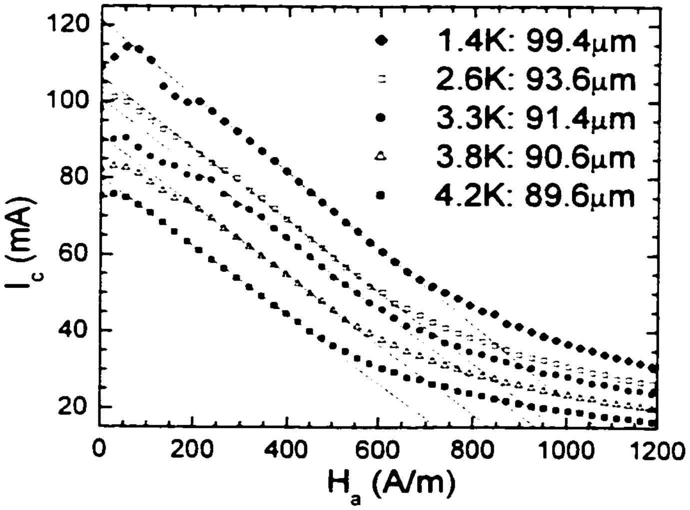

Figure 8.11: $I_c(H_a)$ for the 40μm, 200nm thick a-MoGe strip between 1.4 K and 4.2 K.

Figure 8.11 shows the $I_c(H_a)$ dependence for temperatures between 1.4 K and 4.2 K for the same 40μm wide and 200nm thick strip which was presented earlier. As the temperature is reduced, $I_c(0)$ increases and the slope of the linear fit at low fields, dI_c/dH_a increases as well. At lower temperatures, extra structure develops in the $I_c(H_a)$ curves, particularly near zero-field. This behavior is similar to the measurements on the sample of 200nm thick strips at 4.2 K shown in Figure 8.9. The development of these reduced critical currents (with respect to the linear Meissner extrapolation) at low fields may be related to a thermomagnetic instability.

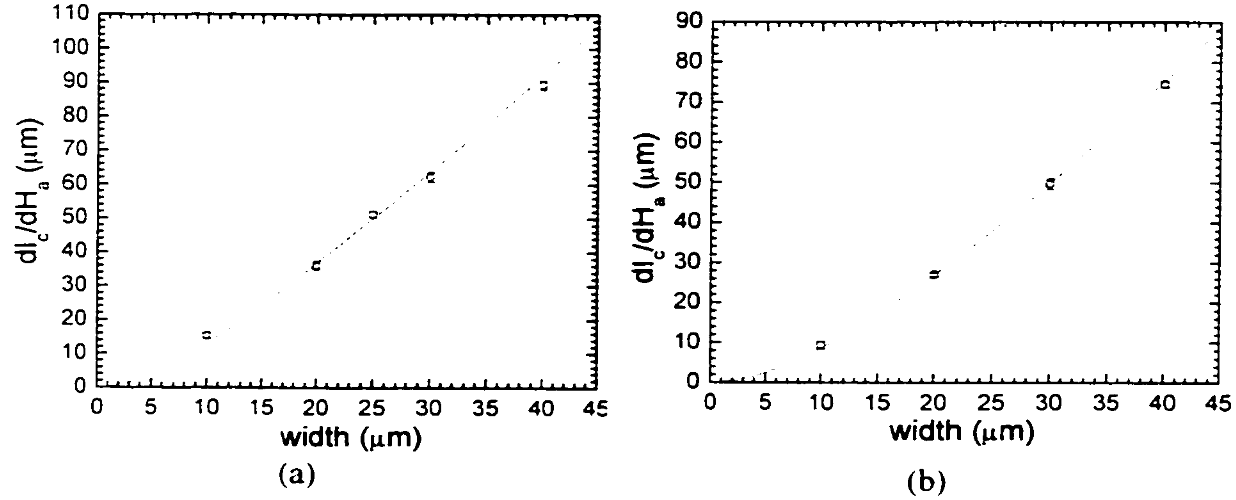

Figure 8.12: (a) Slopes of the linear Meissner fits, dI_c/dH_a as a function of strip width for the 200nm thick a-MoGe strips. The solid line is a fit to the theory of Vodolazov and Maksimov using λ = 670nm. (b) Slopes of the linear Meissner fits, dI_c/dH_a as a function of strip width for the 100nm thick strips. The solid line is a fit to the theory of Vodolazov and Maksimov using λ = 650nm.

Upon measuring $I_c(H_a)$ for each of the strips in the low-field regime, the linear decrease of the critical current was fit as described earlier. A plot of the slopes of these fits against the strip width is shown in Figures 8.12(a) and 8.12(b). As discussed in Section 7.1.1, the zero-temperature penetration depth for most of the films ($\rho_n \sim 180\mu\Omega$-cm, $T_c \sim 6.5$ K) is in the range 510 - 560nm, as calculated from the dirty-limit expression, equation 2.12. At 4.2 K, the penetration depth should increase to 600 - 700nm. For the

200nm thick strips, the thin-film penetration depth, $\lambda_\perp$ = 1.8 - 2.5μm, and is not negligible with respect to the strip width. This quantity is even larger for the 100nm thick films. Thus one would not expect the solutions of Kupriyanov and Likharev or Benkraouda and Clem for the wide-strip limit to quantitatively fit the $I_c(H_a)$ dependence for the strips measured in this work. Figure 8.12(a) shows a fit to the width variation of the linear Meissner slopes for the 200nm thick strips. The fit was generated using equation 8.16 from the solution of Vodolazov for the critical current while varying the penetration depth. The best fit was obtained for λ(4.2 K) = 670nm. Because λ appears in the parameters of equation 8.16 in the form λ^2/d, an uncertainty in the film thickness introduces error into the value of λ from the fit. The fractional error in λ will be one-half of the fractional error in d. Thus a 10% uncertainty in film thickness corresponds to error bars of +/-35nm on λ obtained from the fits of Figure 8.12. Taking λ(0) = 560nm from the dirty-limit calculation, the ratio of penetration depths from the above fit at 4.2 K and λ(0) is:

$$\frac{\lambda(4.2K)}{\lambda(0K)} = 1.20 . \tag{8.38}$$

For T_c = 6.5 K, measurements performed at 4.2 K correspond to a reduced temperature, $t = T/T_c = 0.65$. The two-fluid approximation for the penetration depth corresponds to a temperature dependence of:

$$\frac{\lambda(t)}{\lambda(0)} = \left(1 - t^4\right)^{-1/2}, \tag{8.39}$$

which gives a ratio of 1.10 for t = 0.65. However, the two-fluid approximation does not necessarily hold in the dirty-limit, and no simple universal curve can be predicted from theory [17]. To check the temperature dependence of λ, an independent measurement was performed on an unpatterned a-MoGe film from the same batch of films from which the strip samples were patterned. The penetration depth was measured with a two-coil screening technique in a helium flow-through cryostat, allowing for temperature regulation from 1.7 K to well above T_c. An oscillatory drive current is applied to a small coil in contact with one side of the film, while the amount of signal coupled to a second identical coil on the opposite side of the film is measured with a standard lock-in amplifier. As the penetration depth varies, the amount of the drive signal which is screened by the superconducting film changes as well. Thus by measuring the change in mutual inductance between the two coils and using the film thickness, it is possible to extract the penetration depth of the film. For a 200nm thick film with a T_c of 6.5 K, this two-coil measurement yielded the following ratio [18]:

$$\frac{\lambda(4.2K)}{\lambda(1.7K)} = \frac{735nm}{625nm} = 1.18. \qquad (8.40)$$

A slight further decrease of λ from 1.7 K to 0 K would bring this ratio into agreement with the value of 1.20 from expression 8.38. The value of λ extracted from this two-coil measurement is also influenced by the uncertainty in the film thickness. A fractional error in d of 10% results in an approximate 5% error in λ. Thus a 10% thickness error would bring the two-coil measurement of λ(4.2 K) = 735nm into agreement with the value of 670nm obtained from the fits to the theory of Vodolazov for the Meissner state.

Figure 8.12(b) shows the width dependence of the linear Meissner slopes for the 100nm strips, for which the $I_c(H_a)$ dependence is shown in Figure 8.8. For these data, the best fit to equation 8.16 is obtained for λ(4.2 K) = 650nm. As stated previously, this particular 100nm thick sample exhibited a reduced T_c of 6.2 K and a reduced ρ_n of about 85μΩ-cm, corresponding to λ(0) = 390nm. It is not clear why the ratio:

$$\frac{\lambda(4.2K)}{\lambda(0)} = 1.67 . \qquad (8.41)$$

would be so much larger for this film. The two-coil measurement of λ has not yet been performed on a film showing this reduced T_c and resistivity.

The measured value of the zero-field critical current, $I_c(0)$, can also be compared with the theory of Vodolazov. For an ideal strip, the critical current in zero-field is achieved when the current density at the edges reaches the critical surface entry current density, $j(+/-1) = j_s$. It is possible to relate $I_c(0)$ to j_s using equation 8.17. Thus the relationship between $I_c(0)$ and j_s depends only on the sample variables W, d, and λ. As discussed earlier, many of the low-field $I_c(H_a)$ measurements performed on the a-MoGe strips show a reduction of I_c below the linear Meissner slope for H_a near zero. This effect is most pronounced in the 200nm thick strips and may be related to a thermomagnetic instability which sets in for large values of the transport current.

W(μm)	d(nm)	λ(nm)	$I_c(0)$ (mA)	$\gamma\sqrt{\delta}$	J_s(10^6 A/cm^2)
40	200	670	81.6	0.507	2.0
30	200	670	62.4	0.563	1.9
25	200	670	56.9	0.598	1.9
20	200	670	52.5	0.641	2.1
10	200	670	35.0	0.764	2.3
40	100	650	29.3	0.630	1.2
30	100	650	25.4	0.684	1.2
20	100	650	21.6	0.754	1.4
10	100	650	12.7	0.851	1.5

Figure 8.13: Table of measured values of $I_c(0)$ for the various a-MoGe parameters along with the corresponding parameters from equations 8.10 - 8.13. Surface entry current density calculated using equation 8.17 and $J_s = j_s/d$.

It seems reasonable to define $I_c(0)$ as the current corresponding to the extrapolation of the fit to the linear Meissner slope back to $H_a = 0$. In the case of a small offset maximum in

$I_c(H_a)$. $I_c(0)$ is best defined by the intersection point of the linear fits for the two polarities of $I_c(H_a)$. The values of $I_c(0)$ obtained in this manner are tabulated for the 200nm and 100nm thick strips in Figure 8.13.

From the measured values of $I_c(0)$, the corresponding values of j_s can be calculated using the tabulated values of the quantity $W\gamma\sqrt{\delta}$ from the expressions for δ and γ in equations 8.12 and 8.13. The values of j_s fall in the range 1.8 - 2.3 x 10^6 A/cm^2 for the 200nm thick strips and 1.2 - 1.5 x 10^6 A/cm^2 for the 100nm thick strips. For a defect-free edge, the critical surface entry current density, j_s is expected to approach the Ginzburg-Landau depairing current, j_{GL}, given by equation 2.7. In order to compute j_{GL}, the coherence length, ξ of the film must be known. The zero-temperature coherence length, $\xi(0)$ can be calculated from the dirty-limit expressions using the measured values of $S = dB_{c2}/dT$ [19]. For the 200nm film with $T_c = 6.5$ K, $S \approx 2.8$ T/K, leading to $\xi(0) \approx 4.2$nm, while for the 100nm film with $T_c = 6.2$ K, $S \approx 3$ T/K giving $\xi(0) \approx 4.2$nm as well. The temperature dependence of the coherence length is given by the Ginzburg-Landau expression:

$$\xi(t) = \xi(0)(1-t)^{-1/2}. \tag{8.42}$$

Thus at 4.2 K, ξ for the 200nm film increases to 7.1nm, while for the 100nm film the value of ξ is 7.4nm. Using the values of λ from the fits of the linear Meissner slopes to equation 8.16, the value of j_{GL} is 3.2 x 10^6 A/cm^2 for both the 200nm and 100nm thick films. The error in this value of j_{GL} depends on the uncertainty in the value of λ from the fitting and the error in ξ obtained from the dirty-limit expression. Thus the values of j_s from the measured $I_c(H_a)$ curves at low magnetic fields range from 40 to 70% of the calculated j_{GL}. This reduction of j_s may be related to roughness along the strip edges which would allow the entry of vortices into the Meissner state when the current density at the strip edge is less than j_{GL}. Although this reduction of j_s lowers $I_c(0)$, it should not affect the magnitude of the linear Meissner slope, which only depends on the strip variables W, d, and λ.

8.4.2 Intermediate-field vortex dome regime

As the applied magnetic field is increased from zero, the measured values of I_c decrease linearly until this line intersects a line with the same magnitude of slope drawn through the origin. At this point, the critical current begins to decrease more slowly than the linear dependence characteristic of the Meissner state, as shown in the $I_c(H_a)$ plot for a 25μm wide, 200nm thick strip in Figure 8.7. This deviation from the Meissner slope indicates the formation of a vortex dome, resulting in a H_a^{-1} decay of the critical current as described by the various theoretical treatments. The H_a^{-1} dependence is best analyzed on a double-logarithmic plot, as shown in Figure 8.14 for the 40μm, 20μm and 10μm wide, 200nm thick strips. At low magnetic fields, the linear Meissner regime appears as a downward curve which straightens as the vortex dome begins to develop. A straight line with a slope of -1 drawn through this region is tangent to the linear Meissner fit and provides the pre-factor for the H_a^{-1} behavior. However, as the magnetic field is increased beyond about 2000 A/m (25 Oe), the critical current does not follow this initial H_a^{-1} dependence, but rather decreases with a shallower power-law before again decaying as H_a^{-1}, but with a larger pre-factor. This second H_a^{-1} region develops for applied fields of about 6000 A/m (75 Oe). The values of the H_a^{-1} fit parameters are given in the table in Figure 8.15. As expected for the vortex dome regime, the critical current is roughly independent of strip width, as demonstrated by the closeness of the fit parameters for the different width strips. This demonstrates that bulk pinning does not play a significant role in this field range, as bulk pinning would cause an increase in the critical current for wider strips.

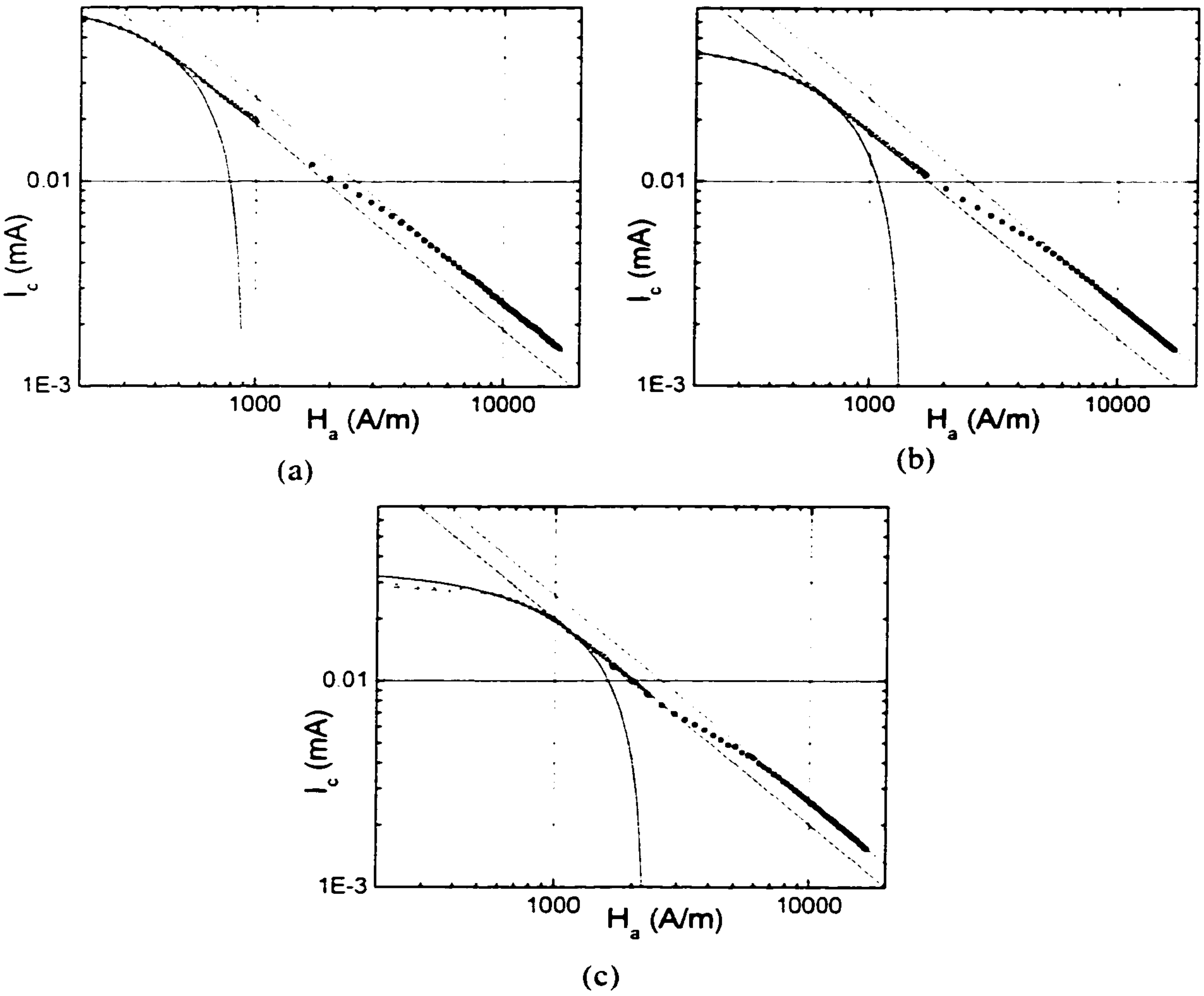

Figure 8.14: Double-logarithmic plots of $I_c(H_a)$ in the intermediate field vortex dome regime for the 200nm thick a-MoGe strips - (a) 40μm wide, (b) 20μm wide, (c) 10μm wide. The coefficients of the straight lines with slopes of -1 are given in the table in Figure 8.15.

Using equation 8.26 from the calculations of Vodolazov for a finite width strip, it is possible to extract the corresponding value of $I_c(0)$ from the pre-factors of each of the H_a^{-1} fits. This computation depends only on the sample variables W, d, and λ through the parameters from equations 8.10 - 8.13, as tabulated in Figure 8.15. For the initial H_a^{-1} fit, the extracted values of $I_c(0)$ correspond closely with the same quantity obtained by extrapolating the linear Meissner slope back to zero-field, as shown in the table of Figure 8.13. The second H_a^{-1} fit at larger fields corresponds to a larger $I_c(0)$. The existence of the two different H_a^{-1} regimes may be related to the presence of defects along the strip edges. It is possible that at low magnetic fields, the linear Meissner slope and the initial formation of the vortex dome are influenced by the entry of vortices along only a portion of the strip length containing edge defects. This segment of the strip would still exhibit the same qualitative behavior, expected for an ideal defect-free strip, i.e. linear Meissner slope determined by W, d, and λ, and H_a^{-1} decay at larger fields, but the value of $I_c(0)$ would be lower, as j_s would be reduced by the edge defects. At sufficiently large magnetic fields, the vortex dome may form along a greater length of the strip, such that the strip appears to have a larger value of j_s. Thus the $I_c(H_a)$ dependence at larger magnetic fields may more closely approach the behavior of an ideal defect-free strip.

W(μm)	d(nm)	λ(nm)	$\gamma\sqrt{\beta\delta}$	a_1(A^2/m)	J_{s1}(10^6A/cm^2)	a_2(A^2/m)	J_{s2}(10^6A/cm^2)
40	200	670	0.111	18.9	2.1	25.4	2.4
20	200	670	0.224	17.2	2.0	25.3	2.4
10	200	670	0.448	20.0	2.1	25.9	2.4
30	100	650	0.281	3.5	1.3	-	-

Figure 8.15: Table of fit parameters from the a-MoGe strips for the various H_a^{-1} regions in the intermediate field regime. The value, a_1 is the coefficient of the H_a^{-1} fit at lower magnetic fields in Figures 8.14 and 8.16, while a_2 is obtained from the H_a^{-1} fit at larger fields. The surface entry current density values are calculated using equation 8.27.

The 100nm thick strips exhibit a similar $I_c(H_a)$ dependence as the 200nm thick strips. A double-logarithmic plot of $I_c(H_a)$ for the 30μm wide, 100nm thick strip is shown in Figure 8.16. At low magnetic fields, the data follow a H_a^{-1} dependence which is tangent to the linear Meissner slope. The pre-factor to the H_a^{-1} fit corresponds to a value of $I_c(0)$ within 5% of the value obtained from the linear fits in the Meissner regime. The critical current values again deviate from this H_a^{-1} fit for magnetic fields on the order of 1000 A/m (~13 Oe). The data continue along a shallower power-law and, unlike the 200nm strips, do not approach a second H_a^{-1} regime with a larger pre-factor, at least within the range of magnetic fields explored in this measurement. It is possible that there is a second H_a^{-1} regime at larger magnetic fields, but it is not yet clear why the 100nm strips would have a much larger transition region between the two H_a^{-1} regimes.

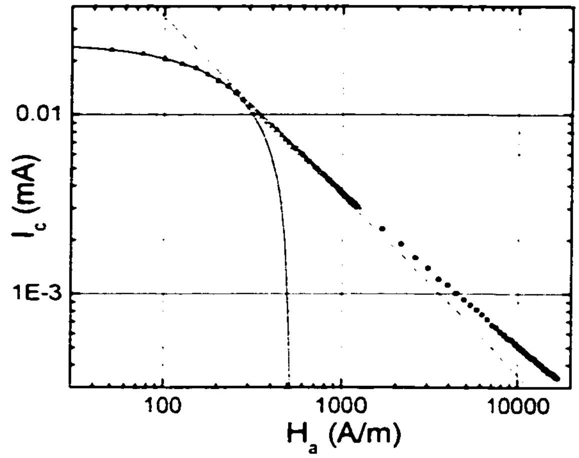

Figure 8.16: Plots of $I_c(H_a)$ in the intermediate field vortex dome regime for the 100nm thick, 30μm wide a-MoGe strip. The coefficient of the H_a^{-1} fit is given in the a_1 column of the table in Figure 8.15.

8.4.3 Large magnetic fields (~H_{c2})

The width-independent H_a^{-1} dependence of the critical current continues out to magnetic fields on the order of 10^5 A/m (~1200 Oe). The 200nm thick strip sample was studied in a different magnet dewar for applied magnetic fields up to 2.4 x 10^6 A/m ($\mu_0 H_a \approx 3$ T). As discussed in Section 8.3.3, the critical current for these measurements was determined from an extrapolation of the linear flux-flow resistance, rather than the voltage criterion technique used in previous $I_c(H_a)$ measurements. This leads to somewhat enhanced critical currents, although the field dependence is qualitatively the same. This issue will be discussed in the next section pertaining to the measured current-voltage characteristics for the strips.

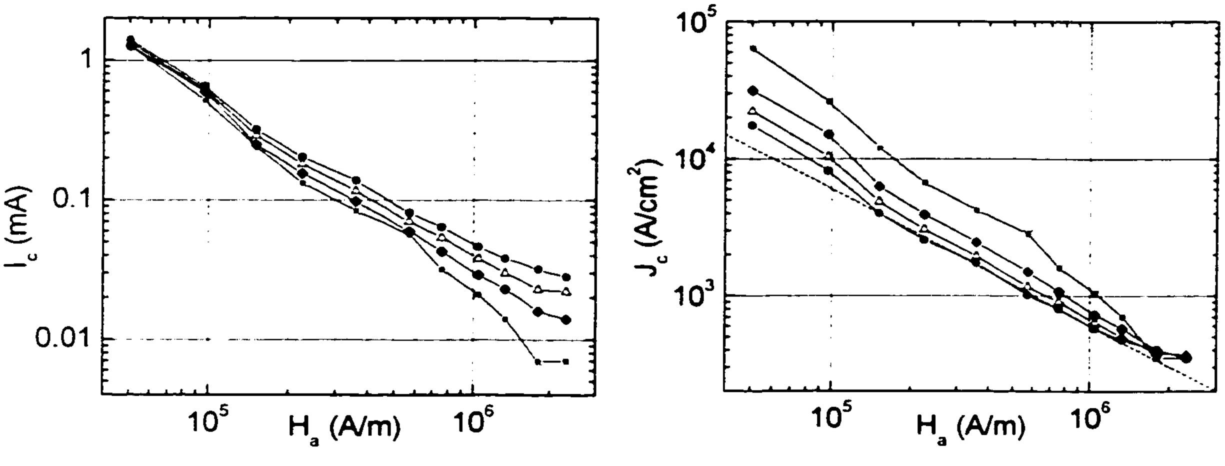

(a) (b)

Figure 8.17: (a) Field dependence of the dynamic critical current for the 200nm thick a-MoGe strips at large magnetic fields obtained from an extrapolation of the linear flux-flow resistance. (b) Average critical current density, obtained for each strip by dividing the critical current by the strip width and thickness. The straight line with a slope of -1 is a guide to the eye and is given by $J_c = \left(6x10^{12}\,A^2/m^3\right)/H_a$, corresponding to $j_c = 3x10^6\,A/cm^2$ for the 40μm wide strip. The symbols used are: asterisk=10μm; diamond=20μm; triangle=30μm; circle=40μm.

Figure 8.17(a) shows the field dependence of the extrapolated dynamic critical current for the four different width, 200nm thick strips on a double-logarithmic plot. The critical current decays as H_a^{-1} and remains essentially independent of the strip width up to magnetic fields around 6 x 10^5 A/m (7540 Oe). At this point, the curves begin to separate, such that the narrower strips have a smaller critical current. This behavior can also be seen by plotting the average critical current density, J_c (=I_c/Wd) as in Figure 8.17(b). This graph shows the enhanced critical current density at lower magnetic fields for narrow strips, as expected for a surface barrier with a vortex dome. Above about 6 x 10^5 A/m, the J_c curves for the different strip widths begin to merge, and for a magnetic field of about 1.6 x 10^6 A/m (~20 kOe), J_c becomes independent of strip width. This seems to indicate that for these large magnetic fields, the bulk pinning in the strips dominates the vortex dynamics. The field dependence of the bulk pinning alone, i.e without the presence of the surface barrier, is not yet known. It may be possible to study the bulk pinning strength as a collective pinning phenomenon with transport measurements on very wide strips patterned from the same a-MoGe films.

8.5 Measurements of current-voltage characteristics in a-MoGe strips

In addition to measuring $I_c(H_a)$ for the a-MoGe strips, we have also studied the current-voltage characteristics (IVC). The strips exhibit different behavior for different magnetic field ranges. For these IVC graphs, we plot the average longitudinal electric field, E, obtained by dividing the measured strip voltage by the voltage lead separation (200μm), against the applied transport current, I.

8.5.1 Low magnetic field - Meissner regime

At low magnetic fields, the IVC for the strips exhibits a true supercurrent followed by a finite voltage state for currents greater than I_c, with substantial structure in the voltage state. Figure 8.18(a) shows the IVC for the 30μm wide, 100nm thick strip in a magnetic field of 130 A/m (1.6 Oe), well within the linear Meissner slope regime as can be seen in the $I_c(H_a)$ plot of Figure 8.8. For comparison with theory as well as other IVC measurements on samples with different lead geometry. the voltages are scaled by the voltage lead separation to give the electric field. E along the strip.

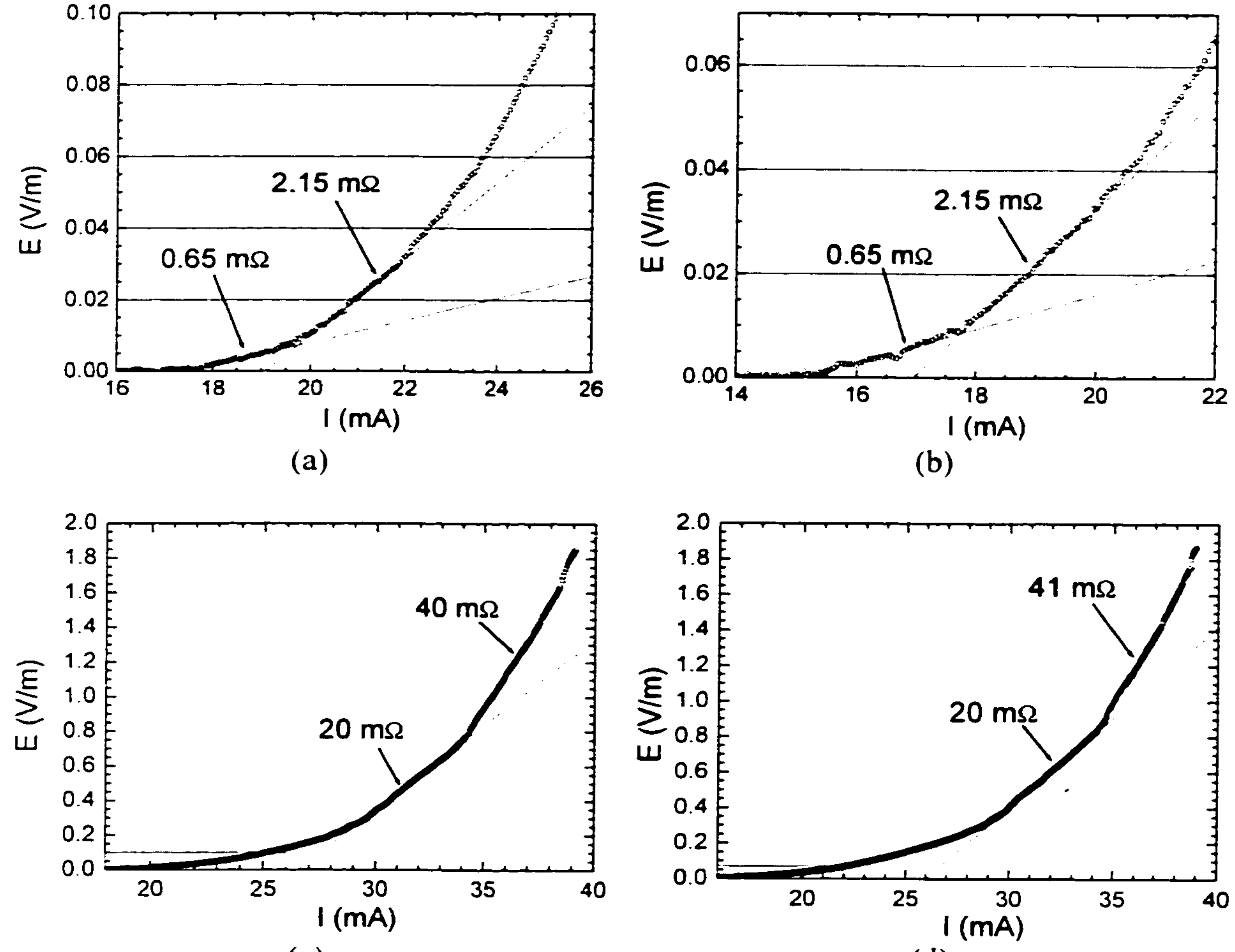

(a) (b) (c) (d)

Figure 8.18: IVC for a 30μm wide. 100nm thick a-MoGe strip in a magnetic field of (a) 130 A/m (1.6 Oe). (b) 170 A/m (2.1 Oe). (c) Same IVC as (a). i.e. 130 A/m. but further out on IVC. (d) same IVC as (b). i.e. 170 A/m. but further out on IVC. In (c) and (d) the range of the IVCs in (a) and (b) is denoted by the box in the lower left.

Upon exceeding I_c. E increases linearly with an initial resistance of 0.65mΩ. crossing the voltage threshold used as the criterion for determining $I_c(H_a)$ in the previous sections. As the transport current is increased. kinks appear in the IVC as the strip switches to regimes of increasing resistance, i.e. a steeper slope in the IVC. Figure

8.18(b) contains an IVC for the same 30μm strip measured at 170 A/m (2.1 Oe), still in the Meissner regime. As expected, this measurement shows a reduced critical current, but the slopes of the initial segments of the IVC are the same as the 130 A/m curve. If a different voltage criterion for determining I_c were chosen on these two IVCs, the value of I_c will change, but the slope dI_c/dH_a remains the same, indicating that the voltage criterion technique is justified for studying the behavior of strips in this magnetic field range.

Beyond the initial linear segments in the IVC for the 30μm wide, 100nm thick strip, the IVC turns upward with a positive curvature. It appears that this behavior may at least qualitatively fit the IVC dependence described theoretically by Blok and Lempitskii from the treatment of wide, thin superconducting strips. However, as the IVC is measured further out, the strip exhibits more structure, with multiple linear regimes. Figure 8.18(c) shows the IVC for the same strip in the 130 A/m (1.6 Oe) magnetic field measured out to the point at which the strip switches to the normal state, with the range of the IVC plot from Figure 8.18(a) indicated by a boxed region. Figure 8.18(d) shows the IVC out to the normal state for a field of 170 A/m, with the range of Figure 8.18(b) indicated by a box. The IVCs taken out to the normal state, Figures 8.18(c) and 8.18(d), contain two substantial linear regimes with slopes of 20mΩ and 40mΩ. It is possible that these two linear sections of the IVC are the regions described by Blok and Lempitskii for the Meissner state, where the lower resistance corresponds to the entry of chains of vortices parallel to H_a along one edge of the strip. The doubled slope is generated by the entry of positive vortices along one edge and anti-vortices at the other edge due to the substantial self-field from the transport current. The smaller resistance structure in the IVC between I_c and the 20mΩ slope region could be caused by the entry of vortices into segments of the strip where the critical surface entry current density, j_s is reduced by edge defects. The 20mΩ slope would then correspond to the first point where a line of vortices along the entire length of the strip edge is brought into the strip over the edge barrier. Qualitatively similar IVCs were obtained for the other width, 100nm thick strips, as well as the 25μm wide, 200nm thick strip.

8.5.2 Large magnetic fields: vortex dome regime

As the magnetic field is increased to the point where a vortex dome forms in the strip and the $I_c(H_a)$ deviates from the linear Meissner decrease, the IVC of the strip changes significantly. Figure 8.19 shows the IVC for the 20μm wide, 100nm thick film measured in magnetic fields of 6340 A/m (79.7 Oe) and 16,820 A/m (211.4 Oe), well into the vortex dome region of the $I_c(H_a)$ curve. For transport currents larger than I_c, the IVC exhibits a linear increase of E with a single slope. As the current is increased further, the IVC deviates from this linear fit with an upward curvature which fits well to a quadratic function. The transition from the linear region to the quadratic behavior occurs for larger electric fields as the magnetic field is increased. Figure 8.20 contains a table of the fit parameters for the linear dependence and the quadratic fits from measurements of the IVC at these two magnetic fields on the four different width, 100nm thick strips.

The resistance value for the initial slope is observed to scale with the width of the strip, although the 10μm wide strip resistivity is consistently 5 - 10% lower than the same quantity measured on the other three strips. This may be due to a small uncertainty in the strip width, which would be most pronounced in the narrowest strip. Upon dividing by the strip width to obtain the resistivity of the linear region, this quantity is seen to scale with the magnetic field as well. This behavior is characteristic of standard flux flow at moderate magnetic fields and indicates a uniform motion of non-overlapping vortex cores across the strip width once the critical current is exceeded.

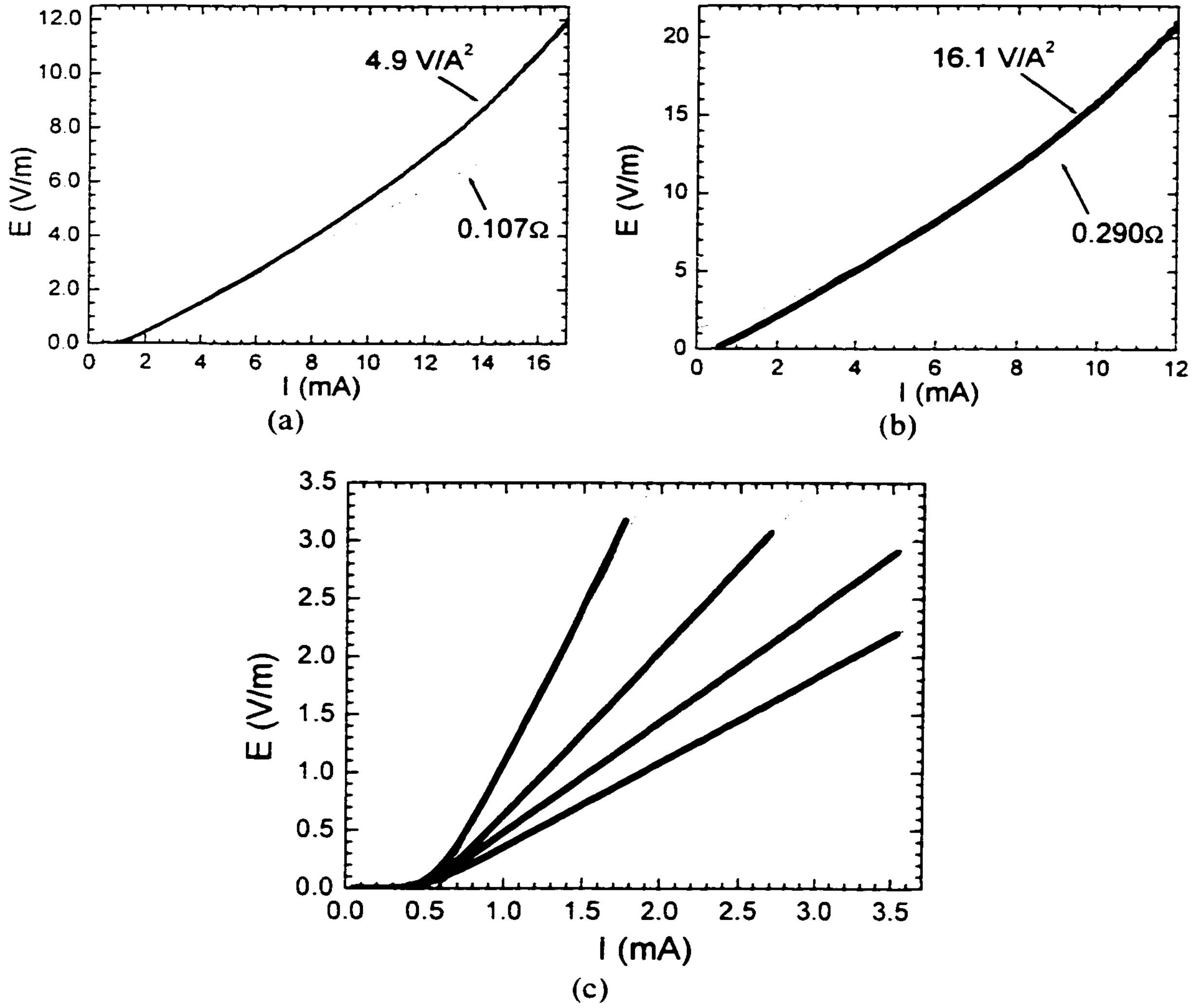

Figure 8.19: IVC for a 20μm wide, 100nm thick a-MoGe strip in a magnetic field of (a) 6340 A/m (79.7 Oe), (b) 16820 A/m (211.4 Oe), with a linear region just above I_c, followed by a curved region which fits well to a quadratic. (c) IVCs for 10, 20, 30, and 40μm wide, 100nm thick a-MoGe strips in a field of 16820 A/m (211.4 Oe), showing the linear resistive behavior in this range of the IVC. Shallowest slope corresponds to the 40μm wide strip, while the steepest slope corresponds to the 10μm wide strip. The quadratic dependence occurs further out on the IVC, as in (a) and (b), although the 10μm wide strip shows a slight curvature in this range.

The coefficient of the quadratic term in the fits to the curved region further out on the IVC are also tabulated in Figure 8.20. These terms approximately scale with the inverse square of the strip width, and the coefficients increase roughly linearly with the applied magnetic field.

W(μm)	d(nm)	c (Ω) (6340 A/m)	d (V/A^2) (6340 A/m)	c (Ω) (16.820 A/m)	d (V/A^2) (16.820 A/m)
40	100	0.054	1.3	0.146	4.1
30	100	0.072	2.5	0.192	6.8
20	100	0.107	4.9	0.290	16.1
10	100	0.199	20.0	0.515	65.4

Figure 8.20: Table of parameters from linear and quadratic fits to the IVC behavior of the 100nm thick a-MoGe strips for intermediate fields. The value of the parameter, c is obtained from the linear fits of the IVC just above I_c, while the parameter, d is the coefficient of the second-order term from a quadratic fit to the curved region further out on the IVC.

Tests were performed to rule out sample Joule heating as a source of the curvature in the IVC. For the same magnetic field, the IVC was recorded with a thirty times faster ramp rate, yielding an identical IVC to the initial measurement. If heating were the source of the curvature, then a faster ramp would dissipate less power and should result in less curvature. The strip voltage was also monitored as a function of time with the transport current adjusted such that the strip was in the curved region of the IVC. The voltage was observed to remain constant, whereas heating effects would be expected to cause an increase in the voltage with time. This quadratic behavior fits qualitatively with the calculations of Blok and Lempitskii for the IVC of superconducting strips with edge barriers described by equation 8.35. In the Blok and Lempitskii model, the quadratic behavior results when the transport current is large enough that both the vortex density and flow velocity scale with the transport current [9, 10]. The scaling of the quadratic fit with strip width and magnetic field strength is similar but not identical to the prediction of Blok and Lempitskii. This is most likely related to the fact that Blok and Lempitskii considered the wide strip limit, while the strips measured in these experiments were all of finite width with respect to the thin-film penetration depth.

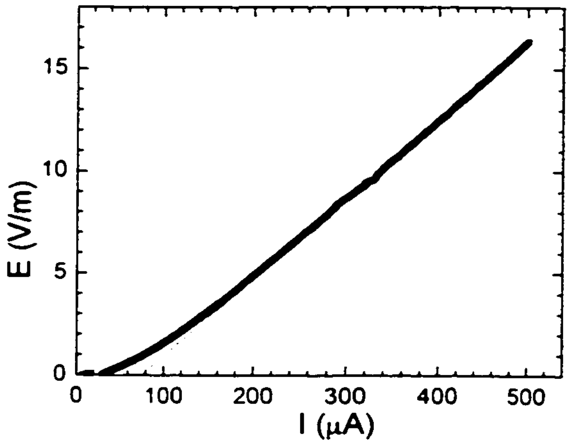

Figure 8.21: IVC for a 10μm wide, 200nm thick a-MoGe strip in a magnetic field of 5.7 x 10^5 A/m (7170 Oe). The linear fit corresponds to a resistance of 7.64Ω, and extends over most of the IVC.

For larger magnetic field strengths, the linear flux-flow behavior extends out further on the IVC, while the extent of the curved region is diminished. Figure 8.21 shows the IVC for the 10μm wide, 200nm thick strip in a magnetic field of 5.7 x 10^5 A/m (7170 Oe). At such large magnetic fields, the IVC is linear over most of the range measured, although there is significant curvature at small values of E, just above I_c. Because of this curvature near I_c, the critical current at these large magnetic fields was determined by an extrapolation of the flux flow resistance instead of the previously used voltage criterion of the previous I_c measurements. This conversion to measurements of the dynamic critical currents led to an enhancement of the recorded values of I_c, and may account for the larger pre-factor in the $I_c(H_a)$ measurements at the largest magnetic fields. shown in Figure 8.17. The resistances corresponding to the linear fits in this magnetic field range scaled inversely with strip width. such that the flux-flow resistivity was independent of the width. Figure 8.22 contains a plot of the flux-flow resistivity. ρ_f as a function of magnetic field. At low magnetic fields. ρ_f increases linearly with field. as expected from the Bardeen-Stephen treatment of flux-flow for isolated vortex cores in the low-temperature limit. as described earlier. However. at larger magnetic fields. collective effects become significant and the ρ_f dependence curves upward away from the linear dependence. This curvature is similar to the initial flux-flow measurements of Kim et al. [20]. The curved ρ_f dependence is discussed by Berghuis and Kes in the context of 2D collective pinning [21].

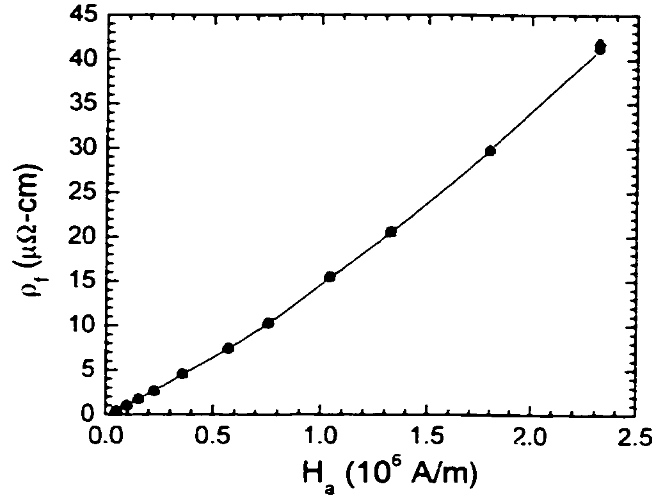

Figure 8.22: Flux-flow resistivity. ρ_f versus magnetic field as measured from the 200nm thick a-MoGe strip IVCs. The data follow a linear dependence at low magnetic fields. but curve upwards at larger fields.

8.6 Critical current measurements on strong-pinning Nb strips

In order to contrast the edge barrier dominated $I_c(H_a)$ dependence in weak-pinning a-MoGe strips, we have also performed critical current measurements on strips made from films with substantial bulk pinning. Sputtered Nb films displayed bulk pinning strengths on the order of 10^6 A/cm^2 at low magnetic fields. Strip patterns similar to those of the a-MoGe samples were etched into 100nm thick Nb films which were dc sputtered onto sapphire substrates. The etching was accomplished with a Reactive Ion Etching system, and the strip widths studied were 15, 20, and 25μm.

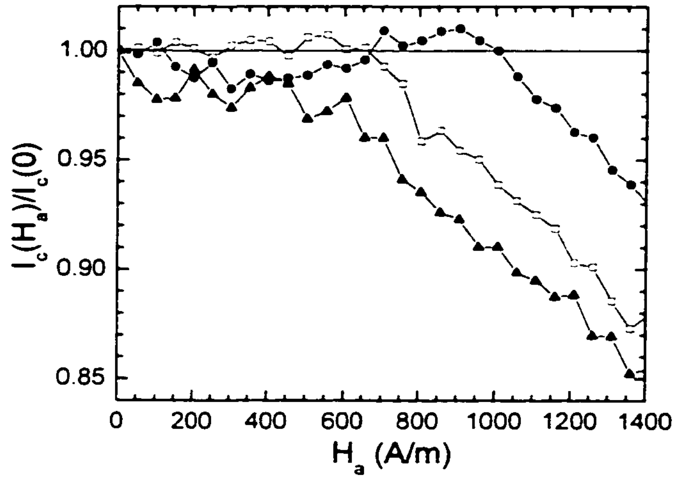

Figure 8.23: $I_c(H_a)/I_c(0)$ for 100nm thick Nb strips with widths of 15, 20, and 25μm. Solid line is a guide to the plateau behavior of I_c for low magnetic fields. Symbols used are solid circle = 25μm; hollow square = 20μm; solid triangle = 15μm.

Figure 8.23 contains a plot of $I_c(H_a)$ for the three Nb strips, where the I_c values have been scaled by the corresponding $I_c(0)$. The critical current dependence is qualitatively different from that of the weak-pinning a-MoGe strips. Instead of the initial linear decrease of I_c with magnetic field, the critical current for the Nb strips exhibits a plateau out to fields on the order of 800 A/m (10 Oe) before the critical current begins to decrease. The plateau region extends to larger magnetic fields as the strip width is increased. At larger magnetic fields, the critical current decreases, and the I_c values scale linearly with the strip width, indicating that I_c is dominated by bulk pinning. This is in sharp contrast to the width-independent edge barrier H_a^{-1} dependence of the critical currents in the weak-pinning a-MoGe strips.

8.7 Effects of surface steps on transport in a-MoGe strips

In Chapters 6 and 7, surface steps on superconducting thin-films and crystals were observed to have a significant influence on the vortex dynamics as well as the field-cooled flux distributions as seen with SSM imaging. We have performed preliminary measurements of the critical current for a-MoGe strips with a single transverse surface step in the middle of the strip. Figure 8.24(a) shows the geometry of the step which was etched into the 25μm wide strips with the same techniques used to produce the thin-film step samples for the SSM imaging experiments.

The critical current was measured with a voltage criterion of 1μV. Figure 8.24(b) contains a plot of the bipolar $I_c(H_a)$ dependence for a 25μm wide, 200nm thick strip with a 80nm step etched into the surface. The critical current for this strip exhibits substantial asymmetry with field, with the linear slopes for the two field polarities differing by over 20%. The $I_c(H_a)$ also has a significant offset maximum. The field polarity with the offset maximum and the shallower slope corresponds to the entry of vortices parallel to H_a along the thick edge of the strip. Qualitatively similar behavior was observed for other strips with different step heights. The asymmetry in the low-field linear slopes was observed to decrease for smaller step height, although there was substantial scatter in the data. Although it seems plausible that a surface step would result in an asymmetric $I_c(H_a)$, the observed behavior is not understood at the present time.

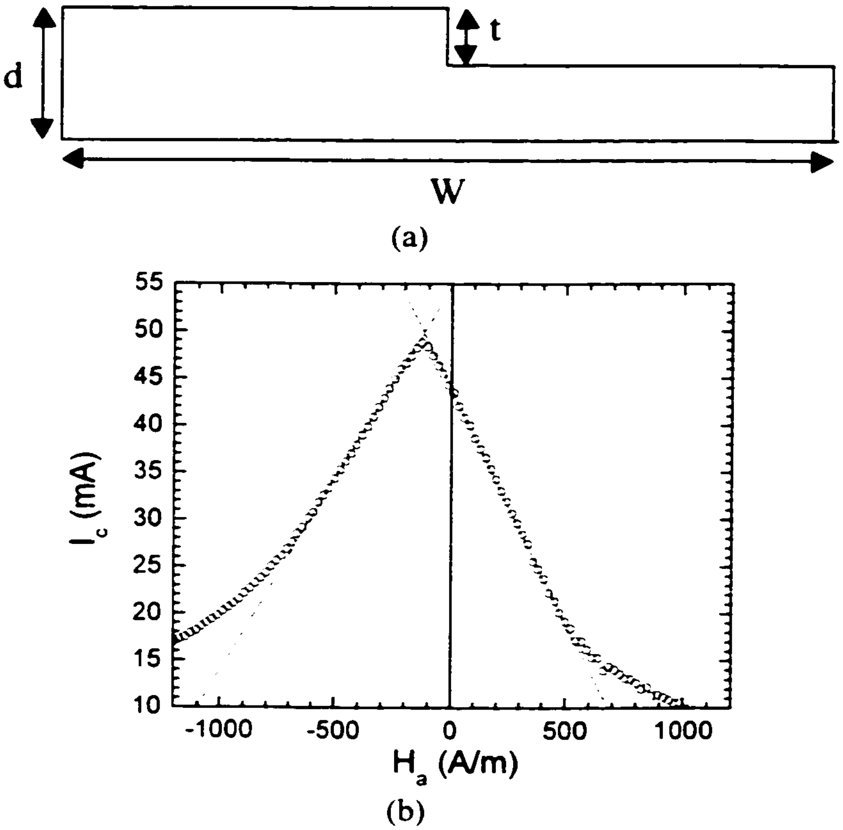

Figure 8.24: (a) Schematic of the surface step geometry for a strip. (b) $I_c(H_a)$ for a 25μm wide, 200nm thick a-MoGe strip with an 80nm surface step. The linear fit for $H_a > 0$ has a slope of 49.8μm, while the fit for $H_a < 0$ has a slope of 40.7μm.

8.8 Conclusions and future work

We have probed the interactions between vortices and sample edges in thin superconducting strips through measurements of the field dependence of the critical current. For strips with weak bulk pinning, the edge barrier mechanism dominates the vortex transport over most of the range of magnetic fields we have studied. We observe three different magnetic field regimes in the critical current behavior. At low magnetic fields, we have measured a linear decrease of I_c as the magnetic field is increased. The slope, dI_c/dH_a along with $I_c(0)$ are larger for wider strips. When the magnetic field is larger than a surface entry threshold field, the critical current values deviate from the linear decrease and follow a $1/H_a$ dependence. The critical current in this intermediate field regime is independent of the strip width, as expected for the dynamics of a vortex dome. At magnetic fields approaching H_{c2}, the critical current curves separate such that wider strips exhibit a larger I_c. In this large field regime, the residual bulk pinning in the strips dominates the edge barrier critical current, which has been substantially reduced by the large magnetic field.

The measurements of the critical current in weak-pinning thin-film superconducting strips presented in this chapter demonstrate that edge barriers play a significant role in the vortex dynamics for this strip geometry. In many instances, the observed behavior fits well to the theoretical calculations. However, the critical currents appear to be sensitive to the presence of defects along the edge of the strip. This is manifest in reduced values of the critical surface entry current density, j_s, and as extra structure in the IVC for the strips, particularly at low magnetic fields. A detailed study of the influence of edge defects on the strip response would be useful. Cleaner edges could be produced by cooling the sample to lower temperatures during the ion mill patterning or possibly by switching to another, less damaging patterning technique altogether. The possibility of vortex nucleation at the intersection points of the superconducting voltage leads with the strip edge could be eliminated by switching to normal metal voltage leads which only contact the strip in the middle of the top surface. The leads could be isolated from the strip edge with a layer of a sputtered insulating film. The addition of multiple voltage leads along the length of the strip would make possible measurements of the uniformity of the critical current. For an ideal strip with defect-free edges, the critical current should not vary along the length of the strip. Artificial edge defects could be introduced along a portion of the edge between only one pair of voltage leads. The effect of the defects on the critical current and IVC uniformity could be observed by measuring different pairs of voltage leads.

Further study of the critical currents in the strips with surface steps could reveal the nature of the vortex dynamics in this asymmetric strip geometry. The different edge barriers for the two sides of the strip with different thickness could provide a means for controllably fabricating strips with asymmetric vortex dynamics. An investigation of this behavior would be greatly assisted by the ability to image the vortex distributions in the strip. Unfortunately. the magnetic field scale required for such imaging is outside the range of capability for the SSM. Perhaps a different magnetic imaging technique. such as magneto-optical imaging. would provide information about the vortex entry at the edges and motion around the surface step.

8.9 References

[1] M. Y. Kupriyanov and K. K. Likharev. *Effect of an edge barrier on the critical current of superconducting films*. Sov. Phys. Solid State **16**. 1835 (1975).

[2] D. Y. Vodolazov and I. L. Maksimov. *Distribution of the magnetic field and current density in superconducting films of finite thickness*. cond-mat/0001035 (2000).

[3] M. Benkraouda and J. R. Clem. *Critical current from surface barriers in type-II superconducting strips*. Phys. Rev. B **58**. 15103 (1998).

[4] E. H. Brandt and M. Indenbom. *Type-II-superconductor strip with current in a perpendicular magnetic field*. Phys. Rev. B **48**. 12893 (1993).

[5] D. Y. Vodolazov. I. L. Maksimov. and E. H. Brandt. *Modulation instability of the order parameter in thin-film superconductors with edge barrier*. Europhys. Lett. **48**. 313 (1999).

[6] D. Y. Vodolazov. *Private Communication* (2000).

[7] A. Y. Aladyshkin. A. S. Mel'nikov. I. A. Shereshevsky. *et al.*. *Influence of surface irregularities on barriers for vortex entry in type-II superconductors*. cond-mat/9911430 (1999).

[8] L. Burlachkov. A. E. Koshelev. and V. M. Vinokur. *Transport properties of high-temperature superconductors: Surface vs bulk effect*. Phys. Rev. B **54**. 6750 (1996).

[9] B. Y. Blok and S. V. Lempitskii. *Effect of a magnetic field on the resistive state of a wide superconducting film*. Sov. Phys. Solid State **26**. 272 (1984).

[10] L. G. Aslamazov and S. V. Lempitskii. *Resistive state in broad superconducting films*. Sov. Phys. JETP **57**. 1291 (1983).

[11] F. Lefloch. C. Hoffman. and O. Demolliens. *Nonlinear flux flow in TiN superconducting thin film*, Physica C **319**. 258 (1999).

[12] H. Castro. B. Dutoit. A. Jacquier. *et al.*. *Experimental study of the geometrical barrier in type-I superconducting strips*. Phys. Rev. B **59**. 596 (1999).

[13] E. Zeldov. A. I. Larkin. V. B. Geshkenbein. *et al.*. *Geometrical Barriers in High-Temperature Superconductors*. Phys. Rev. Lett. **73**. 1428 (1994).

[14] P. M. Horn and R. D. Parks. *Flux-Flow and Fluctuation Effects in Granular Superconducting Films*. Phys. Rev. B **4**. 2178 (1971).

[15] P. Tholfsen and H. Meissner. *Flux Flow in Thin Type-I Superconducting Films*. Phys. Rev. **185**. 653 (1969).

[16] W. R. White. A. Kapitulnik. and M. R. Beasley. *Collective Vortex Motion in a-MoGe Superconducting Thin Films*. Phys. Rev. Lett. **70**. 670 (1993).

[17] M. Tinkham. *Introduction to Superconductivity* (McGraw-Hill. Inc.. New York. 1996).

[18] K. Osborn. *Private Communication* (2000).

[19] R. Besseling, *Private Communication* (2000).

[20] Y. B. Kim. C. F. Hempstead. and A. R. Strnad. *Flux-Flow Resistance in Type-II Superconductors*, Phys. Rev. **139**. A1163 (1965).

[21] P. Berghuis and P. H. Kes, *Two-dimensional collective pinning and vortex-lattice melting in a-*$Nb_{1-x}Ge_x$ *films*, Phys. Rev. B **47**. 262 (1993).

VITA

Britton Louis Plourde was born on November 9. 1970 in Bethesda. Maryland. He graduated from the University of Michigan in Ann Arbor in 1993 with a B.S. in physics and a B.Mus. in flute performance. Britton won the Williams undergraduate physics thesis award along with a merit scholarship from the College of Literature. Science. and the Arts. He was also awarded first place in the undergraduate concerto competition in the music department.

After starting graduate school in Urbana in 1993. Britton won a graduate teaching award in 1994 for his activities as a teaching assistant. He received the M.S. in physics in 1995. In 1994. Britton joined the research group of Dale Van Harlingen and began studying magnetic imaging techniques and vortex dynamics. Since 1994. Britton has given presentations at many scientific conferences. including a NATO Advanced Study Institute in Kusadasi. Turkey in 1998. While in Urbana. he continued his musical studies and obtained a M.Mus in flute performance in 1999. From 1997 to 2000. Britton played the flute in the Illinois Symphony Orchestra in Springfield. IL.

After completing the Ph.D. program at the University of Illinois. Britton will continue studying superconducting devices at the University of California at Berkeley.